A COMPUTER-BASED JUSTIFICATION FOR USING THE SIMPLE BEND TEST AS THE BASIS FOR PREDICTING THE PERFORMANCE OF STEEL HOOKED-END FIBRES IN REINFORCED CONCRETE

by

T. J. Bam

Submitted in partial fulfilment of the requirements for the degree

Master of Engineering (Mechanical Engineer)

in the

Department of Mechanical and Aeronautical Engineering
Faculty of Engineering, Built Environment and Information Technology
UNIVERSITY OF PRETORIA

2019

© University of Pretoria

UNIVERSITEIT VAN PRETORIA
UNIVERSITY OF PRETORIA
YUNIBESITHI YA PRETORIA

ABSTRACT

A COMPUTER-BASED JUSTIFICATION FOR USING THE SIMPLE BEND TEST AS THE BASIS FOR PREDICTING THE PERFORMANCE OF STEEL HOOKED-END FIBRES IN REINFORCED CONCRETE

by

T.J. Bam

Supervisors: Prof. Schalk Kok
Prof. Nico Wilke
Department: Mechanical and Aeronautical Engineering
University: University of Pretoria

The classical test to confirm the performance of a given fibre design for use in reinforced concrete is the pull-out test. While attempts have been made to simulate the performance of such pull-out tests, in practice it has been found that there is a significant disparity between prediction and real-life performance.

The high strength of steel reinforcing fibres is a consequence of the cold wire drawing process and subsequent fabrication. Residual stresses exist in cold drawn wire as a consequence of the elastic response to a non-uniform distribution of plastic strain. This also introduces a yield strength profile where yield strength varies radially through the wire. The question arises as to whether fibre design should use a starting material model that considers these properties.

This thesis examines whether the tensile test, simple bend test and pull-out test provide enough information to define a starting material model that may be used for further design and simulation of such fibres.

Since the details of the wire drawing process and material specification are proprietary and therefore unknown, a sensitivity study was conducted to determine which aspects of the wire drawing process have the greatest effect on the pull-out curve and the following were established as being significant:

- Plastic strain due to wire drawing was shown to be the most important factor.
- The bilinear curve was shown to be a suitable approximation for the stress-strain curve.
- Replacing the plastic strain profile with a single value of average equivalent plastic strain is practical.

The following were established as having negligible effect:

- The consequences of the hooked-end forming process.
- The residual stress profiles due to wire drawing provided that the above was also excluded.
- The hardening law

While inverse analysis demonstrated that all tests provide sufficient information to determine the required properties for this bilinear material model, the pull-out test was shown to provide more accurate approximations of the maximum pull-out force at the first and second peaks and the bend test was shown to produce more accurate approximations of the energy associated with pull-out. Good correlation with the baseline pull-out curve was found for both the isotropic and the kinematic hardening laws and it is concluded that behaviour during pull-out is insensitive to the hardening law.

Sensitivity analysis and characterisation of the material model using an experimental pull-out curve demonstrated the importance of the coefficient of friction. Full characterisation using the pull-out curve therefore requires the solution to a three-variable problem: yield strength, tangent modulus and coefficient of friction. This was a suggested topic for further study.

© University of Pretoria

ACKNOWLEDGEMENTS

I gratefully acknowledge the assistance provided by Dr. Danie De Kock and his team at Qfinsoft in facilitating access to the Ansys suite of software which was so central simulations, analysis and reporting and for their support in guiding me in their use and overcoming technical problems. Without their support this thesis would not have been possible.

Professor Kok and Professor Wilke, University of Pretoria, Department of Mechanical and Aeronautical Engineering, I thank you for all the time and energy you made available in terms of guiding me, reviewing my work and providing me with the necessary advice and correction to bring it to its current level.

I am also grateful to my manager, Mrs. Roelien Vorster, for assisting me in managing my work schedule in pursuit of this task; and all my colleagues in the Metallurgy and Integrity department at Sasol who supported and encouraged me.

My husband, Campbell, who not only encouraged and supported me but was also a willing and relevant sounding-board, often at the expense of his own challenges and schedule. My parents-in-law for their assistance in proof-reading and my father, for proof-reading, formatting and constructive criticism.

And above all, I thank the Lord for allowing me this opportunity; for bringing me into contact with all these people and for upholding and sustaining me such that I am in a position to present this thesis.

© University of Pretoria

TABLE OF CONTENTS

© University of Pretoria

© University of Pretoria

© University of Pretoria

LIST OF FIGURES

© University of Pretoria

© University of Pretoria

Figures in Appendix

© University of Pretoria

LIST OF TABLES

Tables in Appendix

© University of Pretoria

NOMENCLATURE

α	Die half-angle
Δ	End displacement of fibre relative to the surface of the concrete matrix during a pull-out test
Δ	Ratio characterising the deformation zone of the die
ϵ	True strain
ϵ_p	Plastic strain
θ_0	Initial work hardening rate
κ	Bond modulus
μ	Coefficient of friction
μP	Average frictional stress
ξ	Damage coefficient for friction model
ρ	Density
σ	Normal stress
σ_ϵ	Evolvable component of yield stress
σ_ϵ^s	Saturation stress
σ_0^y	Initial yield stress
$\sigma_1, \sigma_2, \sigma_3$	Principal stresses
σ_4	Stage four flow stress
σ_b	Back stress
σ_d	Drawing stress
σ_m	Centreline stress
σ_u	Ultimate tensile strength
σ_y	Yield strength or flow stress
τ	Shear stress
A_0	Cross-sectional area of wire at entrance to die
A_1	Cross-sectional area of wire upon exit from die
C	Specific heat
c_4	Stage four work hardening rate
d	Displacement
E	Young's modulus
$\mathbb{E}$	Energy
F	Force
f'_c	Maximum compressive strength of concrete
G	Shear modulus
h	Hook depth
L_{eq}	Distance from die exit at which temperature gradient through the wire equilibrates
n_p	Number of points on a curve
P	Tensile load applied during pull-out
P	Normal pressure
r	Reduction associated with wire drawing
T	Torque
T_0	Temperature of the wire just before entering the die
T_{eq}	Equilibrated temperature through the wire at some distance from the die exit
T_{core}	Temperature of the core of the wire as it exits the die
T_{max}	Temperature of the surface of the wire as it exits the die
T_w	Temperature increase due to uniform deformation and redundant work

© University of Pretoria

CHAPTER 1 - OVERVIEW

1.1. CONTEXT

Concrete has been used in the construction industry for many centuries. On its own it has a strength in tension that is only a tenth of its strength in compression [1].This weakness can be overcome by introducing suitable reinforcing. For many years, the approach has been to establish an appropriate configuration of steel rods, encase this in a suitable mould and fill this with concrete slurry. Once the concrete has set and the mould has been removed (if appropriate) the end result will exhibit strength in tension and compression according to established models and well understood parameters.

In more recent times the notion of replacing the reinforcing rods with fibres has been explored, the anticipated benefits being substantial reduction in labour, cost, risk and complexity. Such fibres exist in various forms, configurations, dimensions and materials.

The classical [2] test to confirm the performance of a given fibre design in fibre-reinforced concrete is the pull-out test which measures force against slip to the point where the fibre is completely disengaged from the concrete.

1.2. PROBLEM DEFINITION

While attempts have been made to simulate the performance of such pull-out tests, in practice it has been found that there is a significant disparity between prediction and real-life performance. Research in this area is currently focused on how discrete portions of the pull-out curve are affected by controlled changes to known and easy-to-measure parameters such as strength of the concrete or the diameter of the fibre [3] [4] [5] [6] [7] [8] [9] [10] [11].

In all of these studies the fibre itself is assumed to be homogeneous. While this is a reasonable first approximation, it is widely known that the high strength of steel reinforcing fibres is a consequence of the cold wire drawing process and subsequent fabrication and the wire not having been annealed prior to further use. Residual stresses are known to exist in cold drawn wire as a consequence of the elastic response to a non-uniform distribution of plastic strain. This also introduces a yield strength profile where yield strength varies radially through the wire and is a function of the amount of plastic deformation experienced by different points within the wire. We see therefore that the properties of the fibre are in fact not homogeneous but are directly influenced by the wire drawing process and all subsequent manufacturing events.

The formation of residual stresses as a consequence of the wire drawing process has been widely studied [12] [13] [14] [15] [16] [17] [18] along with the effect of these stresses on aspects of service such as fatigue life [19] [20] [21] and sensitivity to corrosion [20] [22]. Their effect on the pull-out behaviour of steel reinforcing fibres, however, has not been well studied.

Previous studies [8] on the effect of increased yield strength due to plastic deformation have assumed that the area of increased yield strength is local in that it is confined to regions of obvious plastic deformation such as the bend radii of the hooked ends. A further assumption in this previous study is that yield strength does not vary with radial location within the wire.

These properties, i.e. the residual stress and yield strength profiles through the wire characterise the behaviour of the wire. The question therefore arises as to whether a fibre design that does not consider the starting material model or the consequences of the wire-drawing and forming processes will follow any predictable pattern of performance.

The information required to determine these properties (details of the wire drawing process and the exact material specification) will typically be unknown in practice. In order to overcome this, this study will use the results of a simulated hooked-end fibre manufacturing process and pull-out test to determine which aspects of the process are most relevant to the pull-out curve. In particular:

© University of Pretoria

- Plastic strain due to wire drawing
- Residual stress due to wire drawing
- Plastic strain and residual stresses due to forming of the hooked-ends
- The yield strength profile
- Particular combinations of residual stress profiles
- Stress-strain curve
- Hardening laws

We will then use the output of the above to determine whether sufficient information is made available in a tensile test, simple bend test and the pull-out test itself to fully characterise the material properties of the wire such that its performance in a pull-out test may be adequately predicted. In our further articulation below, the two variables we refer to are:

- Yield strength,
- Tangent modulus

1.3. OBJECTIVE

To determine whether the pull-out test on a steel reinforcing fibre provides enough information to define a starting material model that may be used for design and simulation of hooked-end steel reinforcing fibres as used in fibre-reinforced concrete.

1.4. GOALS

In pursuit of the above, our goals are to:

a) Understand the problem domain
b) Simulate the wire-drawing process and confirm the validity of our assumptions and approach
c) Simulate the hooked-end forming process
d) Simulate the pull-out test
e) Apply inverse analysis as per our starting objective.

1.5. CONSTRAINTS

There is no single standard for wire drawing and each process will have its own peculiarities. We therefore recognise that it is neither practical nor desirable that we attempt to simulate the entire wire-drawing process. Instead, we will endeavour to identify the salient aspects and, where appropriate, justify those which we will be omitting. We also recognise that the overall process including matters relating to the material, its preparation and handling are proprietary and that, as a consequence, we will need to work around this vast body of unknown information.

1.6. OVERVIEW OF THESIS

Chapter 2 presents the use of steel fibres as reinforcement in concrete and introduces the pull-out test as a means of testing fibre performance and comparing designs. Factors affecting the performance of reinforcing fibres are discussed with emphasis placed on the mechanical properties of the fibre. The mechanical properties are known to be a function of the wire drawing process, the basics of which are discussed with attention drawn to the effects of plastic deformation and residual stresses.

Simulation of the wire drawing process is examined in Chapter 3. A material model is defined based on fibre samples and real-world material properties. The scope is established through research and experimentation where any factor affecting residual stress profiles is relevant. After detailing the simulation the resulting residual stress and accumulated equivalent plastic strain profiles are presented and compared with those in literature.

Transfer of stress states from the 2D axisymmetric model used for wire drawing to the 3D models used for further study is verified and uniaxial tensile, torsion and bend tests are simulated on the as-drawn wire in Chapter 4. The hooked-end fibre is created through the simulation of a forming process and subjected to a pull-out test in order to obtain the known solution to the virtual problem. Sensitivity studies performed on the pull-out test establish which resultant properties from the wire drawing process are most critical in

© University of Pretoria

terms of predicting behaviour during pull-out. The effect of the coefficient of friction on behaviour during pull-out is also demonstrated.

The inverse problem is solved in Chapter 5 where the results of the tensile, bend and pull-out tests are used to estimate the stress-strain curve governing the behaviour of the wire during pull-out. Material models thus established are verified through comparison of the approximated pull-out curves with the baseline curve obtained in Chapter 4. The possibility of calibrating the material model directly from an experimental pull-out curve is also investigated.

Conclusions regarding the estimation of material models from the tensile test, bend test, and pull-out test are presented in Chapter 6. The three-variable problem requiring the solution to yield strength, tangent modulus and coefficient of friction is identified as an area for further study.

© University of Pretoria

CHAPTER 2 - THE PROBLEM DOMAIN

2.1. OVERVIEW TO THIS CHAPTER

In this chapter we will be examining concrete in general and steel-fibre reinforced concrete in particular. We will see that the study and design of steel reinforcing fibres to date gives limited consideration to the material properties of the fibre, i.e. those properties which are the consequence of the manufacturing process.

Since we know that reinforcing fibres are formed by means of a wire drawing process, we will also review the salient aspects of the real-world wire-forming process relevant to our study and will consider the following:

- The basics of the wire drawing process
- Plastic deformation and the resulting stresses due to wire drawing
- The significance of residual stress in wire

2.2. CONCRETE – EARLY HISTORY

Concrete is a building material composed of aggregates, cement and water, among other additions and additives. When water is added to cement the resulting calcium-silica-hydrate grows into crystalline and amorphous structures [23] that lock the added aggregates tightly together [24] and make concrete.

Humans have been using concrete as a building material for centuries. Some cite the first known example as being a crude concrete floor made from burnt lime plaster at a Neolithic Settlement in Galilee in approximately 7000BC. Other examples of the early use of concrete are parts of the Egyptian pyramids (approx. 2500 BC) and the Colosseum (70 AD) and Pantheon in Rome (118 AD) [24].

Concrete offers the advantage of being strong in compression [24]. Its strength in tension is however only a tenth of its strength in compression [1]. In 1867, Joseph Monier [25] patented a means to overcome cement's limited tensile strength using iron-wire reinforcement [26], thus giving rise to the concept of reinforced concrete.

Today, reinforcing bars, pre-stressed steel and steel wire reinforcement are all used in concrete structures to resist tensile stresses [27]. Steel is currently the most popular material for reinforcement due to the fact that the average value of its linear coefficient of thermal expansion is similar to that of concrete [27] and research has shown that the average nominal bond stress at failure of steel is greater than that for other materials like Fibre Reinforced Polymers [28]. Concrete reinforced with steel bars gives rise to a ductile composite material that has the existing strength of concrete in compression and the additional strength of steel in tension [29].

2.3. STEEL FIBRE REINFORCEMENT

In 1874 a patent was issued for reinforcing concrete with fibres and until the 1960s, they were believed to be able to enhance the tensile and bending strength of concrete [3] by delaying the widening of micro-cracks [30]. Since then however, no experimental evidence has emerged to support this [3].

Fibre reinforcement is particularly suited to the control of the cracking process since the fibres are small, closely spaced and uniformly distributed [1] over a greater area that can be covered by traditional reinforcement [30]. Including fibres in concrete also improves impact strength, toughness and durability [31] and fibres are easier to work with than traditional reinforcement [32].

Fibres may be made from many different materials [33]. Due to its previously discussed advantages, steel fibres will be considered in detail going forward.

In order to improve the mechanical bond between the fibre and the concrete, steel fibres may vary by manufacturing process, shape and length [31] where the shape is often a function of the manufacturing process [34] [35]. In particular, the cold-drawn manufacturing process will be considered for fibres

© University of Pretoria

modified by bending, flattening or roughening [34]. Some different shapes of steel fibres are depicted in Figure 2-1. The hooked-end fibre will be the focus of this study since it is the most popular and most successful shape and has been on the market for over 25 years [36].

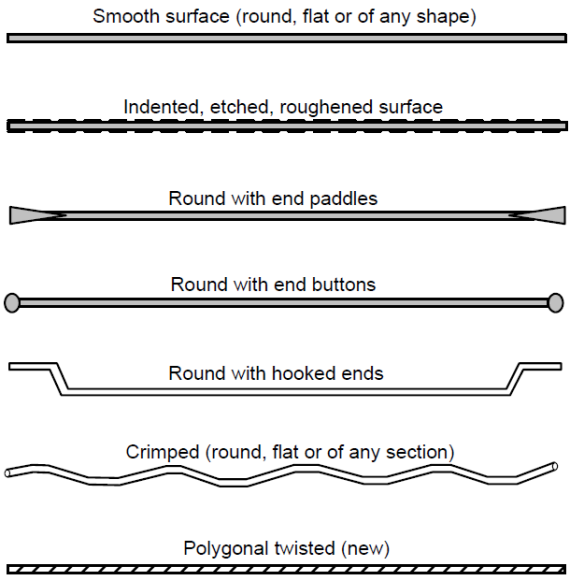

Figure 2-1 Typical profiles of steel fibres for use in concrete [4]

2.4. APPLICATIONS AND GENERAL SPECIFICATION

Steel reinforcing bars and steel fibre reinforcement are not equivalent and the specific application will dictate which method is most applicable [37]. Some structures such as foundations, certain walls [38] and elevated slabs [39] may be cast with steel fibre reinforcement taking the place of steel reinforcing bars. Others will require a combination of fibres and bars [30]. For beams in particular, certain requirements must be met before fibre-reinforced concrete is permitted as an alternative to shear reinforcement [40].

The design and use of steel reinforcing fibres is currently unregulated in South Africa [41] [42] [43] and typical international standards provide little information outside of tolerances and mechanical strength requirements [34] [35]. References such as the *fib* Model Code 2010 [44] are however available, and the contents thereof are likely to be incorporated in future versions of international standards as the use of fibre-reinforced concrete increases in popularity. Analytical and experimental studies suggest that the following guidelines should be followed in the specification of steel fibres for reinforcement [4]:

- Fibres should have a tensile strength that is two to four times higher than the compressive strength of the concrete
- The strength of the bond between the fibre and the concrete matrix should be at least the same order of magnitude as the tensile strength of the concrete
- The tensile modulus of elasticity of the fibre should be at least three times higher than that of the concrete
- The thermal expansion coefficient and Poisson's ratio of the fibre should have the same order of magnitude as the concrete

2.5. PERFORMANCE OF PLAIN AND FIBRE-REINFORCED CONCRETE

The main reason for the low tensile strength of concrete is the existence of micro-cracks and their growth under loading due to the difference in stiffness between the aggregate and the cement [30]. A typical stress-strain curve for concrete under a uniaxial compression load is given in Figure 2-2.

At low stresses, the stress-strain relationship is linear. Departure from the linear relationship occurs when the micro-cracks extend past the aggregate-cement interface and into the cement. Increased non-linearity indicates the formation of crack networks. At maximum compressive strength, f'_c, the load is carried entirely by the un-cracked portions of the concrete. Thereafter, the ability of the concrete to resist the compressive load decreases gradually [27].

© University of Pretoria

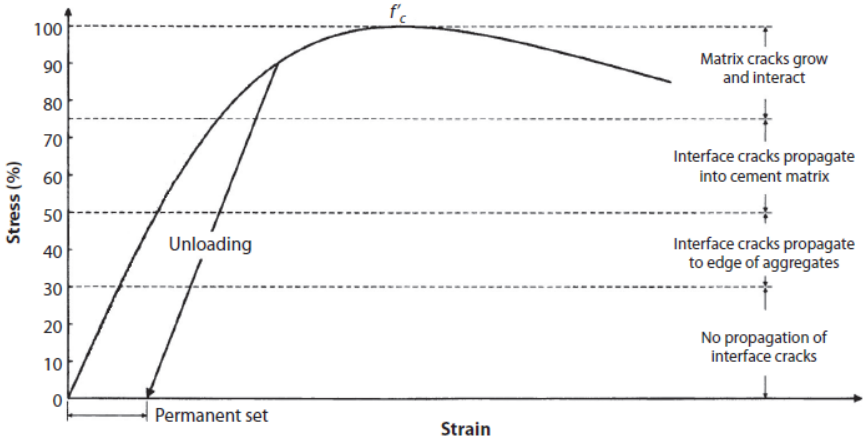

Figure 2-2 Generalised stress-strain curve for concrete in compression [27]

In plain concrete, shear stresses are transferred across cracks by the interlocking action of the aggregates and friction at the faces of the crack. Since the bond between the steel fibre reinforcement and the concrete allows for the transfer of loading, a tensile load applied to fibre reinforced concrete results in some of the load being carried by the fibres and the rest carried by the concrete [30] thereby increasing the toughness or energy absorption capability of the concrete [5]. This is represented schematically by the stress-strain curves in Figure 2-3.

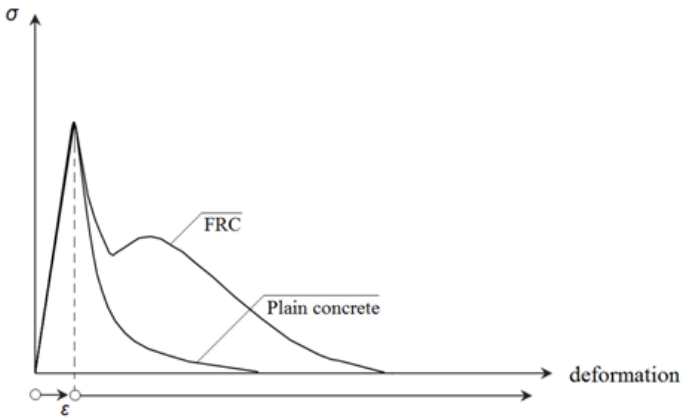

Figure 2-3 Fibre reinforced concrete and plain concrete under tension [45]

For plain concrete under tension, the strength limit is attained quickly, cracks form almost immediately, and the strength of the concrete deteriorates rapidly. Figure 2-3 indicates that the addition of fibre reinforcing to concrete modifies the behaviour of the concrete under tension so that it starts to approximate the behaviour under compression as given by Figure 2-2. The aim of any design of a reinforcing fibre is therefore to maximise the area underneath the stress-strain curve for tensile loading.

The role of fibre reinforcement is to improve resistance to cracking rather than increase the overall deformation capability of the concrete itself. Resistance to failure may be enhanced by either increasing the path the cracks will have to follow during separation or by increasing the fibre's ability to deform [5].

2.6. TESTING THE PERFORMANCE OF HOOKED END FIBRES

The main reinforcing action associated with steel fibres occurs after the concrete matrix has already cracked. Failure occurs when sufficient energy has been absorbed in widening the crack so that the bridging fibre pulls out of the concrete matrix. The mechanical behaviour of fibre reinforced concrete is therefore related to the pull-out load-slip behaviour of the individual reinforcing fibres [30].

A convenient test which replicates the extraction of a bridging fibre under conditions of crack growth is the pull-out test where the relationship between pull-out load (force) and fibre end displacement (slip) is

© University of Pretoria

recorded. The total energy that is absorbed or dissipated during the test is equal to the area underneath the load-displacement curve [46]. These curves are also used as a means for comparing fibres of different materials and quantifying the effect of changing various factors [30].

2.6.1. Pull-out curve

In the pull-out test, a fibre is embedded in a cementitious matrix for a certain length and is subjected to a tensile load P applied to the protruding tip. Assuming the fibre is able to be withdrawn in its entirety without breaking, the pull-out curve is generated by measuring the change in load with increasing displacement Δ relative to the surface of the matrix [5].

2.6.1.1. Straight steel fibre

The pull-out curve for a straight steel fibre is discussed first in order to highlight the difference that is brought about as a result of the mechanical features of the hooked-end fibre. The pull-out curve of a straight steel fibre is represented schematically in Figure 2-4.

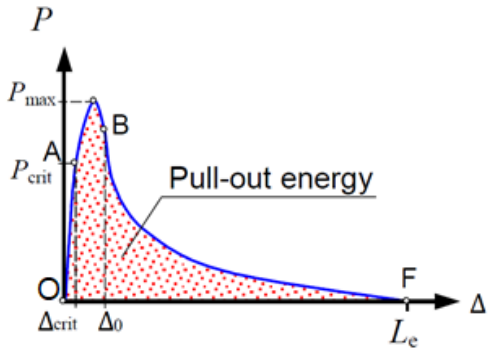

Figure 2-4 Pull-out curve for a straight steel fibre [30]

Key stages and points in the curve are given as follows:

a) O-A In the *pre-critical region* the fibre is assumed to be elastically bonded to the concrete matrix along its entire embedded length [5]. The limited displacement is a result of elastic deformation in the bond and that portion of the fibre not encased in concrete [30].
b) A-B During *initiation and progression of de-bonding* [30] only part of the fibre is bonded, with the behaviour of the bond governed by the maximum elastic bond shear stress and initial frictional shear stress [5].
c) B The point of *full de-bonding* [30] does not necessarily coincide with the point of maximum pull-out load [6] but depends on the relationship between the applied force and the progression of de-bonding [30].
d) B-F In the *pull-out region* [30] the fibre is completely de-bonded and behaviour is governed solely by frictional shear [5]. Load decreases with increased slip due to decreasing fibre embedded length and most likely, a slip-decaying friction model [30].

2.6.1.2. Hooked-end fibre

The pull-out curve for a hooked-end fibre in comparison with a straight fibre is represented schematically in Figure 2-5. It is noted that the pull-out process of the hooked-end fibre is similar to that of a straight steel fibre up to the point of complete interfacial de-bonding. After this point, experimental evidence suggests that resistance to pull-out is primarily provided by the mechanical contribution of the hook in the hooked-end fibres [6].

The curve may be broken down into stages as follows:

a) O-A Fibre response during the *elastic or adhesive bond* [30] stage is elastic [7]
b) A-B During *initiation and progression of de-bonding* [30] de-bonding occurs between the straight portion of the fibre and the surrounding concrete matrix [11].
c) B Just after *full de-bonding* [30] there is no displacement of the hooked portion of the fibre within the duct. Any displacement of the end of the fibre is elastic and relates only to the straight portion of the fibre [7].

© University of Pretoria

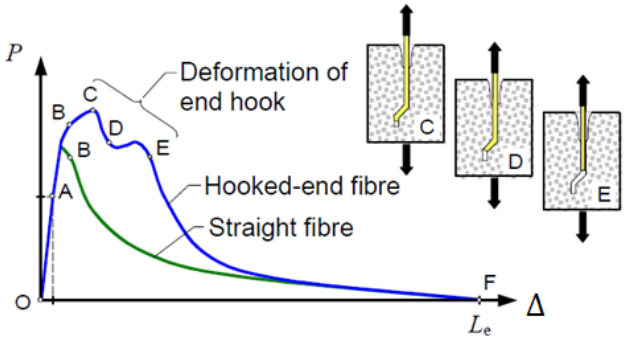

Figure 2-5 Comparison of pull-out curves for straight and hooked-end fibres [30]

d) B-C *Increase in load due to mechanical anchorage* [30]. The portions of the fibre that make up the bend radii are forced against the upper surfaces of the concrete duct creating reaction forces that cause plastic deformation. The fibre begins sliding in the duct when a plastic hinge has formed at the bend radius [46].
e) C *Maximum pull-out force* [30] occurs at the point where the midpoints of the bend radii (points G2 and G3 in Figure 2-6) have respectively entered the inclined and straight segments of the concrete duct [7].

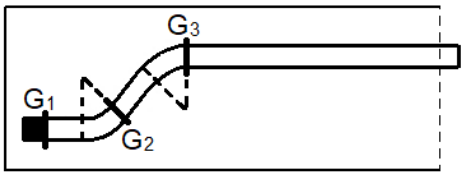

Figure 2-6 Maximum pull-out force [7]

f) C-D During *slip and plastic deformation of fibre* [30] the pull-out load decreases while the midpoints of the bend radii move along the inclined and straight segments of the duct [7]. The load decrease is attributable to reduced friction due to the reduced embedded length of the fibre [30].
g) D-E The *increased load required to continue plastic deformation* [30] is governed by reverse bending in the last bend radius (with midpoint G_2) [11] as depicted in Figure 2-7.

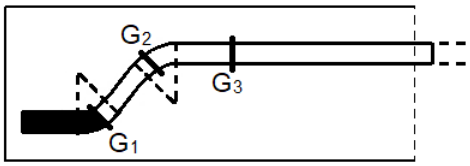

Figure 2-7 Increased load to continue plastic deformation [7]

h) Pull-out load then decreases due to the fact that plastic deformation is now only occurring in the end of the fibre as it is being pulled out of the inclined segment of the duct [7] as depicted in Figure 2-8.

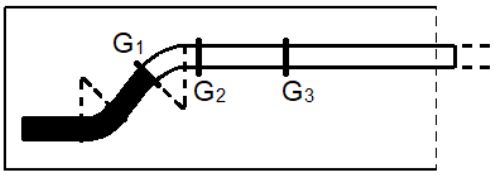

Figure 2-8 Reduced load due to straightened hook [7]

i) E-F *Frictional decaying process due to fibre pull-out* [30] begins when the end of the fibre is in alignment with the straight section of the concrete duct and there is no further plastic deformation [46]. The load is governed by local friction at three points of contact between

© University of Pretoria

the fibre and the duct walls due to incomplete straightening as depicted in Figure 2-9. Some authors state that the frictional force in this stage is relatively constant [46] [11] while others note a decaying frictional force [30] [4].

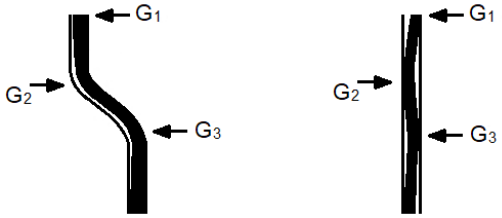

Figure 2-9 Hook geometry as pull-out begins (left) and after pull-out (right) [7]

2.7. FACTORS AFFECTING THE PERFORMANCE OF HOOKED-END FIBRES

Examination of a number of pull-out tests performed under various conditions allows conclusions to be drawn regarding the factors that govern the effectiveness of a given reinforcing fibre in transferring stress. The following (in no particular order) will be shown to have the largest influence [9]:

- Bond between the fibre and the concrete matrix, including friction
- Geometric properties including length, diameter, aspect ratio and ratio of perimeter to area
- Orientation of the fibre with respect to applied loads
- Mechanical features, including both mechanical deformation and material properties

2.7.1. Bond

The bond allows forces to be transmitted between the fibre and the cement matrix and affects all stages of the pull-out process [30]. There are four components to the bond:

a) *Adhesion* between the fibre and the cement matrix, can be physical or chemical [6]. This aspect has been shown to only affect the ascending branch of the pull-out curve [5].
b) *Friction* is a mechanical bond that can be constant or varying [6] and affects all stages of the pull-out curve. Three models are available to describe the behaviour: constant friction, decaying friction and slip-hardening friction [30]. More detail is given in Section 2.7.1.1.
c) The *mechanical* component is associated with fibre geometry [6]. Mechanical deformation of the fibre has been shown to be the most effective means of improving bond strength [7]. More detail is given in Section 2.7.4.1.
d) *Interlock* or interconnection between the fibres [6], depends on mechanical features and number of fibres per unit volume of concrete [11].

2.7.1.1. Friction

Constant friction models have a uniform effect on the magnitude of the load at all stages of pull-out [8]. It is simple to simulate and does not require calibration using experimental observations. This will be the chosen friction model for this study.

Proponents of the decaying frictional model depicted in Figure 2-10 observe that frictional shear stress deteriorates and decreases as the slip between the fibre and the concrete matrix increases, possibly due to the cement matrix crumbling and acting as rollers in the duct as the fibre is pulled out [5].

In Figure 2-10, ξ is the dimensionless damage coefficient parameter which represents the rate of deterioration of the frictional shear stress due to the crumbled cement in the fibre duct. The damage coefficient can be varied to model either constant or decaying friction [5]. Its value is usually chosen so as to give the analytical descending branch of the pull-out curve the same decaying trend as seen in an experimental curve [6].

© University of Pretoria

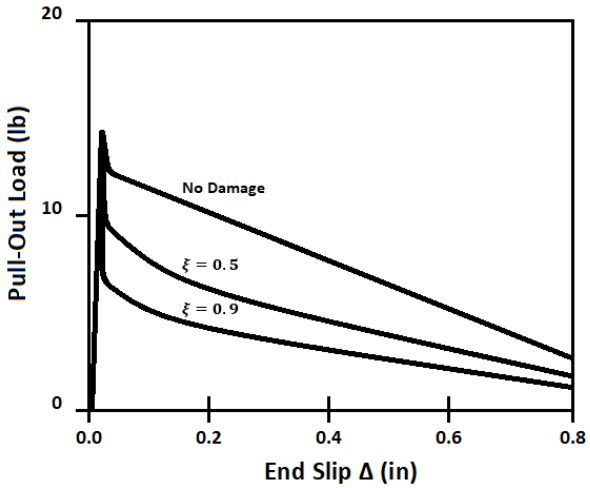

Figure 2-10 Effect of decaying friction on the descending branch of the pull-out curve [5]

The slip-hardening friction model is not commonly used. Typical instances of applicability include the modelling of high-performance fibre-reinforced cement composites [4].

2.7.2. Geometric properties

A lack of knowledge regarding the behaviour of deformed fibres has led to commercial geometries that are intuitive rather than optimised [7] despite the fact that geometry is known to have the greatest contribution to peak load and total work done during pull-out [9]. The effect of the following geometric properties is summarised below:

a) Increased *embedded length* increases peak load [9] and more than increases total work done during pull out, provided the normal stress along the fibre does not result in fracture [5].
b) There is a direct relationship between *diameter* and peak load [4]. For hooked-end fibres, larger diameters require more energy for plastic deformation resulting in increased work [7].
c) Total work done is more than proportional to increasing *aspect ratio* [5]. Its efficacy is however limited by an increased tendency for fibre entanglement during mixing [33].
d) An increased *ratio of perimeter to cross-sectional area* results in increased frictional and adhesive bond forces along the fibre and concomitant increase in peak load [4].
e) *Mechanical deformations* have an active effect on pull-out and will be discussed in Section 2.7.4.

2.7.3. Orientation

Studies show that orienting reinforcing fibres at different angles of inclination results in increased total work done during pull-out but not necessarily increased peak load [30]. The inclination of the fibre provides an additional opportunity for plastic deformation as the fibre attempts to straighten in line with the direction of loading [7].

It stands to reason that no practical steps can be taken to align fibres in the direction of potential loading during the concrete casting process. It is therefore convenient that studies indicate that the random orientation of the fibres with respect to loading results in an overall increase in strength [30]. This study will consider fibres oriented in the direction of loading only.

2.7.4. Mechanical features

2.7.4.1. Mechanical clamping

This is a mechanical component of the bond and refers to the cold-working and subsequent deformation of the hooked-end of the fibre during pull-out [6]. Many studies confirm the effect of this geometrical component on increasing total work done [6] [7] [9] [46].

2.7.4.2. Material properties

Experimental results show that the mechanical clamping effect is independent of concrete matrix strength and length of fibre embedment, but is dependent on fibre material properties and the geometry of the hook [6]. Since the effect of hook geometry has been confirmed to be well known, the effect of material properties warrants detailed examination.

© University of Pretoria

2.7.4.2.1. Strength

A steel reinforcing fibre fails if it fractures before being completely withdrawn from the cement duct. It therefore stands to reason that the higher the tensile strength of the fibre, the lower the likelihood of failure [7].

Strength may also be equated to the load a material can withstand before yielding. Peak load has been shown to be directly related to the commencement of plastic deformation of the hooked-ends of the fibre [7] [8].

2.7.4.2.2. Elasticity

Both elastic modulus and shear modulus only affect the behaviour of the hooked-end fibre in the pre-critical, elastic bond region of the pull-out curve. There is therefore little to no effect on pull-out [5] [8].

2.7.4.2.3. Plasticity

The cold work required to form plastic hinges at both bend radii increases the peak pull-out load. The load value drops to a second maximum as soon as the fibre has been pulled out sufficiently so that only one active plastic hinge remains [6]. Such cold-work results in a local increase in yield strength at the bend radii which studies have shown should be included in the simulation of pull-out [8].

It is axiomatic that in order to deform plastically, the material in the bend radius of the hook must be exposed to stresses in excess of the material yield strength hence requiring a larger stress to continue deformation [12]. The behaviour of a fibre is therefore affected by the extent to which the material can work-harden before fracture as determined by the fibre manufacturing process and the work hardening behaviour of the material.

Many different models exist for simulating the behaviour of materials after the elastic limit. Some studies make use of isotropic elastic linear hardening models [8] [47]. Other studies limit the description of hardening behaviour to isotropic without providing further detail regarding the flow curve [17] [48]. Studies considering kinematic hardening behaviour could not be found.

2.8. OVERVIEW OF REAL-WORLD WIRE FORMING

2.8.1. Major considerations

It is common knowledge within the industry that the wire-forming process results in a product with an increased yield strength and reduced ductility. Residual stresses are known to exist in cold drawn wire as a consequence of elastic response to a non-uniform distribution of plastic strain [17]. The effect of these stresses on pull-out behaviour has not been well studied.

It is recognised that the wire drawing process will introduce a yield strength profile where yield strength varies radially through the wire and is a function of the amount of plastic deformation experienced by different points within the wire. Previous studies on the effect of increased yield strength due to plastic deformation on pull-out have made the following assumptions [7] [8] [30]:
a) The area of increased yield strength is confined to the bend radii of the hooked ends
b) Yield strength does not vary with radial location within the wire
In the sections that follow, an overview of real-world wire forming will be presented.

2.8.2. Basics of the forming process

Drawing is a cold metal forming technique where a tensile force applied to the metal at the exit side of a die causes the metal to change shape as it is pulled through the die [12]. This produces rods, pipes and wires with a fine microstructure and improved mechanical properties [49].

The starting product for wire drawing is hot-rolled wire rod, the surface of which is cleaned and prepared before being lubricated and drawn through the die. Coarse wires with a final diameter

© University of Pretoria

greater than 6.35 mm are typically formed in a single step while several passes are required for fine wires [12]. The die for wire drawing is typically a modified cylinder as depicted in Figure 2-11 with specific features highlighted as follows [12] [13] [14]:

a) *Bell* or *entry zone*: Has a flared profile and a diameter much larger than the product entering the die so as to protect the product surface from damage due to the die edges
b) *Entrance angle* or *lubricating cone*: Provides the transition from the bell to approach angle, ensures that lubricant is drawn evenly into the die
c) *Approach angle* or *working cone*: Location of reduction in diameter, characterised by the half-die angle, α. The included angle of the die is given as 2α.
d) *Bearing length* or *land*: No diameter reduction, guides the wire as it exits the die
e) *Back relief* or *exit zone*: Provides dimensional stability to the die and protects product surface from damage due to the die edges

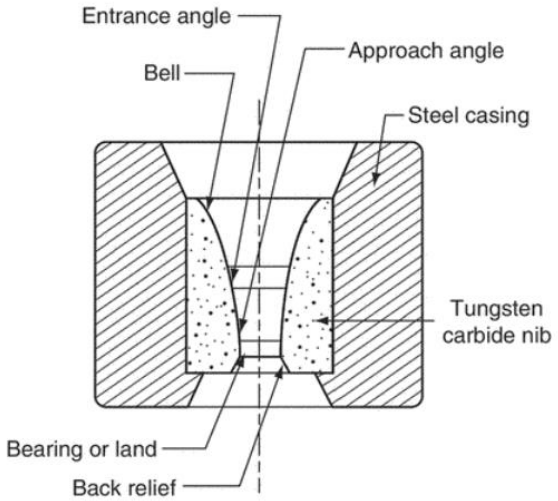

Figure 2-11 Wire-drawing die nomenclature [14]

2.8.3. Plastic deformation and resulting stresses

Stresses on the wire during the drawing process are depicted in Figure 2-12 where σ_d is the drawing stress, σ_b is the back stress, σ_m is the centreline stress, P is the normal pressure and μP is the average frictional stress [14].

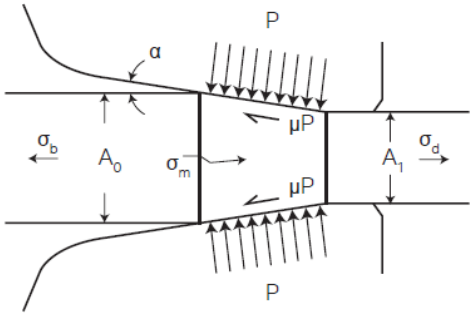

Figure 2-12 Stresses on wire during the drawing process [50]

The drawing stress results from the traction force pulling the wire through the die. Back stress acts in the opposite direction to the drawing stress [14] and may or may not be present in any given drawing process [50]. Centreline stresses may be positive or negative, with positive or tensile values increasing the likelihood of fracture during drawing [14]. The normal pressure acts to compress the wire and deform the material [50]. Average frictional stress is assumed to be proportional to the normal pressure at any point in the die according to Coulomb's law of friction and acts in a direction opposite to the motion of the wire [12].

© University of Pretoria

The nature of the deformation experienced by the wire in the drawing process may be described as non-uniform plastic deformation: Plastic flow at the surface is greater than that at the centre resulting in a residual stress distribution through the wire [12]. During drawing, axial stress varies from zero at the entrance of the die to a maximum at the die exit and is limited by the tensile strength of the wire at the exit. Tangential and radial stresses are equal and compressive and related to the axial stress by a yield criterion. After drawing, residual stresses on the wire surface are compressive only when reductions in area are small (less than 1%), otherwise they are tensile [15].

2.8.4. Significance of residual stress

Uniaxial tensile tests performed on a wire after cold-drawing allow one to conclude that the wire is brittle by virtue of the small area under the stress-strain curve. This is depicted in Figure 2-13 which compares the stress-strain curves for a cold drawn wire before and after drawing.

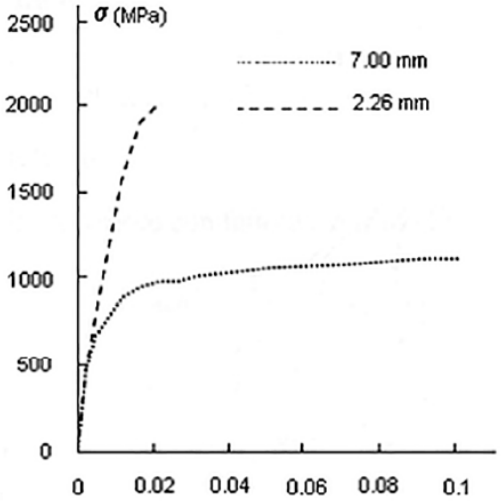

Figure 2-13 Comparison of stress-strain curves before and after drawing [49]

Even so, cold drawn wires are known to have considerable ductility since they may be repeatedly bent and twisted without failure. The ductile nature of failure during a uniaxial tensile test has been confirmed by examination of the fracture surface. The apparent contradiction between these two states (brittle according to the stress-strain but ductile in practice) is resolved by considering the existence of residual stresses inside the wire [47]. The effect of residual stresses on the stress-strain curve resulting from a tensile test is illustrated in Figure 2-14 for a wire at a drawing strain of 3.5 resulting in a tensile strength of 2770 MPa.

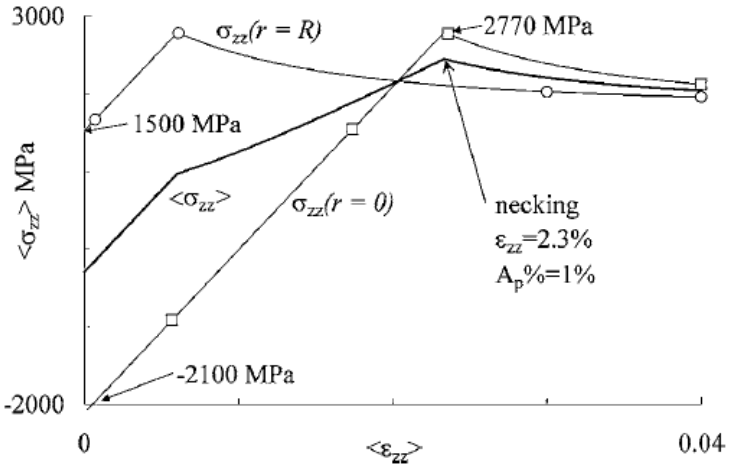

Figure 2-14 Average stress-strain curve as influenced by residual stresses [47]

In Figure 2-14, local (residual) axial stress-strain curves are given for the wire at the surface (circles) and at the centre (squares). The stress-strain curve of the wire under uniaxial tension (solid line) is

© University of Pretoria

determined by averaging these axial residual stress curves. We see therefore that the large plastic deformations imposed on the wire by the drawing process lead to a loss in hardening capabilities and the appearance of brittleness during a uniaxial tensile test. Ductility is however preserved as a result of the residual stresses inherited from the drawing process [47].

2.9. SUMMARY

Since the strength of concrete in tension is only a tenth of its strength in compression, most concrete is reinforced before it is used in structural applications. Steel is a popular material for reinforcement due to the fact that a superior bond is formed between steel and concrete when compared to other reinforcing materials. The only practical means of increasing the tensile strength of concrete meaningfully is through the use of steel reinforcing bars (rebar). Steel fibres oriented across a crack can absorb energy by deforming and pulling out. While fibre reinforcement cannot at this stage entirely replace traditional rebar reinforcement, it has been shown to be particularly suited to the control of the cracking process.

The pull-out test is a convenient means of replicating the extraction of a bridging fibre under conditions of crack growth. The resulting load versus pull-out curves can be used as a means of comparing fibre designs. The most popular form of steel reinforcing fibre is the hooked-end fibre since the mechanical contribution of the hook allows for significantly more energy to be absorbed during pull-out. Experimental studies have shown that this additional capability for absorbing energy is solely due to the plastic deformation experienced by the hooked end.

Plastic deformation of the hooked end is related to the material properties of the fibre, an area which is noted as relatively underdeveloped in the field. Such properties are known to be directly affected by the manufacturing process, in this case, cold wire-drawing and cold forming of the hooked ends.

Residual stresses are known to exist in cold drawn wire as a consequence of elastic response to a non-uniform distribution of plastic strain. It is further recognised that the wire drawing process will introduce a yield strength profile where yield strength varies radially through the wire and is a function of the amount of plastic deformation experienced by different points within the wire. Our research has shown that the effect of residual stresses on the pull-out behaviour of steel reinforcing fibres has not been well studied. Furthermore, previous studies on the effect of plastic deformation on the pull-out curve have assumed that the fibre is homogeneous.

This has led to current geometries for steel reinforcing fibres that are intuitive rather than informed, a situation that is not easily rectified due to disparity between simulated prediction and real-life performance. It is therefore evident that an understanding of the effect of the fibre manufacturing process on the pull-out curve is required.

© University of Pretoria

CHAPTER 3 - SIMULATING THE WIRE DRAWING PROCESS

3.1. OVERVIEW OF THIS CHAPTER

We recognise that it is not practical to simulate the entire wire forming process in order to obtain the exact residual stress and yield strength profiles of the wire before examining the design of the fibre. A further challenge exists in that the real-world wire-drawing process is proprietary and therefore likely to be unknown in practice. The only facts available are the properties of the final product evident from tests and observations we might make about the final product.

Our approach therefore is to model a wire-drawing process on a range of starting material models until we find one that will result in the final state we have observed in a real-world product. We will then seek to confirm our model by comparing the results to those obtained from literature. It is beyond the scope of this exercise to develop a comprehensive wire drawing simulation and several simplifications were embraced in order to maintain the focus of this study.

It is assumed that the variables in the wire drawing process may be studied independently and that their effect on the residual stress and yield strength profiles may be quantified separately. Variables of interest are those that affect the shape of the profiles. Variables that only affect magnitude will not be studied in detail.

In order to gain this understanding, this chapter will:

- Present wire drawing simulations found in literature
- Identify an appropriate starting material model
- Identify and consider aspects evident from the real-world wire-drawing environment
- Identify and consider lessons learned from related exploratory simulations
- Simulate the production of a steel wire through wire drawing
- Confirm the relevance of our simulation by comparison to real-world simulations found in literature

3.2. SIMULATIONS IN LITERATURE

3.2.1. *Atienza et al.*

Atienza et al. [17] studied residual stresses in cold drawn ferritic rods using a two-dimensional axisymmetric model with isochoric plastic deformation, excluded phase transformation, accounted for mechanical and thermal aspects, used prescribed displacements and defined contact with an unspecified friction coefficient. Simulated residual stress profiles were verified by comparing the results with experimental profiles obtained using neutron and x-ray diffraction.

Figure 3-1 gives the resulting simulated and experimental residual stress profiles. Circles, squares and triangles denote the axial, radial and hoop residual stress profiles respectively.

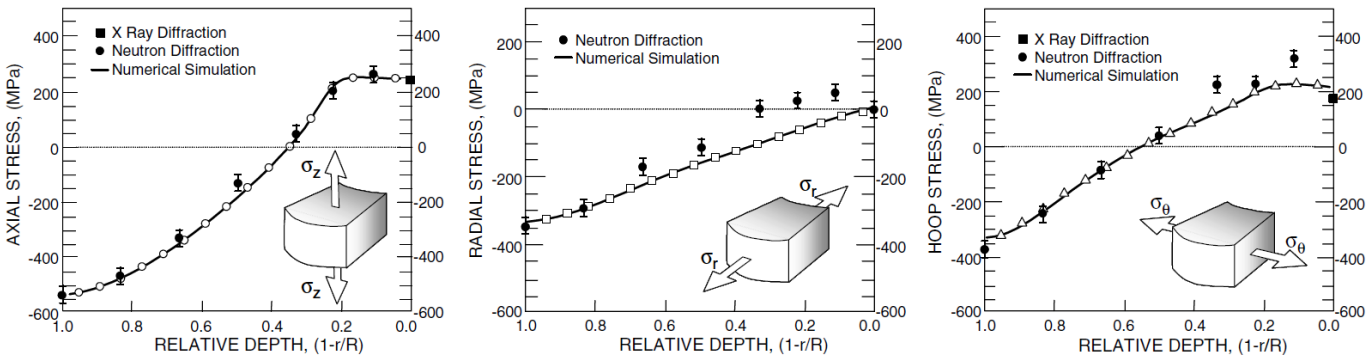

Figure 3-1 Numerical and experimental residual stress profiles [17]

© University of Pretoria

3.2.2. He et al.

He et al. [18] used a two-dimensional axisymmetric model, a friction coefficient of 0.03, isotropic non-linear elastic-plastic material, Von Mises yield criterion, assumed low temperature and low drawing speed and determined the flow stress experimentally using tensile tests. Simulated residual stress profiles were verified by comparing the results with x-ray diffraction measurements at the surface of the wire.

3.2.3. Phelippeau et al.

Phelippeau et al. [47] used a two-dimensional axisymmetric model with non-linear geometry, unilateral hard contact between die and wire, assumed isotropic elasticity and plasticity, Von Mises yield criterion and linear isotropic work hardening. Simulated residual stress profiles were verified by comparing the stress-strain curve from a subsequent simulated tensile test with that of an experimental tensile test. A drawing strain of 3.5 with a resulting tensile strength of 2770 MPa was considered for the wire.

Figure 3-2 gives the resulting simulated residual stress profiles. Circles, squares and triangles denote the axial, radial and hoop residual stress profiles respectively.

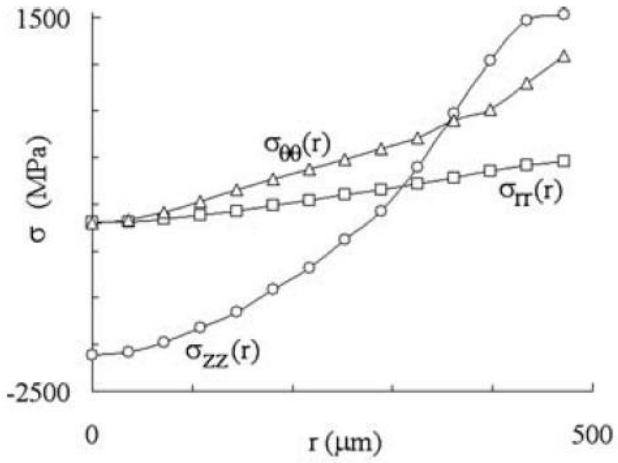

Figure 3-2 Numerical residual stress profiles [47]

3.2.4. Toribio et al.

Toribio et al. [48] studied residual stresses in cold-drawn pearlitic steel wire using a two-dimensional axisymmetric six-pass model with Von Mises yield criterion and associated flow rule, isotropic strain hardening, a rigid tungsten carbide die with $\alpha = 3.5°$ and frictionless contact.

3.3. THE MATERIAL MODEL

3.3.1. Overview

In this context, the term 'material model' refers to the feedstock to the wire-drawing process. The purpose of a material model is to provide a relationship between stress and strain such that stress may be predicted for any given value of strain [51]. This model plays a crucial role in our simulation of the wire-drawing process and this section explains the basis for our various choices in specifying and defining that model.

3.3.2. General material specification

We restrict our investigation to carbon steel for two reasons:
a) To contain the scope of this investigation and
b) Based on the work of Callister [52], we have concluded that the reinforcing fibres are most likely made from low carbon steel with a carbon content of approximately 0.1 – 0.2%.

To ensure that realistic assumptions were made regarding the material model, hooked-end steel reinforcing fibres were obtained from a company in Randburg that specialises in seamless concrete

© University of Pretoria

flooring. The fibres used by this company are proprietary and limited information was available. The datasheet given in Figure A-4 in Appendix A gives approximate information on the fibres and was used as a starting point. We note that the datasheet reports a minimum tensile strength value of 1200 MPa which was confirmed by laboratory uniaxial tensile tests conducted on three fibres. The tests also revealed ultimate tensile strength (UTS) in excess of 1500 MPa. Results of the tests are given in Table A-1 in Appendix A.

3.3.3. Yield criterion

The yield criterion is required to establish a relationship between the multiaxial stress state and the uniaxial yield strength [53]. The Von Mises yield criterion was chosen for this study on the basis that it provides the best correlation with experimental data [12].

It is recognised that the Von Mises yield criterion is only applicable to isotropic materials [52]. The material structure of cold drawn low-carbon steel is known to be primarily ferritic [14]. A ferritic material structure lends itself to the assumption of isotropy [14] unlike a pearlitic structure, for example, which is anisotropic. Consideration of other yield criteria for anisotropic materials, such as the Hill Yield criterion, is therefore not necessary. The wire drawing process simulated in this study therefore additionally assumes that the workpiece material is isotropic.

3.3.4. Evolution of stress with plastic strain

Strain-rate-independent plasticity was assumed in the development of the constitutive equation for plastic strain. The response of the material therefore does not depend on the rate of deformation. The basis for this assumption is given in Section 3.5.4.2 where the strain rate was shown to have no effect on the residual stress profile and could therefore be neglected.

3.3.4.1. Flow rule

When the initial yield surface evolves, a flow rule is required to define the stress state on the subsequent surface with respect to the state on the initial surface. The associated flow rule was selected since it is relevant in modelling the behaviour of metals [53]. It is illustrated in Figure 3-3.

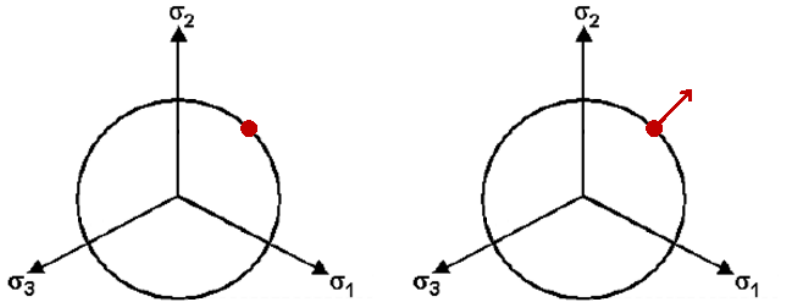

Figure 3-3 Stress state on evolved yield surface with respect to the initial surface [54]

A feature of the associated flow rule as highlighted in Figure 3-3 is that the direction of plastic flow is normal to the yield surface [53]. This means that the direction of the plastic strain increment is the same as the direction of the stress increment and increments in plastic strain are therefore proportional to increments in stress [55]. The constitutive equation defined for the material model must therefore specify a direct relationship between stress and plastic strain.

3.3.4.2. Hardening rule

The manner in which the yield surface evolves due to increasing strain must be specified. Two generally accepted models of modified yield surfaces are isotropic hardening, where the yield surface expands without changing shape as illustrated in Figure 3-4 and kinematic hardening, where the yield surface remains the same size and shape but translates as illustrated in Figure 3-5 [54].

© University of Pretoria

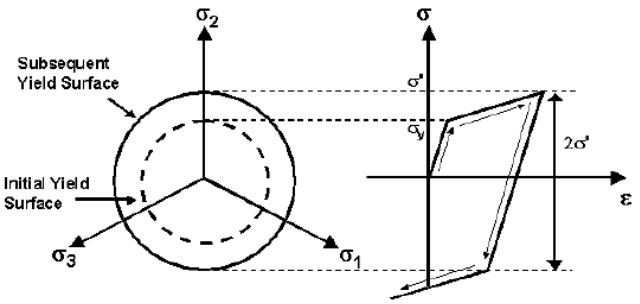

Figure 3-4 Isotropic Hardening [54]

The isotropic hardening rule is generally applicable to the analysis of metals subjected to large strains. The growth of the elastic domain in isotropic hardening means that the yield strength under conditions of reversed loading will be greater than the initial yield strength of the material. This rule is therefore unable to model the Bauschinger effect and is suitable for proportional loading conditions only [54].

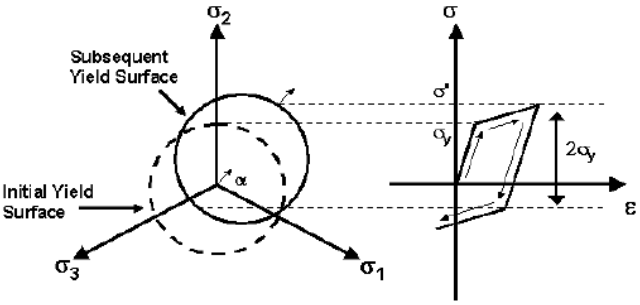

Figure 3-5 Kinematic hardening [54]

The translation of the yield surface as a rigid body is useful in modelling behaviour such as the Bauschinger effect [55]. This means that the kinematic hardening rule is generally applicable to analysis of metals subjected to small strains and applications involving non-proportional, cyclic loading [54].

Loading may be considered to be proportional if the ratios between the principal stresses remain constant under the applied load [54]. Since the simulation of the wire drawing process involves large strains and proportional loading, isotropic hardening was chosen as the work hardening rule for this study.

3.3.4.3. Constitutive equation for work hardening law

The constitutive equation for work hardening allows one to calculate the flow stress of the material for a known value of equivalent plastic strain [56]. One must however note that plasticity is path dependant. Equivalent plastic strain is a means of converting a three-dimensional strain to an equivalent scalar strain quantity. While this facilitates the use of a one-dimensional stress-strain curve in three-dimensional cases; it is clear that the same scalar quantity will result from different combinations of three-dimensional plastic strain increments [51].

Equivalent plastic strain is therefore not able to uniquely describe the state of the material. Flow stress does however qualify as a state variable [56] since it physically correlates to the actual microstructural state of the material [51]. The work hardening model selected for this study models the flow stress σ^y as:

$$\sigma^y = \sigma_0^y + \sigma_\epsilon \quad (1)$$

© University of Pretoria

where σ_0^y is the initial yield stress and σ_ϵ is the evolvable component of the yield stress. The constitutive equation must therefore describe the change in the evolvable component with a change in plastic strain [51].

Stage IV Voce hardening is a model that is known to be able to accurately depict linear hardening behaviour at large strains [57] [58]. Since large strains are a consequence of the wire drawing process, this model was chosen to describe the evolution of the yield stress. The Stage IV Voce hardening model is given by [58]:

$$\frac{d\sigma_\epsilon}{d\epsilon_p} = \theta_0\left(1 - \frac{\sigma_\epsilon}{\sigma_\epsilon^s} + \frac{\sigma_4}{\sigma_\epsilon}\right); \qquad \frac{d\sigma_4}{d\epsilon_p} = c_4 \tag{2}$$

where:
- θ_0 is the initial work-hardening rate
- σ_ϵ^s is the saturation stress
- ϵ_p is plastic strain
- σ_ϵ is the evolvable component of the flow stress
- σ_4 is the stage IV flow stress
- c_4 is the stage IV work hardening rate

3.3.4.3.1. *Initial work-hardening rate θ_0*

The initial work-hardening or strain-hardening rate, θ_0, is a scaling parameter and is generally of the order:

$$\theta_0 = \frac{G}{100} \tag{3}$$

where G is the shear modulus [56].

3.3.4.3.2. *Saturation stress σ_ϵ^s*

The saturation stress, σ_ϵ^s, may, under certain circumstances, be thought of as the maximum attainable stress in a material. Calculation of the saturation stress for a material is complex and depends on numerous factors such as loading conditions and temperature [59]. Accurate calculation is outside of the scope of this study.

The endurance limit of a material, as determined by conventional stress cycling tests, may be taken as a reasonable approximation of the saturation stress [60]. With the endurance limit commonly estimated as being equal to half of the material's ultimate tensile strength [61], the value for the saturation stress was therefore taken to be equal to:

$$\sigma_\epsilon^s = 0.5\sigma_u \tag{4}$$

3.3.4.3.3. *Stage four work hardening rate c_4*

The stage four work hardening rate, c_4, is given by the slope of the stress-strain curve at high strains and is generally of the order:

$$c_4 = \frac{E}{100} \tag{5}$$

where E is the Young's modulus [56].

3.3.5. Details of the material model

3.3.5.1. Specifications of the chosen material

Properties used to define the material model were determined by considering a range of real-world low carbon steel material specifications. The intent being to find a material specification

© University of Pretoria

that, when subjected to the simulated wire drawing process, would result in a yield strength as close as possible to that of the sample fibres acquired for this study.

Properties used to define the material in the simulation software are given in Table 3-1 [62]. Preliminary simulated tensile tests of the simulated drawn wire returned a yield strength of 1080 MPa, which we consider sufficiently consistent with the real-world sample which averaged out at 1200 MPa.

Table 3-1 Properties Defining the Chosen Wire Material

Density	7858 kg/m^3
Young's modulus	200 GPa
Yield strength	355 MPa
Poisson's ratio	0.3
Bulk modulus and shear modulus derived from Young's modulus and Poisson's ratio	
Hardening rule	Isotropic

It is acknowledged that the resultant yield strength of the wire produced using this material model is not as close to that of the sample fibres as could have been achieved through experimentation with the individual material parameters given by equations (3) through (5). This model is however the closest achievable approximation for a real-world material whose material parameters are calculated using equations found in literature.

3.3.5.2. Determining the stress-plastic strain curve

The relevant material properties from the chosen material specification were used to derive the requisite parameters per the equations in Section 3.3.4.3. The strain-hardening curve for implementation in the simulation was generated by numerically integrating the evolution equations in (2) using the forward Euler method. A zero initial condition was used for σ_4 and a small, non-zero initial condition was used for σ_ϵ $[58]$. The resulting stress-plastic strain curve is shown in Figure 3-6.

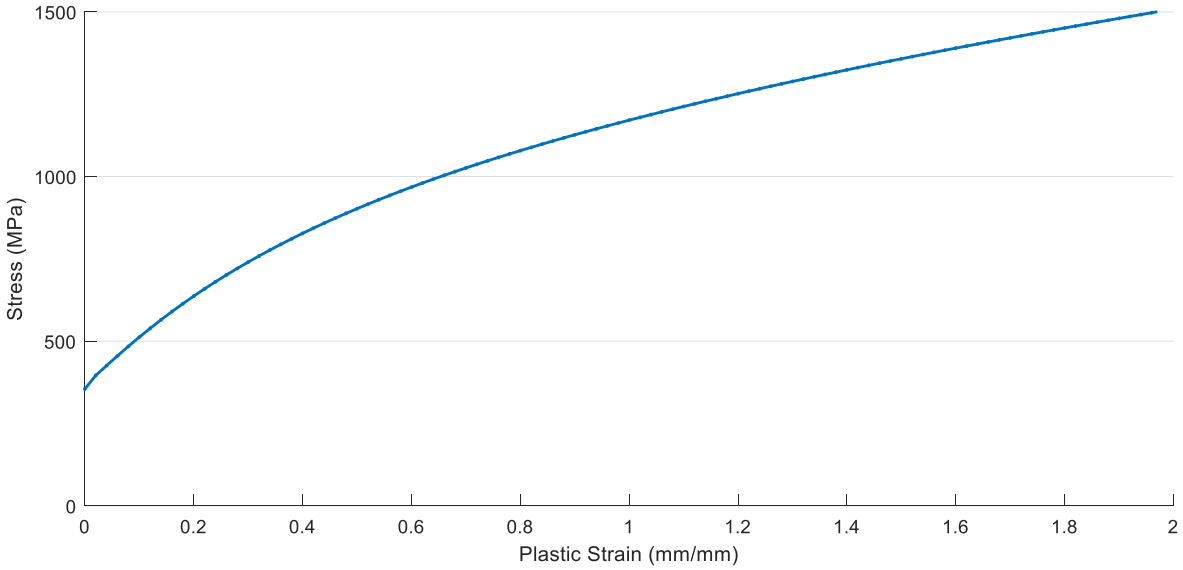

Figure 3-6 Stress-plastic strain curve for the chosen material model

3.4. CONSIDERATIONS ARISING FROM THE REAL-WORLD DRAWING PROCESS

3.4.1. Scope of the simulation

The wire drawing process is not the only fabrication process to which a given length of wire is subjected. The schematic given in Figure 3-7 presents the major steps involved in transforming stock material into hooked-end steel fibres.

© University of Pretoria

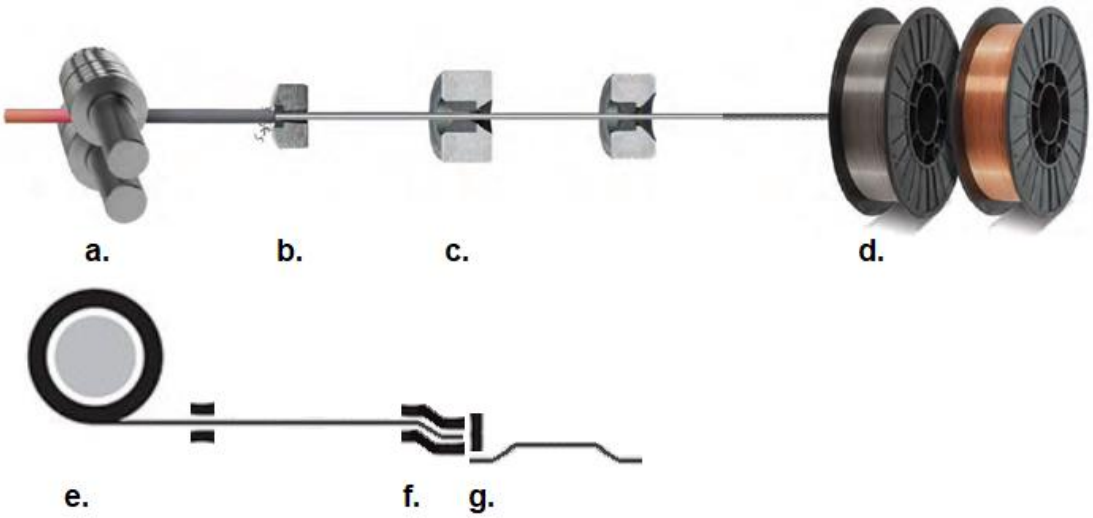

Figure 3-7 Manufacturing process for hooked-end steel reinforcing fibres

The scope of the simulation is considered with respect to Figure 3-7:

a) *Hot forming* requires high temperatures and strain rates that compensate for strain hardening through recovery processes [12]. The production of redraw rod may be neglected based on the assumption that the material is fully recovered and exists in its virgin state.
b) *Surface preparation* describes the collection of cold working operations performed in tandem with the drawing operation [14]. Removal of surface oxides through pickling will not alter the original properties of the workpiece. The effect of shaving is also assumed to be negligible. Other operations such as cleaning and lubricant application are omitted on a similar basis.
c) *Capstans and tensioners* are not explicitly depicted in Figure 3-7 but are located between the dies illustrated by c). These intermediate operations were omitted from the simulation on the basis that associated strains are many orders of magnitude less that the strains attributed to the wire drawing process and are therefore assumed to be negligible.
d) *Coiling* results in the development of cast and pitch in the final product and may affect the residual stress profiles of the wire with residual stress no longer solely a function of radial location within the wire [14]. The effect of coiling is neglected on a similar basis to c) above.
e) *Uncoiling and straightening.* Uncoiling has a converse though not necessarily equal effect to coiling. Straightening is known to alter the residual stress profiles [14] but its effect and that of uncoiling are assumed to be negligible on a similar basis to c) above.
f) *Forming of the hooked ends* is not relevant to wire drawing and will be addressed in Chapter 4.
g) Cutting is not relevant to our study but is shown for completeness. It has no effect on any material properties and will be omitted entirely.

3.4.2. Workpiece

The starting geometry for the workpiece was a wire with a diameter of 1.2mm and a length of 5mm.These dimensions were settled on because of limitations in our student version of ANSYS. No material consequences arising from these limitations could be identified.

A two-dimensional axisymmetric model was used for the workpiece. See Figure A-3 in Appendix A for dimensions of the workpiece and dies used in the simulation.

3.4.3. Boundary conditions

The simulation employed a prescribed displacement boundary condition on the leading edge of the workpiece. This boundary condition simplifies the model and is in accordance with general recommendations for non-linear simulation involving significant plasticity [63].

Frictional contact was specified between the workpiece and the approach angle, blending region and bearing length of each die. A coefficient of friction equal to 0.1 was used. See Section 3.5.3 for detail.

© University of Pretoria

3.4.4. Final diameter and percentage reduction

The hooked-end steel reinforcing fibre samples acquired for this study were measured and found to have a diameter of 0.8 mm. This was selected as the final diameter to be obtained in the wire drawing simulation.

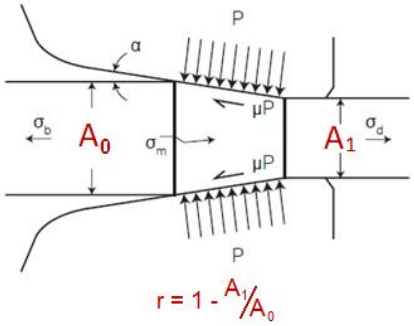

Figure 3-8 Process variables associated with final diameter and percentage reduction [50]

The reduction value r is calculated according to the equation depicted in Figure 3-8 where A_0 and A_1 are the initial and final areas respectively. This simulation will consider typical reduction values of 30 to 35% as encountered in industry [14].

3.4.5. Die properties

3.4.5.1. Material

Tungsten Carbide is a popular material for wire drawing dies [50] and is available as a standard material in the ANSYS material database. Material properties for tungsten carbide as used in the simulation are given in Table 3-2 [64].

Table 3-2 Properties Defining the Tungsten Carbide Material Model

Density	15600 kg/m^3
Young's modulus	634 GPa
Yield strength	445 MPa
Poisson's ratio	0.21
Bulk modulus and shear modulus derived from Young's modulus and Poisson's ratio	

3.4.5.2. Geometry

This study is only concerned with the nib portion of the die. Dies were dimensioned according to the recommended reduction angle of 14° for low carbon steel [50]. The DIN standard nib configuration was chosen for its ease in modelling.

3.4.5.2.1. Pass schedule

The pass schedule was designed such that the reduction angle was kept constant throughout all dies. The reduction angle of 14° (half-die angle of 7°) was rigidly enforced and the percentage area reduction value of 30 to 35% was only loosely enforced. The length of the approach angle, i.e. distance between initial and final diameters, was determined using the half-die angle and the chosen final diameter of the wire. Dimensions are given in Table 3-3.

Table 3-3 Two-Pass Die Simulation

DIE #	INITIAL DIAMETER (mm)	FINAL DIAMETER (mm)	APPROACH ANGLE LENGTH (mm)	ACTUAL % REDUCTION IN AREA	r = 1-(A_1/A_0)
1	1.2	1.0	0.81	30.6	0.306
2	1.0	0.8	0.81	36	0.36

© University of Pretoria

3.4.5.2.2. Delta ratio

The most important aspect of the die geometry is that which characterises the deformation zone. The Δ ratio is defined by [14]:

$$\Delta = \frac{average\ height\ of\ zone\ perpendicular\ to\ drawing\ axis}{length\ of\ zone\ parallel\ to\ drawing\ axis} \quad (6)$$

The assumption of a trapezoidal deformation zone is a common approximation used in industry and leads to [14]:

$$\Delta \approx \frac{4\tan\alpha}{\ln\frac{1}{(1-r)}} \quad (7)$$

For α = 0.122 radians (7°) and r obtained from Table 3-3, delta ratios for the two-pass simulation are given in Table 3-4. A value of Δ close to 1.0 is desirable and can be shown to result in minimum die pressures [14].

Table 3-4 Δ Ratios Arising from the Two-Pass Simulation

PASS NUMBER	α (radians)	r	Δ
1	0.122	0.306	1.35
2	0.122	0.36	1.1

3.4.5.2.3. Bearing length

The main objective of the bearing length is to maintain the output diameter while the die is subjected to wear. Commercial dies with minimal bearing length do exist, as well as those with a bearing length of up to 200% of the wire diameter [14]. A fixed bearing length of 1.7mm was used in this simulation, this being 142% of our input diameter, 170% of our first stage output diameter and 213% of our final diameter.

The main objection to a large bearing length is the increased friction and concomitant increased drawing stresses. There is however no evidence in practice to disqualify the bearing lengths such as we have here [14].

3.4.5.2.4. Blending

The transition between the approach angle and the bearing length is critical to surface finish of the as-drawn wire and is implemented as a radius [14]. The extent of blending is not expected to influence the residual stress profile since the blend acts to effectively reduce the length of the deformation zone. Only magnitude will be affected. A modest blend radius of 0.5 mm was applied to the CAD model in order to prevent unwanted stress concentrations and aberrant behaviour associated with the switching of contact boundary conditions between surfaces.

3.4.5.3. CAD model

A two-dimensional axisymmetric model of only the nib interior was modelled since it is the only part of the die that is in contact with the workpiece and as such renders any other parts of the die superfluous to this study. The bearing and small portions of the bell and back relief were included for the sake of appearance. See Figure A-1 and Figure A-2 in Appendix A for dimensions of the dies.

3.4.5.4. Number of passes

Wire drawing machines are modular and individual die blocks may be assembled in series to make a continuous line of up to 12 drawing passes [13]. The wire drawing simulation considered in this study employed a two-pass wire drawing process.

© University of Pretoria

3.4.6. Extraction of results

Results from the simulation are noted at the conclusion of the wire drawing process when the whole workpiece has passed through both dies and there is no longer any imposed loading. Conditions prevailing at the leading and trailing ends of the processed workpiece are discarded as they are not representative of the material we are interested in.

Stress results were therefore extracted from a region midway along the sample. We note that the reported stress profile towards the centre is not completely uniform and that variations about a mean occur throughout. For the final set of results, the stresses and strains were averaged across the middle 6.75 mm length of the wire at each node in the radius, discarding results from a length of 2.25 mm at either end.

3.5. EFFECT OF WIRE DRAWING PROCESS VARIABLES

This section lists and discusses the observable effects of the wire-drawing process that have been identified through simulation and how they in turn affect the residual stress profiles of the drawn wire. Expected features of the residual stress profiles were identified from the simulations in literature given in Section 3.2.

Residual stress magnitudes cannot be verified in the absence of experimental results. Process variables that can be shown to affect only the relative magnitudes of the residual stresses were therefore not studied in detail. The relevance of the residual stress profiles will be investigated in Section 4.8 and it is anticipated that, should the magnitude be relevant, it may be estimated by solving the inverse problem for a known profile as in Chapter 5.

Since residual stresses exist as a result of a non-uniform distribution of plastic strain, it is reasonable to assume that any variable that affects the residual stress profile will also affect the yield strength profile. The effect of a particular variable on the yield strength profile is therefore implied and will not be explicitly discussed.

For purposes of this study, the interdependence of factors such as temperature and friction were not investigated in detail beyond acknowledging their existence. Detailed consideration was given to the factors highlighted in Figure 3-9.

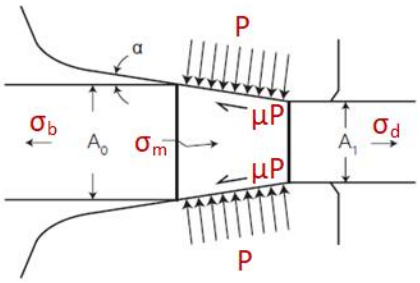

Figure 3-9 Factors relevant to the simulation of wire drawing [50]

3.5.1. Back tension

Back tension, σ_b, improves alignment between the workpiece and die thereby extending the life of the die [14] and improving tolerances on final dimensions [15]. Its application is optional [14] due to the fact that it can result in deterioration of mechanical properties [65]. Back tension was neither considered in the simulations reviewed in Section 3.2, nor in our simulation.

3.5.2. Centreline stresses and redundant work

The chosen die geometries result in compressive centreline stresses, σ_m, through the wire and will not give rise to bulging [14]. The nature of the simulation is such that the centreline stresses and any redundant work will be accounted for.

© University of Pretoria

3.5.3. Friction

Average frictional stress, μP, is highlighted in Figure 3-9. The following modes of friction were considered [14]:

a) *Frictionless* is known to be unrealistic and is therefore not a candidate mode of friction. Comparison of the results from other modes with the frictionless profile does however facilitate direct observation of the effect of the coefficient of friction on the residual stress profiles.
b) *Sticking friction mode* models conditions of no lubricant and therefore has the highest coefficient of friction value, 0.25. This mode generates heavy striations and cracks on the wire surface.
c) *Local sticking mode* has marginal lubrication and a coefficient of friction of 0.15. The drawn wire is characterised by chevron or "crow's feet" like surface defects.
d) *Boundary lubrication mode* requires the thinnest possible film of lubricant and has a coefficient of friction of 0.1. The wire surface is smooth and bright due to the flattening of surface defects.
e) *Thick film lubrication mode* exists when the lubricant film is sufficiently thick so as to promote conditions of shear stress between the wire and die. The coefficient of friction is 0.05 and the drawn wire is characterised by a lumpy and matte surface finish.

Practical values for the coefficient of friction may be expected to vary from 0.01 to 0.2 [17]. We therefore select a coefficient of friction equal to 0.1 as this is representative of a wire drawing process that produces the desired surface finish. Figure 3-10 compares the residual stress profile obtained using $\mu = 0.1$ with that of the frictionless model, demonstrating the fact that the coefficient of friction does not affect the profile and only affects the relative magnitudes of the stresses.

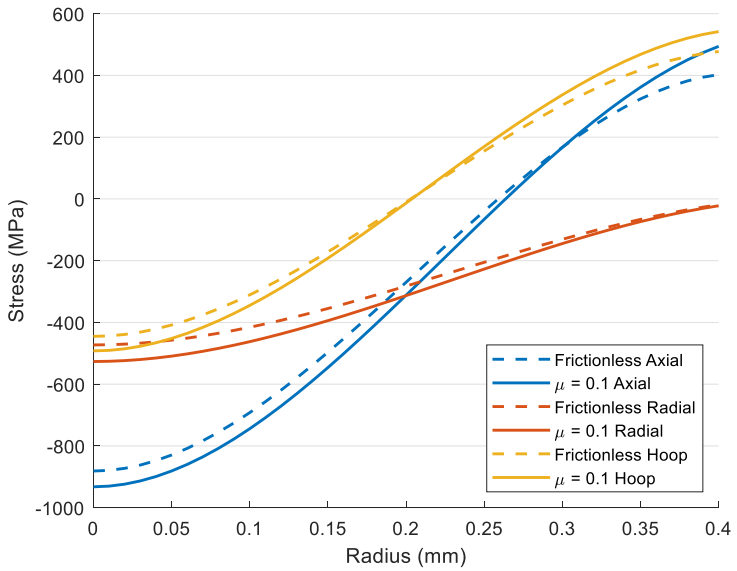

Figure 3-10 Effect of μ on residual stress profiles

3.5.4. Factors associated with drawing stress

The effects associated with the drawing stress, σ_d, highlighted in Figure 3-9, are those associated with the action of pulling the wire through the die. They include increased temperature and drawing speed.

3.5.4.1. Temperature and its effect on residual stress

For temperatures below those required for recrystallisation, up to 95% of the work associated with friction and deformation results in heat increase [15]. The change in temperature of the core and surface of the wire is plotted as a function of axial position in the wire drawing process in Figure 3-11.

© University of Pretoria

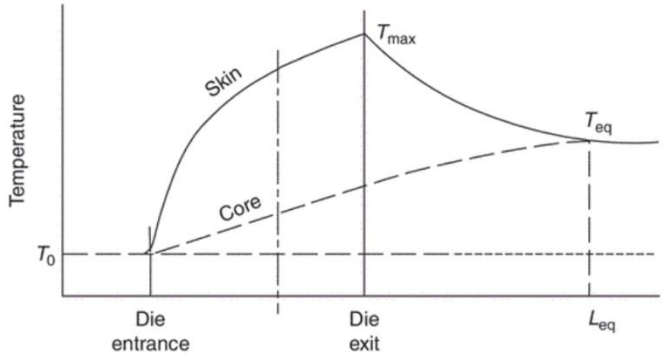

Figure 3-11 Change in core and surface temperature along wire axis relative to die [14]

Figure 3-11 shows the temperature gradient existing in the wire as it exits the die and the equalisation of temperature a certain distance, L_{eq}, from the die exit. At this point there is no longer a temperature gradient and the resulting temperature may be estimated by:

$$T_{eq} \approx T_0 + \frac{\sigma_d}{C\rho} \tag{8}$$

where T_0 is the temperature of the wire just before it enters the die, C is the material specific heat and ρ is the material density [14].

The cooling and contraction of the surface and heating and lengthening of the centre of the wire during the equilibration process is expected to create residual stresses [14] with the profiles being affected by the magnitude of the temperature increase in the die and the temperature gradient in the wire as it exits the die.

3.5.4.1.1. Estimation of temperature increase

Even though friction is known to contribute to temperature increase, for simplicity, it was omitted from this investigation on the assumption that its effect may be studied independently. The temperature increase per pass was calculated using equation (8) with results given in Table 3-5. The drawing stress was obtained from the frictionless wire drawing simulation with material properties given by Wright [14].

Table 3-5 Temperature Increase by Pass

PASS #	DRAWING STRESS σ_d (MPa)	SPECIFIC HEAT (J/(g°C))	DENSITY (g/cm^3)	TEMPERATURE INCREASE (°C)
1	237.62	0.486	7.85	62.3
2	457.97	0.486	7.85	120.0

The equilibrated temperature of the wire is therefore calculated by adding the temperature of the wire just before it enters the die to the results given in Table 3-5. A number of opportunities are known to exist for the dissipation of heat between passes [14] and some authors are known to exploit this by stating that temperatures will therefore not exceed $250\ ℃$ in any given pass [17]. Assuming an initial temperature of $T_0 = 25\ ℃$ between passes, a final equilibrated temperature of $T_{eq} = 145\ ℃$ is predicted.

3.5.4.1.2. Recovery and recrystallisation

Recovery and recrystallisation are expected to have an effect on the residual stress profiles due to the associated decrease in strength and increase in ductility [15]. Internal strain energy is relieved during recovery and recrystallisation involves the growth of new grains without internal strains [52]. Since the temperatures at which

© University of Pretoria

recovery and recrystallisation occur are not explicitly published properties of the material, reasonable estimates were made.

The lower bound for the recrystallisation temperature is commonly approximated as a third of the material melting temperature in degrees Celsius [52]. For a solidus temperature of 1766 K for carbon steel [14], the recrystallisation temperature is therefore approximately equal to 771.15 K.

Recovery is known to occur at lower temperatures than recrystallisation [15]. The lowest possible temperature for recovery was estimated using pressure-vessel industry guidelines for material properties that do not change with time. The recovery temperature for cold drawn low-carbon steel was therefore estimated to be equal to 343 °C [66].

Since the final equilibrated temperature of our wire drawing process is lower than the temperature values given above, recovery and recrystallisation are not anticipated to occur and their effects may therefore be ignored in this study.

3.5.4.1.3. Static strain ageing

Static strain ageing results in increased yield strength due to the migration of carbon and nitrogen atoms to the strain fields of dislocations [14]. It does not affect residual stress profiles since there is no relaxation of internal stress states.

It may however affect the yield strength profile through the wire. While this may be an interesting topic for further study, it would bring an extra dimension to our study, viz the effect of time. The effect of static strain ageing on the yield strength profile is therefore not considered in this simulation.

3.5.4.1.4. Dynamic strain aging

Dynamic strain aging requires plastic deformation at increased temperatures and results in a product with a higher strength than anticipated at the end of the drawing process [14]. Dynamic strain ageing therefore does not affect the residual stress profiles.

The specific temperature at which dynamic strain aging has its largest effect is dependent on the strain rate. Typical wire drawing process have strain rates of 10^3 to 10^4 s^{-1} which corresponds to a required temperature range of 500-650 °C [14]. Although it is possible that the surface temperature of the wire could reach such high temperatures, we saw that the average temperature of the wire at the end of the final pass in the simulation is well below the practical temperature range for dynamic strain aging. Since dynamic strain aging may be expected to only affect the surface of the wire, it is reasonable to assume that on average, the yield strength profile of the wire will remain unaffected by dynamic strain ageing.

3.5.4.1.5. Temperature gradient

From Figure 3-11 we see that the workpiece will exit the die with a temperature gradient, the surface being at a much higher temperature than the centre. The figure also shows that this gradient equilibrates over a distance of L_{eq} to a temperature value, T_{eq}. The effect of the temperature gradient on the residual stress profiles was investigated by simulation using the frictionless wire drawing process.

No equation could be found to estimate the temperature of the surface of the wire as it exits the die, T_{max}. A value for T_{max} was therefore estimated by performing a basic transient thermal simulation on a 0.8 mm diameter wire under conditions of convection in stagnant air with ambient temperature equal to 25 °C.

© University of Pretoria

The temperature profile at the die exit in Figure 3-11 indicates that the core temperature is approximately 0.3 times the temperature at the surface. Assuming an exponential temperature profile through the wire and given the equilibrated temperature $T_{eq} = 145\,℃$, the transient thermal analysis returned $T_{max} = 208.56\,℃$ and $T_{core} = 64.20\,℃$. This defined the initial temperature profile at the die exit.

Residual stress profiles were determined by applying this initial temperature profile as a thermal condition in the frictionless wire drawing simulation. The effect of the temperature gradient on the residual stress profiles at the die exit is illustrated in Figure 3-12. The set of dashed curves represents the baseline returned by a simulation excluding the effect of the temperature gradient.

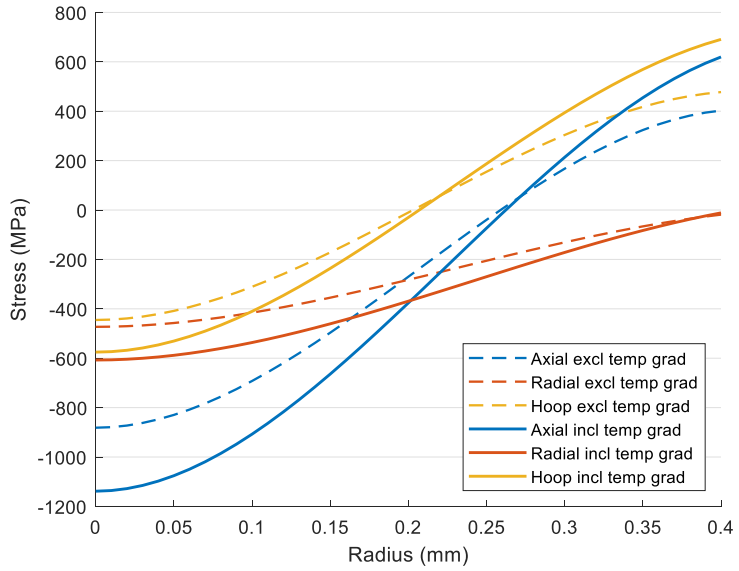

Figure 3-12 Effect of temperature gradient at die exit on residual stress profiles

We see that, while the temperature gradient exists, the resulting residual stress profiles are similar in shape and vary in magnitude only. A second simulation was run where the wire was allowed to cool to room temperature. The subsequent change in residual stresses due to the disappearance of the temperature gradient is given in Figure 3-13.

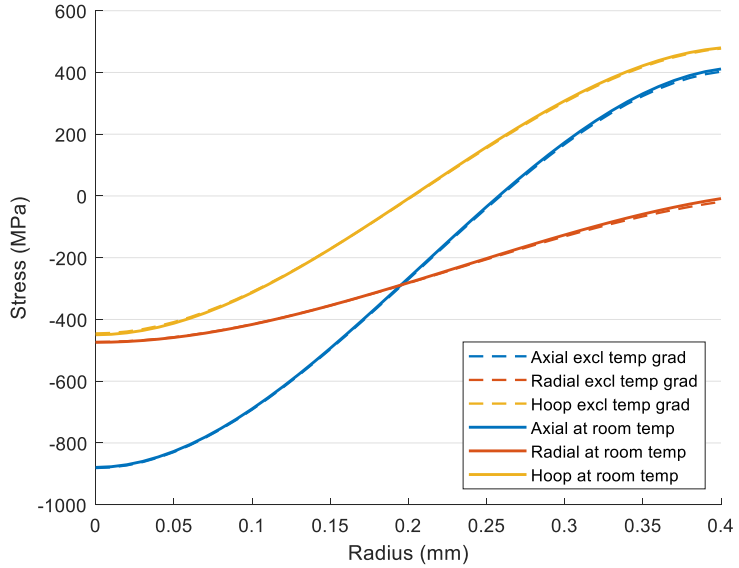

Figure 3-13 Effect of temperature gradient on residual stress profiles after cooling

© University of Pretoria

Figure 3-13 shows that the residual stresses in the cooled wire are almost identical to the residual stresses determined without consideration of the temperature gradient. It is therefore concluded that, while the temperature gradient is present higher residual stresses exist, and when the wire has reached room temperature the temperature gradient ceases to have an effect. The temperature gradient at the die exit will therefore not be included in the final simulation.

3.5.4.1.6. Effect of friction-related temperature

The temperature increase due to friction is proportional to the temperature increase associated with the deformation of the wire. The relationship is given by:

$$T_f = \mu \cot \alpha T_w \tag{9}$$

where T_w is the temperature increase due to both uniform deformation and redundant work [14]. From equation (9) it is evident that a high coefficient of friction results in a greater temperature increase across the die.

Since it has been shown that the temperature gradient present in the wire at the die exit does not affect the residual stress profiles, and since friction has been shown to contribute to the temperature gradient, the effect of the temperature increase associated with friction may be considered to be additive and to only affect the relative magnitudes of the residual stresses while the temperature gradient exists. We conclude that the residual stress profiles may be determined without including accurate simulation of thermal conditions related to friction.

3.5.4.2. The relationship between strain rate and temperature

The flow curve for a material cannot be defined by the relationship between stress and strain alone and must consider strain rate and temperature [12] [15]. Separately, increased temperature results in decreased Young's modulus, yield strength and tangent modulus [67] and increased strain rate results in increased yield strength, with a large increase in strain rate only resulting in a relatively small increase in flow stress [12]. Together, sensitivity of the flow stress to strain rate increases with increasing temperature [16].

In their simulation of a wire drawing process, Phelippeau et al. [47] concluded that increased strain rate competes with and therefore compensates for the effect of increased temperature in the development of residual stresses. Counterintuitively, a material model with a lower flow stress was therefore used for the simulation of the drawing process and a higher flow stress for the simulation of the tensile test. The flow stress for drawing was determined by comparing the results of subsequent simulated tensile tests at a known flow stress with experimental tensile test results.

In their study on the effect of strain rate, He et al. [68] noted no flow stress temperature dependence for temperatures of up to190 °C. Since our simulation considers a maximum temperature of 145 °C as established in Section 3.5.4.1.1. we will therefore also consider the flow stress to be independent of temperature.

The effect of strain rate was studied by comparing simulation results obtained using quasi-static flow curves with those obtained using dynamic flow curves determined at a strain rate of 2000 s^{-1} from Split Hopkinson Pressure Bar (SHPB) tests. Figure 3-14 shows that when the effect of strain rate is accounted for, material yield stress increases resulting in an increase in the magnitudes of the residual stresses [68].

© University of Pretoria

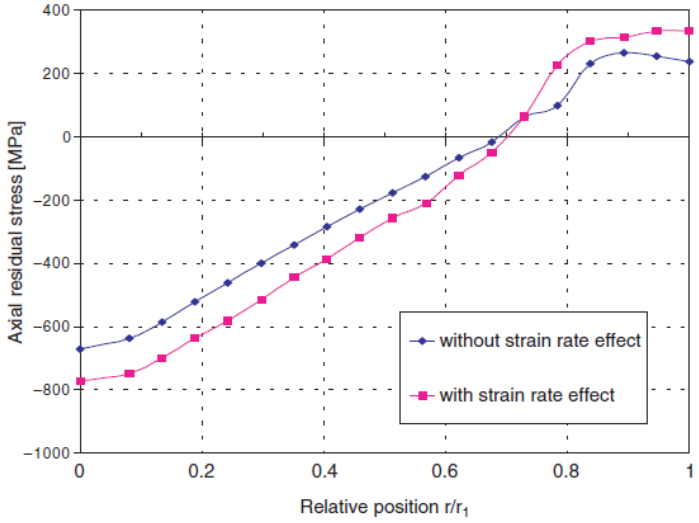

Figure 3-14 Effect of strain rate on axial residual stress profile [68]

It is evident from Figure 3-14 that consideration of the strain rate does not affect the residual stress profile. Additionally, the influence of strain rate has been shown to diminish with increasing strain in low carbon steels [68]. We therefore conclude that the effect of strain rate on flow stress may be neglected in our simulation.

3.5.5. Factors associated with material model

The effect of the material model on the residual stress profiles was investigated by increasing the values for the parameters used to define the model by 20% as given in Table 3-6. Four simulations were run with one parameter changed at a time. Comparison of the resulting residual stress profiles with the baseline profiles is given in Figure 3-15.

Table 3-6 Investigation into Effect of Parameters Defining Material Model

PARAMETER	ORIGINAL VALUE	ADJUSTED VALUE
Yield strength, σ^y	355 MPa	426 MPa
Initial work hardening rate, θ_0	800 MPa	960 MPa
Saturation stress, σ_ϵ^s	280 MPa	336 MPa
Stage IV work hardening rate, c_4	2000 MPa	2400 MPa

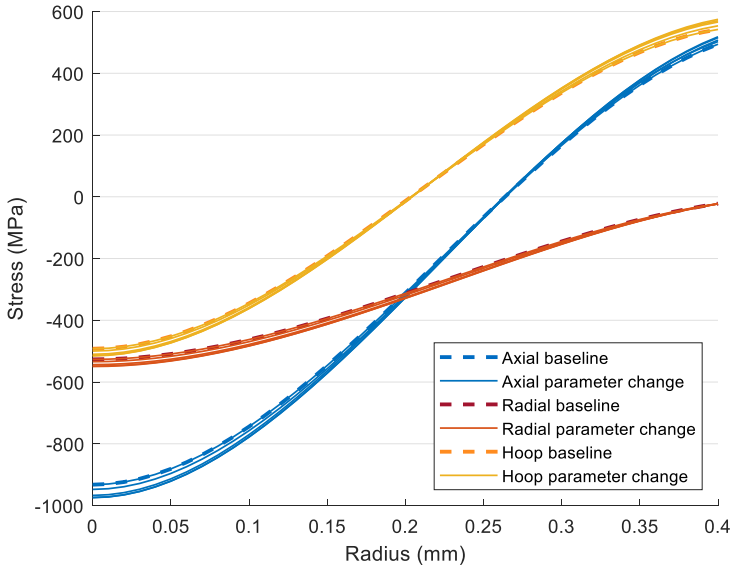

Figure 3-15 Effect of material model parameters on residual stress profiles

© University of Pretoria

It is evident from Figure 3-15 that the parameters used to define the material model do not affect the residual stress profiles. Only the magnitudes of the stresses are seen to change.

3.6. WIRE DRAWING SIMULATION

3.6.1. *Meshing on workpiece*

The workpiece is known to increase in length and decrease in diameter during the wire drawing process resulting in mesh distortion. The mesh was therefore graded appropriately to avoid deterioration in element quality during the solution [53].

3.6.2. *Convergence study*

A convergence study determined that mesh refinement had an effect on the residual stress profiles through the wire. Convergence was considered to have been obtained once subsequent mesh refinement no longer affected the shape of the residual stress curves and only affected the magnitudes of the stresses. Mesh sizes used in this aspect of the study are given in Table 3-7. The fine mesh size was found to be a reasonable compromise between the need for computing economy and accuracy in identifying the axial, radial and hoop residual stress profiles.

Table 3-7 Mesh Refinements for the Convergence Study

CONSIDERATION	COARSE	MEDIUM	FINE	FINER	FINEST
Divisions across radius	3	6	20	30	40
Element height	0.267 mm	0.133 mm	0.04 mm	0.0267 mm	0.02 mm
Divisions across length	100	250	380	250	193
Element width	0.05 mm	0.02 mm	0.013 mm	0.012 mm	0.0104 mm
Workpiece length	5 mm	5 mm	5 mm	3 mm	2 mm

Workpiece length is not a critical variable since residual stress profiles are not a function of axial position along the wire, provided the position under consideration is sufficiently far from the ends of the wire. Since the residual stresses are affected by radial location only, the most critical dimension in terms of convergence is the element height. Mesh refinement attempted to halve element height, where practical, while maintaining the element aspect ratio.

Figure 3-16 through Figure 3-18 show the effect of mesh refinement on the axial, radial and hoop residual stress profiles respectively. Further refinement beyond that of the fine mesh was found to substantially increase simulation time with no significant change to the shape of the residual stress profiles.

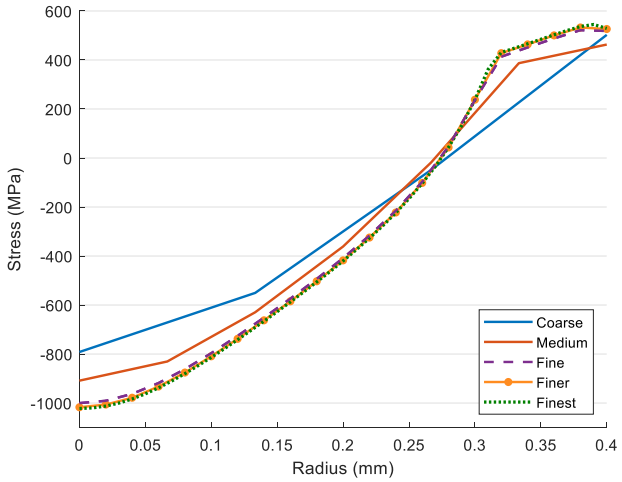

Figure 3-16 Effect of mesh refinement on axial residual stress profile

© University of Pretoria

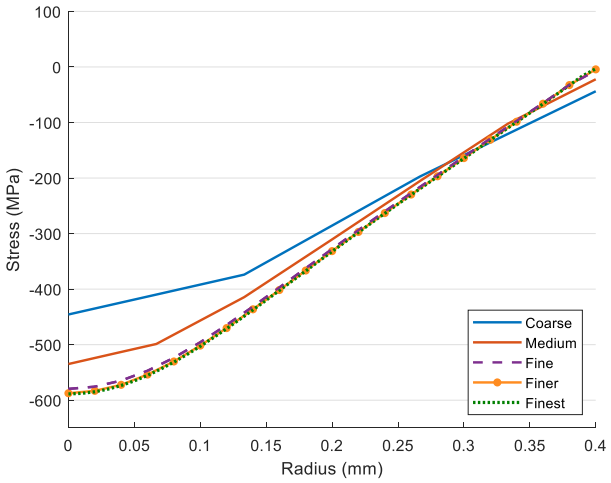

Figure 3-17 Effect of mesh refinement on radial residual stress profile

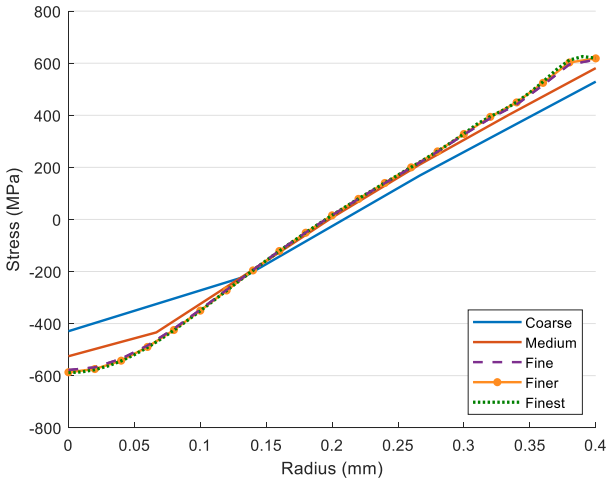

Figure 3-18 Effect of mesh refinement on hoop residual stress profile

3.7. RESULTS

Residual stress profiles obtained from the final simulation are given in Figure 3-19 and Figure 3-20 shows the normalised profiles from literature together with the normalised results of the final simulation. Comparison between the final results and those from literature is seen to be favourable.

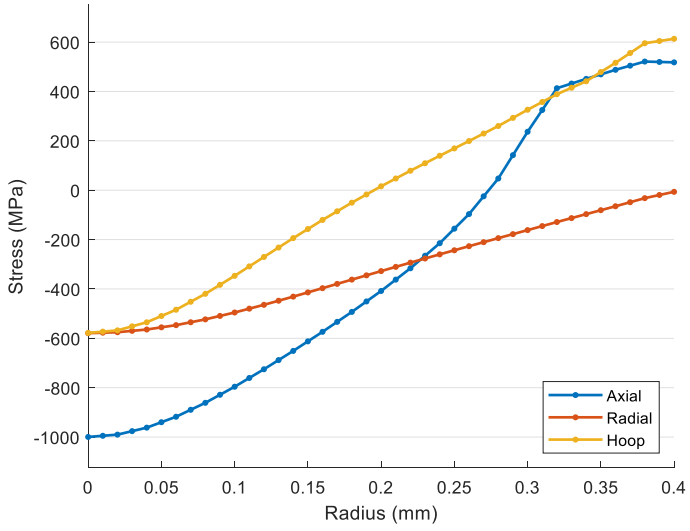

Figure 3-19 Residual stresses in the simulated as-drawn wire

© University of Pretoria

The normalised profiles in Figure 3-20 have the domain 0 to 1. Since the simulations in literature made use of wires of a different diameter to our simulations, the x-axis (radius) was normalised by dividing the radius value at each point along the radius by the magnitude of the radius. A similar approach was applied to normalisation of the y-axis (stress) where the stress value at each point was divided by the maximum absolute stress value for the range of axial, radial or hoop stresses considered.

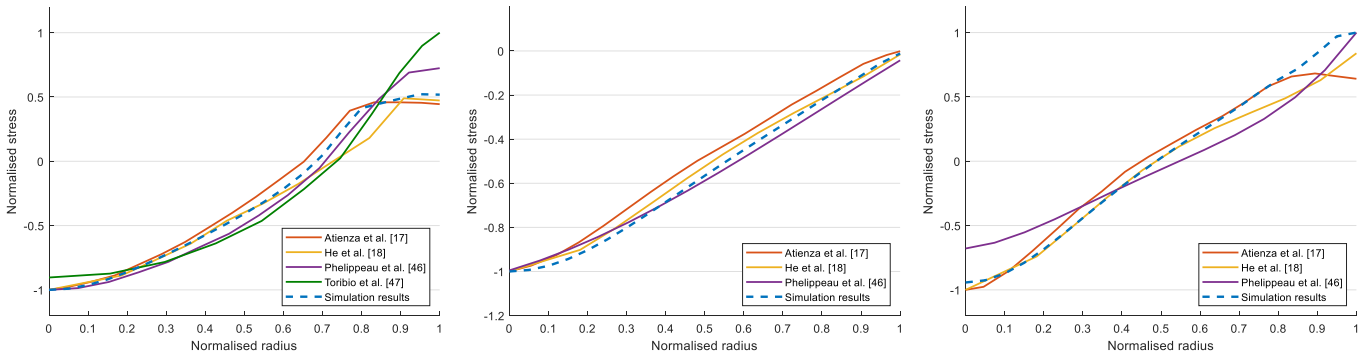

Figure 3-20 Comparison of normalised simulation result with profiles from literature

Equivalent plastic strain was used as the state variable in this simulation. It is acknowledged that equivalent plastic strain should not typically be used as a state variable since plasticity is path dependant. However, in this simulation, the direction of the plastic deformation is constant and the flow stress as a function of the radius of the workpiece may therefore be determined using the stress-plastic strain curve for the material. Equivalent plastic strains as a function of workpiece radius are given in Figure 3-21.

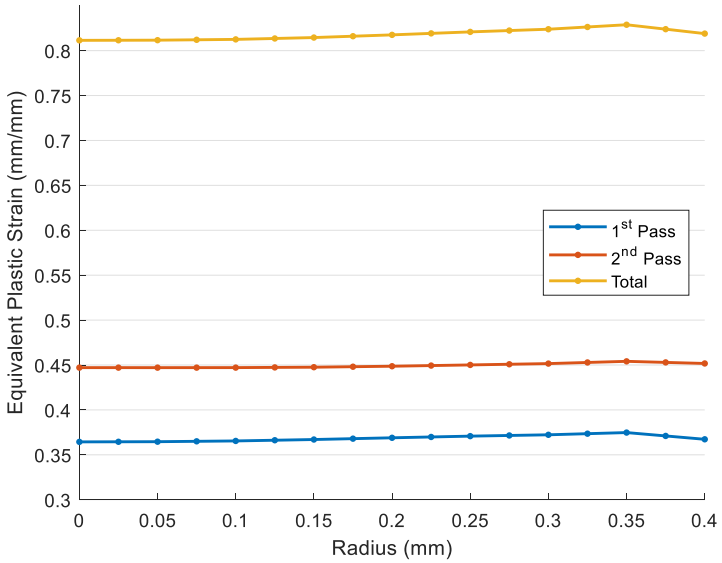

Figure 3-21 Final and individual pass equivalent plastic strain profiles

In Figure 3-21 the final equivalent plastic strain profile is given as well as the individual profiles due to each pass. See Figure A-5 to Figure A-7 in Appendix A for the individual profiles. The equivalent plastic strain profile compares favourably with the profile given by Toribio et al. [48] in Figure 3-22.

© University of Pretoria

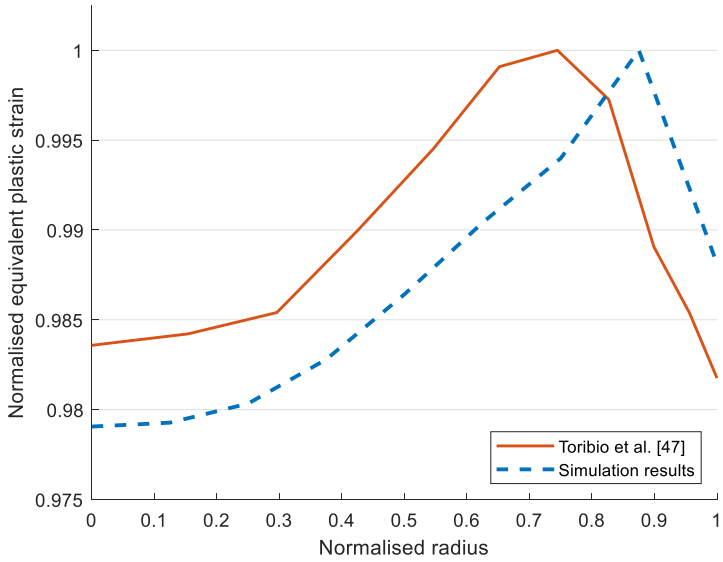

Figure 3-22 Comparison of normalised simulation result with profile from literature

3.8. SUMMARY

To identify an appropriate material model, we started off with a sample of a steel hooked-end fibre which we had analysed by a competent laboratory to determine its mechanical characteristics. The constitutive equation for work hardening was given by the Stage IV Voce hardening model, known to be accurate at large strains. Parameters were determined using equations given in literature and real-world material properties. The chosen material model resulted in a simulated yield strength as close in value to that of the samples as could be achieved using real-world material specifications.

A real-world wire drawing process was examined to identify the aspects which would have a direct bearing on the setup of the final simulation model. Our scope thus limited, we moved on to a detailed investigation of those aspects not directly covered in literature in terms of their effect on the residual stress and yield strength profiles through the wire after drawing. Process variables that could be shown to affect the shape of the curves were included in the simulation.

After our investigation, we then simulated a wire-drawing process that resulted in a model that matches the dimensional characteristics of our sample wire. This output product was then assessed to determine its residual stress and yield strength profiles and we found that they compared favourably with simulations in literature.

In terms of the yield strength profile, equivalent plastic strain was shown to be an acceptable state variable since the direction of development of plastic strain is constant during wire drawing. The yield strength profile therefore takes the form of the equivalent plastic strain profile.

We are confident that we have a representative material model and process for converting it into virtual wire suitable for our next step which is to obtain baseline results by subjecting the virtual wire to a series of simulated tests. This will be followed by inverse analysis in accordance with our starting objective.

© University of Pretoria

CHAPTER 4 - SIMULATING THE PULL-OUT TEST

4.1. OVERVIEW

In order to achieve the objective of this study, we need to know:

- Which properties attributable to the wire drawing process have the greatest effect on pull-out behaviour?
- Whether this resultant effect can be used to recover detail on the properties and hence define an accurate approximate material model?
- And, how that approximate material model would perform in a simulated pull-out test?

From this point onwards, the term 'as-drawn wire' will refer to the consequence of our prior wire-drawing simulation. Results from several tests performed on the as-drawn wire represent the final state of that which we know from the simulation, which will then be used as a benchmark for solving the inverse problem. The remainder of this chapter describes our process as follows:

a) Establish the properties of the as-drawn wire in respect of:
   - Uniaxial tensile test
   - Torsion test
   - Bend test
b) Simulate forming the hooked ends on the fibre
c) Simulate a pull-out test on this hooked fibre
d) Perform sensitivity analysis to rank manufacturing factors i.t.o. effect on the pull-out curve

4.2. INITIAL STRESS AND STRAIN

The nature of the wire drawing process permitted the use of a two-dimensional axisymmetric model. This however is unsuitable for the tests performed in this section. The stress and plastic strain results from the wire drawing simulation therefore need to be transferred to subsequent simulations as initial conditions before proceeding with the tests.

It is known that the stress state of a body is completely described by means of the stress tensor [12]. Normal stresses in three directions are defined by the residual stress profiles. The magnitude of the shear stresses are of the order 10^{-2} and, relative to that of the normal stresses (of order 10^{1} to 10^{2}) were considered small enough that they were assumed to be equal to zero.

The Von Mises plasticity model accounts for all normal and shear plastic strains in one equivalent value, viz equivalent plastic strain. Since the manner in which the workpiece is strained does not change during the wire drawing process, it is concluded that in this specific case the equivalent plastic strain is a state variable. The initial strains in the workpiece were therefore defined by the equivalent plastic strain profile.

The initial state was verified by comparing the engineering stress-strain curve generated by simulating a tensile test on the deformed 2D axisymmetric model directly after drawing through the dies with that of the 3D model in Figure 4-1. The curves thus generated show a small difference. The yield strengths from both curves were calculated using the 0.2% offset, giving values of 1066.78 MPa and 1040.85 MPa for the 2D and 3D models respectively. The percentage error between the yield strength obtained from the 3D model and that of the 2D model is 2.4%.

It is noted that fair distortion existed in the mesh of the as-drawn wire at the end of the 2D axisymmetric simulation and that the stresses and strains in the model had not been processed to obtain average values sufficiently far from the ends. Given this and the small difference (2.4%) between yield strengths determined by each model, the initial state of the 3D model may be concluded to have been correctly defined.

© University of Pretoria

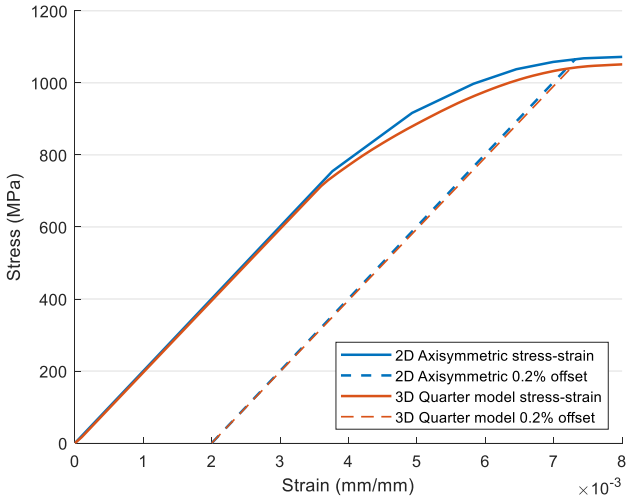

Figure 4-1 Comparison of uniaxial tensile test engineering stress-strain curves for 2D and 3D models

4.3. TENSILE TEST

A quarter model with dimensions as given in Figure 4-2 was used for the tensile test. The nature of the implicit simulation is such that necking will be observed during the test but not fracture. Boundary conditions were set up to enforce symmetry and to replicate conditions of a prescribed displacement tensile test. Convergence on the mesh was established. See Section B.1 in Appendix B for details.

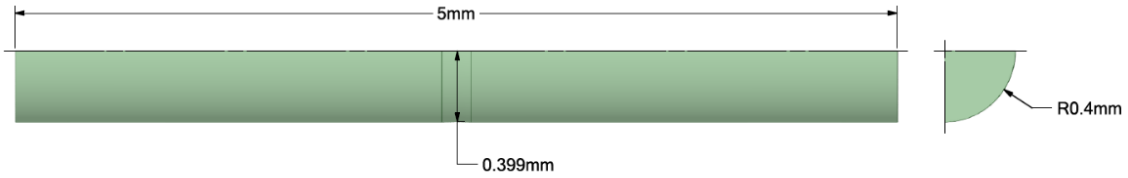

Figure 4-2 Dimensions of quarter model for the tensile test

The resulting force-displacement curve was converted into the engineering stress-strain curve depicted in Figure 4-3 in accordance with advised practice [12] and yield strength was calculated using the 0.2% strain offset. Yield strength is equal to 1040.85 MPa and ultimate tensile strength is equal to 1075.73 MPa. Necking in the specimen is shown in Figure 4-4.

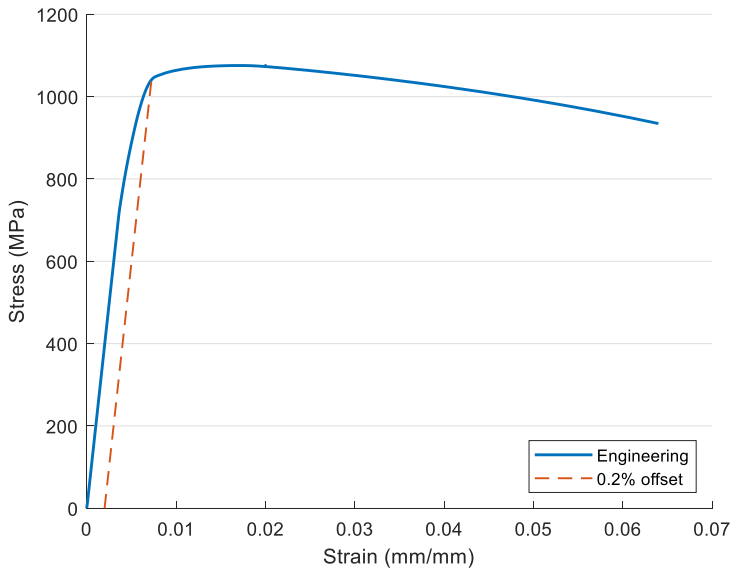

Figure 4-3 Engineering stress-strain curve, tensile test, as-drawn wire

© University of Pretoria

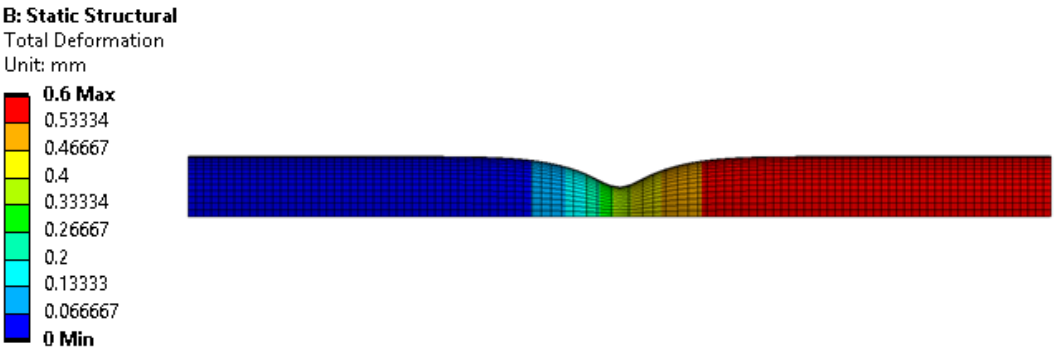

Figure 4-4 Uniaxial tensile test showing necking

4.4. TORSION TEST

A full-sized model was used for the torsion test, dimensions are as given in Figure 4-5. Boundary conditions were set up to replicate conditions of a prescribed displacement torsion test with one full rotation in one direction, followed by one full rotation in the opposite direction to return to the starting datum. Convergence on the mesh was established. See Section B.2 in Appendix B for details.

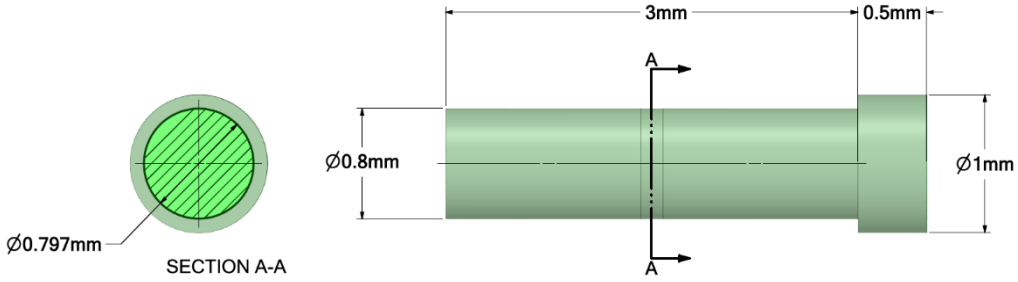

Figure 4-5 Dimensions of full model for the torsion test

The resulting torque-twist curve is depicted in Figure 4-6. The yield strength in shear was calculated using the 2° offset [69] and is equal to 757.7 MPa.

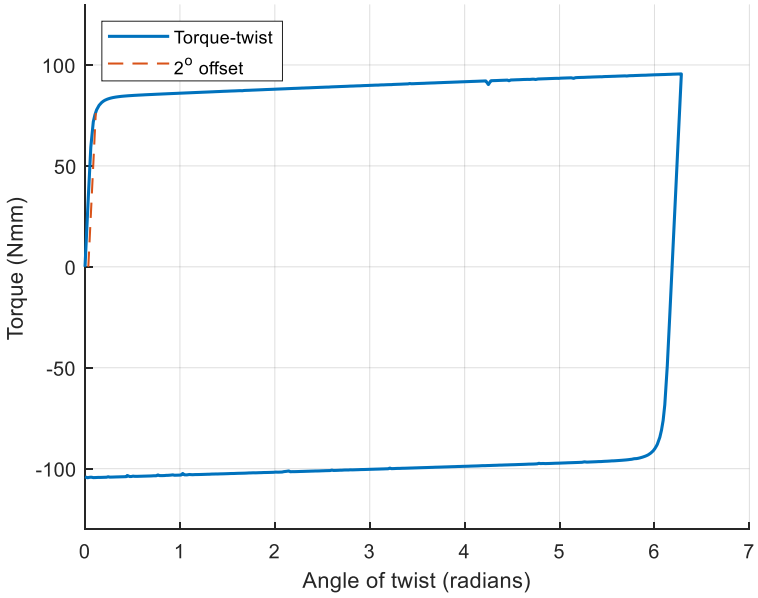

Figure 4-6 Torque-twist curve, torsion test, as-drawn wire

© University of Pretoria

4.5. BEND TEST

The nature of the bend test is such that a quarter model with two planes of symmetry is able to fully represent the sample in the real world. The fibre was therefore modelled as a half cylinder with a length equal to half that of the real-world fibre, dimensions are as given Figure 4-7.

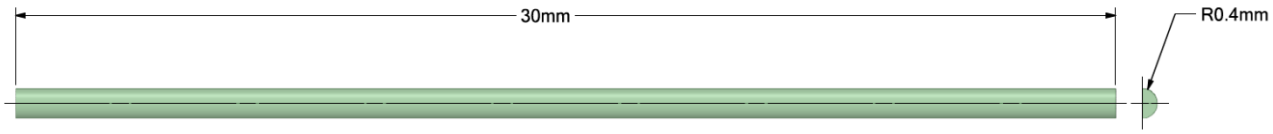

Figure 4-7 Dimensions of quarter model for the bend test

Boundary conditions were set up to enforce symmetry and to replicate the conditions of the bend test advised in literature [58]: a simple support at the centre and a prescribed displacement initially parallel to the end face as shown in Figure 4-8. Convergence on the mesh was established. See Section B.3 in Appendix B for detail.

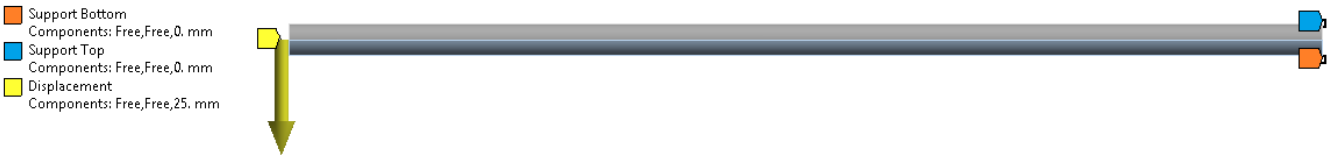

Figure 4-8 Support and loading conditions for the bend test

The sequence of displacements is depicted in Figure 4-9. Forward bending occurs with the application of a prescribed displacement of 25 mm in the z-direction ending at position a). The prescribed displacement is then removed, and the wire allowed to return to its relaxed state in position b). Reverse bending occurs with the application of a prescribed displacement to firstly return the wire to the starting position c) followed by a prescribed displacement of -25 mm in the z-direction, ending at position d). The prescribed displacement is once again removed, and the wire allowed to return to its relaxed state in position e).

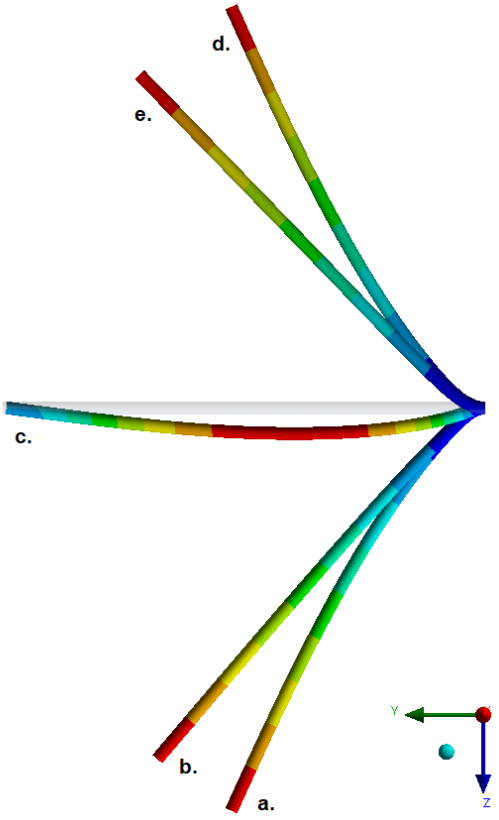

Figure 4-9 Sequence of displacements in the bend test

© University of Pretoria

The aim of the bend test is to expose the wire to the same conditions of bending and reverse bending experienced by the bend radii during the pull-out test and to thereby gain information regarding the behaviour of the material under these conditions. An angle to which the wire must be bent is therefore not specified. Instead, the requirement is a minimum accumulated equivalent plastic strain value as dictated by the hooked-end forming process.

The forming process detailed in Section 4.6 resulted in a maximum of 0.35 mm/mm equivalent plastic strain as shown in Figure 4-15. Forward bending was seen to contribute 0.275 mm/mm and reverse bending 0.175 mm/mm, totalling to 0.45 mm/mm equivalent plastic strain. Figure 4-10 shows the equivalent plastic strain attributable to bending in the forward direction and Figure 4-11 shows that attributable to subsequent bending in the reverse direction.

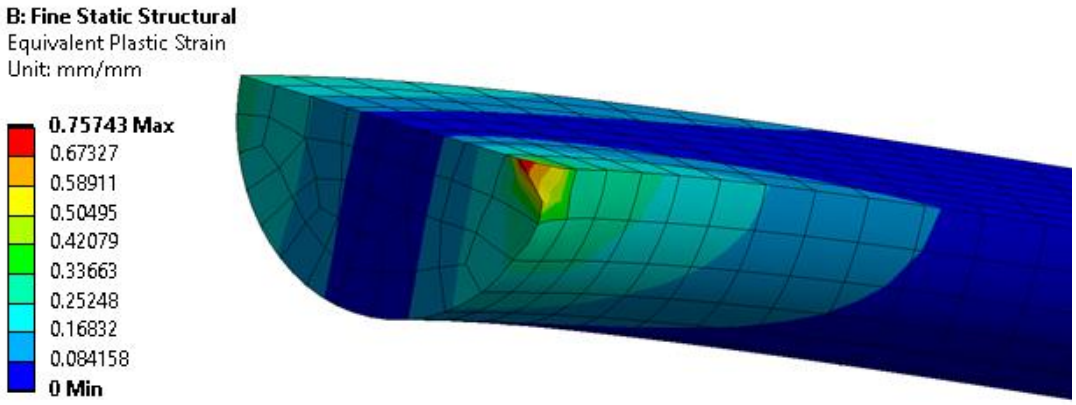

Figure 4-10 Equivalent plastic strain due to bending in the forward direction

The singularity in Figure 4-10 is caused by the bottom support for forward bending. This is the highly distorted element with red/orange/yellow colour scaling. Here the levels of plastic strain are greatly increased and known to be inaccurate. The equivalent plastic strain value of 0.275 mm/mm attributable to the bending in the forward direction was taken from the uniformly shaded area adjacent to the singularity.

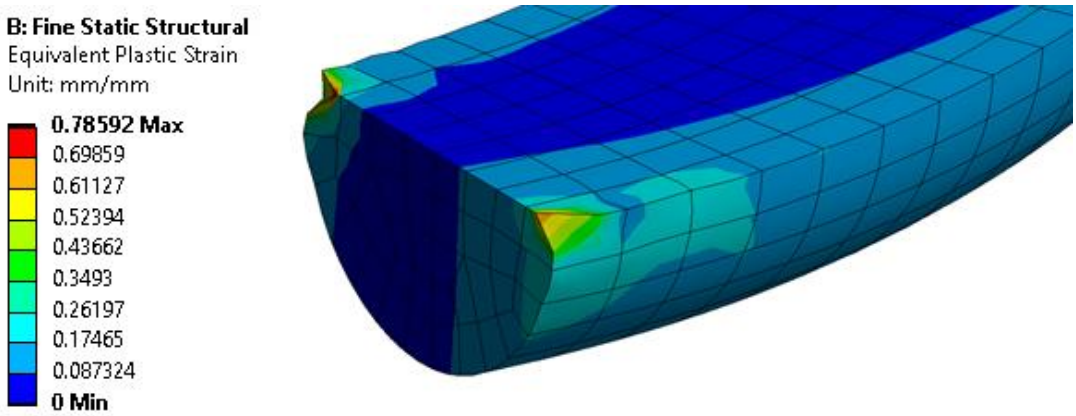

Figure 4-11 Equivalent plastic strain due to bending in the reverse direction

The singularities shown in Figure 4-11 are located at the top and bottom supports. The distorted elements are shown with increased, inaccurate levels of plastic strain. The equivalent plastic strain value of 0.175 mm/mm attributable to bending in the reverse direction was taken from the uniformly shaded area adjacent to the singularities.

© University of Pretoria

The resulting force-time curve is depicted in Figure 4-12. The particular set of time increments used in Figure 4-12 was kept constant to facilitate comparison of curves generated in the parametric study performed in Section 5.4.

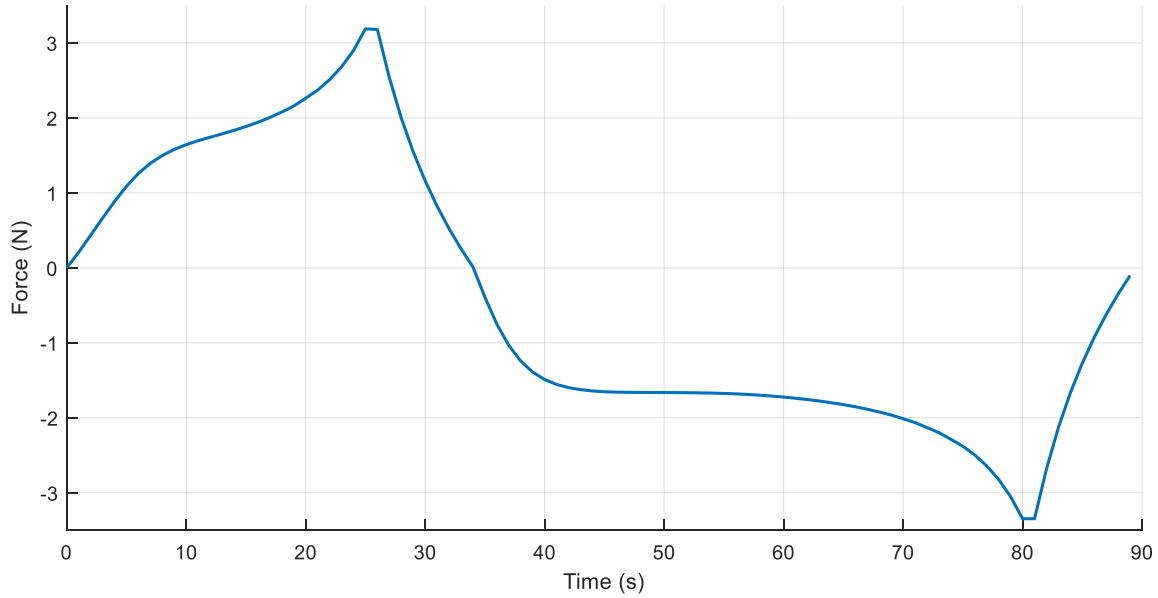

Figure 4-12 Force-time curve, bend test, as-drawn wire

4.6. FORMING THE HOOKED ENDS

A quarter model with planes of symmetry at the midpoint of the length of the fibre and at the centreline of the diameter was used for the forming of the hooked ends. Dimensions are as given in Figure 4-13. The model used for the simulation was developed with the intention of achieving the main dimensions specified in the technical data sheet for our sample fibre as seen in Figure A-4 of Appendix A. It is noted that the forming process used in this simulation is not the same as the real-world forming process where a continuous feed of wire might be pressed and cut in a rotating eccentric die.

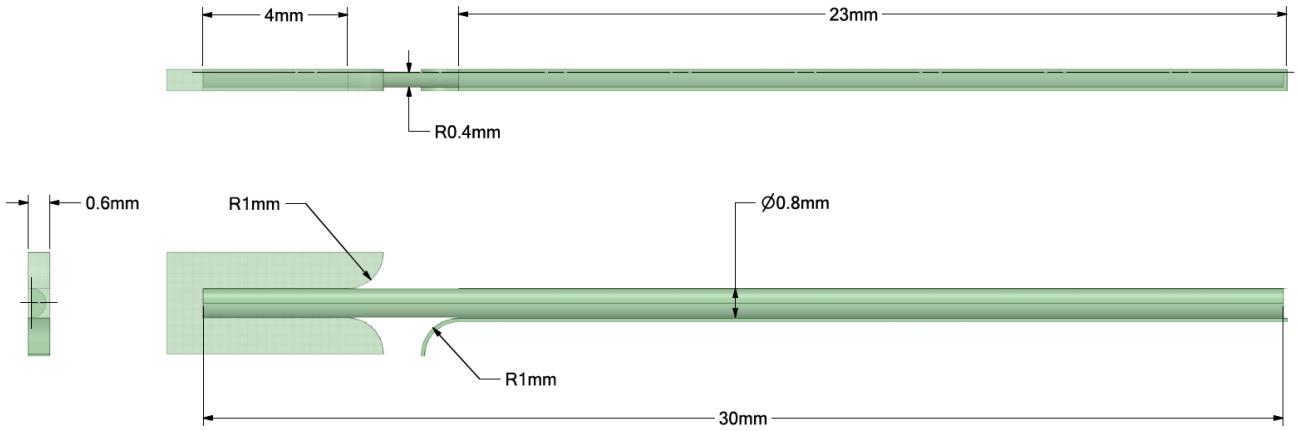

Figure 4-13 Dimensions of the quarter model used for forming the hooked-ends

Boundary conditions were set up to enforce symmetry. The material specification for the grip and forming supports was selected as tungsten carbide for simplicity. Frictionless contact between the wire and the grip surfaces and forming supports minimised the stretching and concomitant thinning of the inclined portion of the fibre as would be anticipated from a real-world forming process. Convergence on the mesh was established as seen in Section B.4 of Appendix B.

© University of Pretoria

The initial state of the wire was defined by the residual stresses and equivalent plastic strains from the 2D axisymmetric wire drawing simulation. The hooked-end was formed using a prescribed displacement on the grip, ensuring that the geometry was fully unloaded and able to return to a relaxed state at the end of the simulation. Resulting dimensions of the hooked-end fibre are given in Figure 4-14

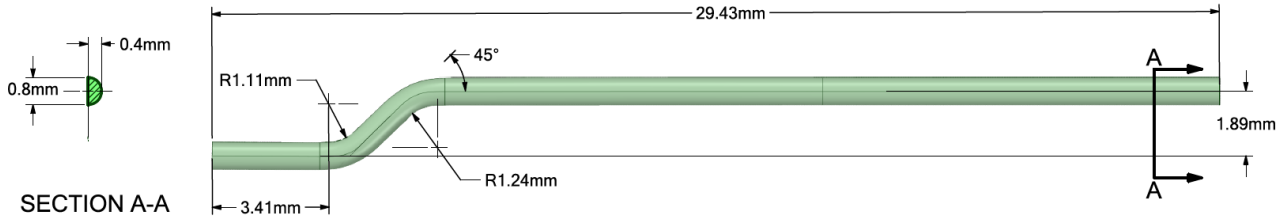

Figure 4-14 Dimensions of the hooked-end fibre formed by simulation

The equivalent plastic strain generated by the hooked-end forming process is depicted in Figure 4-15. It is noted that the regions of plastic strain due to the forming process are localised and that the magnitude decays to a zero value in the middle of the fibre.

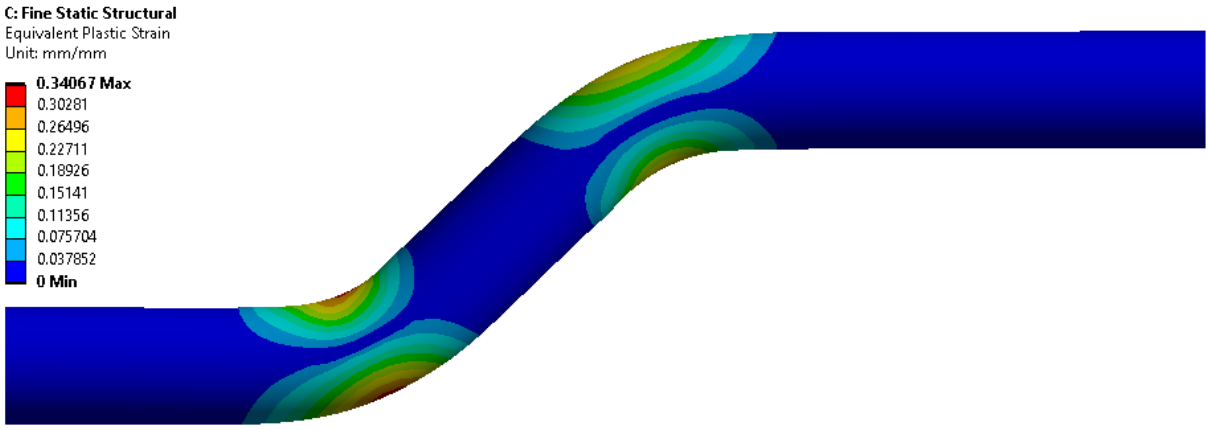

Figure 4-15 Close-up of the equivalent plastic strain at the bend radii

The equivalent plastic strain given in Figure 4-15 does not include the average equivalent plastic strain of 0.818 mm/mm due to the wire drawing process. The increased yield strength of the wire due to drawing was modelled by including, as an initial condition, the equivalent plastic strain profile through the wire attributed to the wire drawing process. This is shown in Figure 4-16 where the plastic strain due to wire drawing is given by the uniform yellow colour, and the localised plastic strain due to the forming of the hooked-ends given by the discrete regions coloured orange and red.

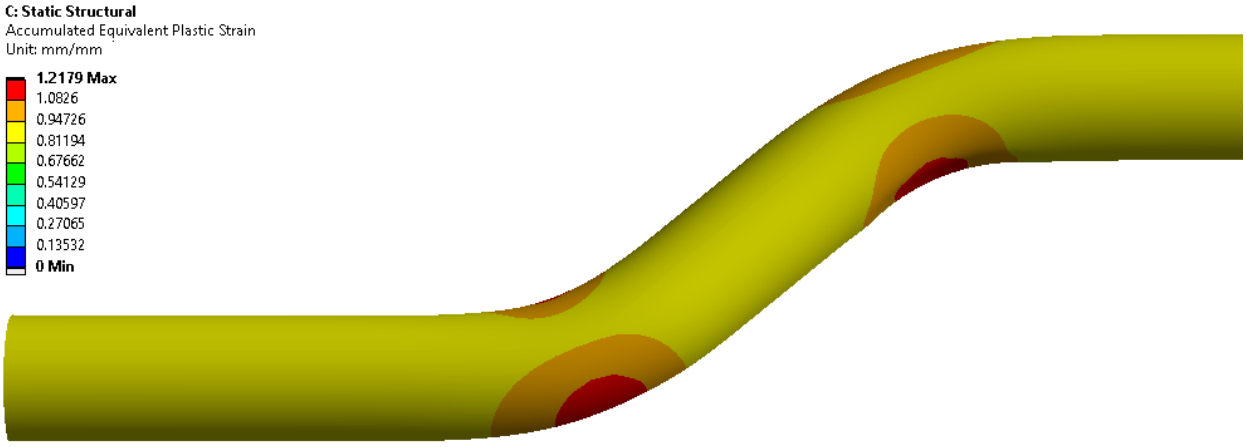

Figure 4-16 Accumulated equivalent plastic strain due to fibre manufacturing process

© University of Pretoria

4.7. PULL-OUT TEST

A pull-out test will now be performed on the hooked-end fibre formed in Section 4.6. The force-displacement curve thus generated will become the baseline curve representing all relevant processes in the manufacture of hooked-end steel reinforcing fibres.

This is followed by a series of sensitivity studies where the relevance of various factors of the fibre manufacturing process in terms of predicting behaviour during pull-out is investigated. The suitability of simple material models as may be estimated by inverse analysis is also investigated.

4.7.1. Setup

The surrounding concrete geometry was created such that the bounds (outside edges) of the concrete in the plane of symmetry along the centreline of the wire were all located at the same distance from the surface of the embedded fibre. Since the fibre does not move in a direction perpendicular to its axis during pull-out, the depth of the concrete was not considered to be critical and an arbitrary value of 2 mm was chosen. This is equal to five times the radius of the wire.

The importance of a sufficiently large surrounding concrete geometry is demonstrated by Figure 4-17. The curve generated using the unconverged geometry with dimensions as depicted in Figure 4-18 fails to define the first and second peaks associated with plastic deformation of the hooked-end and exhibits instability in the portion of the curve associated with frictional pull-out. This is likely due to excessive flexure of the inadequately restrained surrounding concrete.

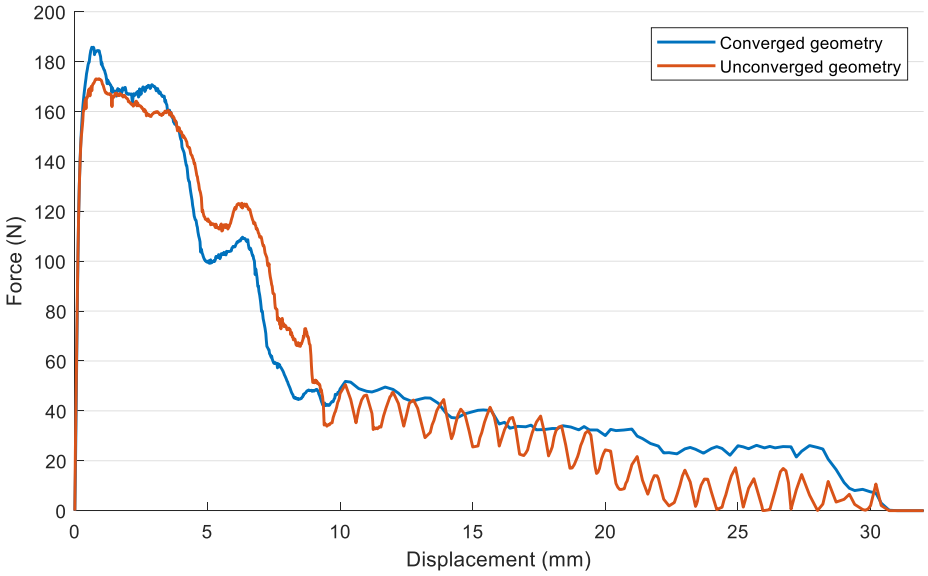

.

Figure 4-17 Comparison of pull-out curves using converged and unconverged concrete geometries

Figure 4-18 Dimensions of the unconverged concrete geometry

The governing dimension for the concrete geometry is the distance between the boundary of the geometry and the surface of the embedded fibre in the plane of symmetry along the centreline of the wire. A convergence study on concrete geometry was performed for governing dimensions of 7 mm and 5 mm. Percentage error in terms of energy associated with pull-out was calculated as:

$$\%\ error = \frac{\mathbb{E}_5 - \mathbb{E}_7}{\mathbb{E}_5} \tag{10}$$

© University of Pretoria

A percentage error of 1.0 was calculated between results obtained using a governing dimension of 5 mm and those using a governing dimension of 7 mm. Convergence was therefore considered to have been achieved on a concrete geometry created using the governing dimension of 5 mm.

Dimensions of the concrete and embedded fibre geometry are as given in Figure 4-19. Convergence on the mesh was established as seen in Section B.5 of Appendix B.

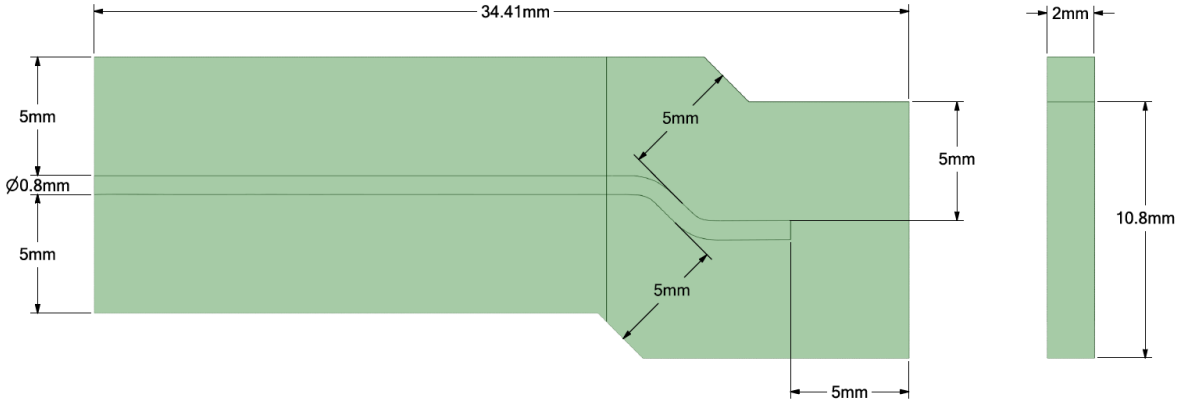

Figure 4-19 Dimensions of the concrete and embedded fibre geometry

A non-linear concrete material model, with properties as given by Table 4-1 [70], was used for the concrete duct. Boundary conditions were set up to enforce symmetry and a prescribed displacement applied to the exposed face of the fibre. The coefficient of friction between the fibre and the concrete duct was equal to 0.1 according to results of a study performed by Khbaz [71].

Table 4-1 Properties Defining the Non-linear Concrete Material Model

Density	2300 kg/m^3
Young's modulus	30 GPa
Poisson's ratio	0.18
Compressive ultimate strength	41 MPa
Tensile ultimate strength	5 MPa
Bulk modulus and shear modulus derived from Young's modulus and Poisson's ratio	

The initial state of the fibre was defined using the complete stress tensor and accumulated equivalent plastic strain results from the hooked-end forming simulation. Equivalent plastic strain was used to define the initial condition since the nature of the plastic deformation experienced by the fibre during the forming of the hooked ends is known.

4.7.2. Baseline force-displacement curve

The baseline pull-out curve is depicted in Figure 4-20. The curve shows the expected features highlighted in Section 2.6.1.2. Particular attention is drawn to the presence of the two peaks attributed to the plastic deformation of the bend radii of the hooked end. Energy absorbed during pull-out is calculated to be equal to 1769.789 Nmm.

It is noted that the force magnitudes depicted in Figure 4-20 are directly related to the use of a half-model of the fibre with a plane of symmetry located at the centreline of the fibre diameter. Force values should therefore be doubled and energy absorbed during pull-out re-calculated accordingly in order to obtain values for the full fibre. In this case, pull-out loads of between 300 to 400 N will be obtained as can be expected for the chosen fibre geometry [72] [73].

© University of Pretoria

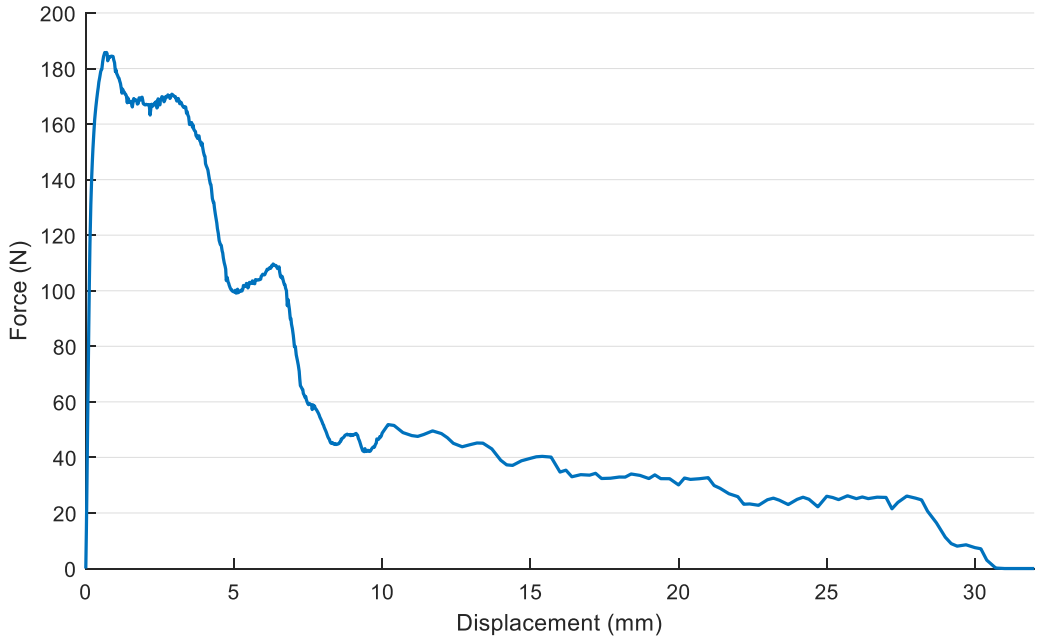

Figure 4-20 Baseline force-displacement curve, pull-out simulation

4.7.3. Nomenclature regarding peaks in pull-out curve

This pull-out curve in Figure 4-20 shows three points which could be considered to be 'peaks'. These will be referred to as 'apparent peaks'. In the literature study, Figure 2-5 makes it clear that only two peaks exist in the pull-out curve; the first associated with plastic deformation of both bend radii of the hooked-end and the second associated with plastic deformation of the last bend radius of the hooked-end.

Figure 4-21 shows the position of the fibre in the cement duct at each apparent peak in the pull-out curve depicted in Figure 4-20. Plastic deformation of both bend radii of the hooked-end can be seen to occur over the first two apparent peaks as depicted by a) and b). Maximum pull-out force as defined by Figure 2-5 is therefore given by the maximum force at the first apparent peak. This peak shall henceforth be known as the first peak. The second apparent peak is therefore a pseudo-peak and will not be referred to again.

© University of Pretoria

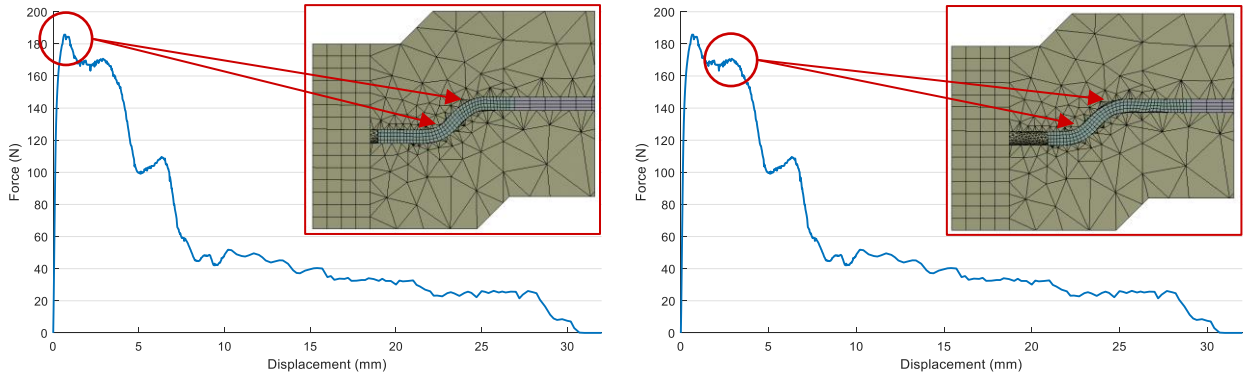

a. First peak
(First apparent peak)

b. Pseudo-peak
(Second apparent peak)

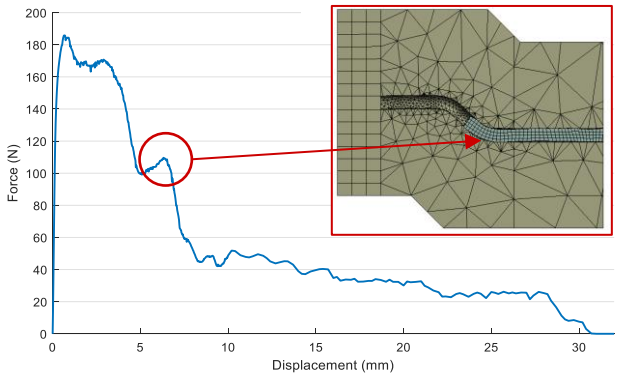

c. Second peak
(Third apparent peak)

Figure 4-21 Position of fibre in cement duct at each apparent peak in the pull-out curve

Plastic deformation of the last bend radius of the hooked-end occurs at the third apparent peak as depicted in c). Maximum pull-out force at the second peak as defined by Figure 2-5 is therefore given by the maximum force at the third apparent peak. This peak shall henceforth be known as the second peak.

4.7.4. Equivalent plastic strain

Figure 4-22 shows the unloaded geometry and equivalent plastic strain due to the bending and reverse bending of the fibre during pull-out. In this figure depicting the relaxed state after complete pull-out, the fibre is seen to exhibit the expected incomplete straightening leading to the three points of contact depicted in Figure 2-9.

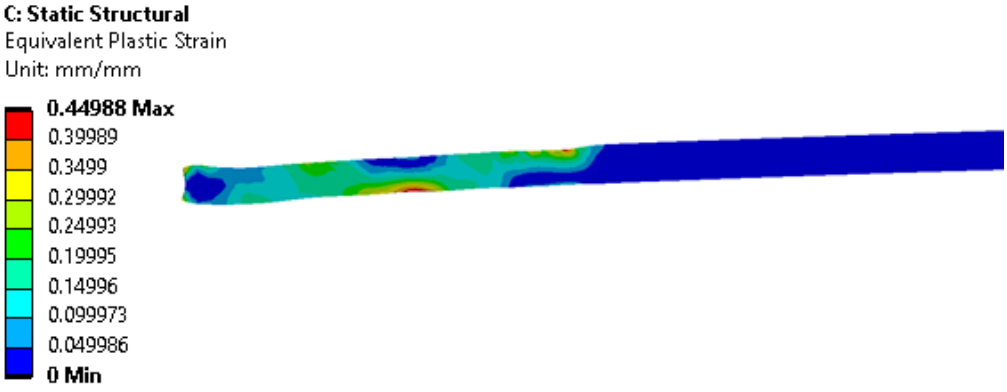

Figure 4-22 Equivalent plastic strain post pull-out

© University of Pretoria

4.8. SENSITIVITY STUDIES

The purpose of the sensitivity study is to determine which aspects of the manufacturing process have the greatest effect on the pull-out curve. Table 4-2 depicts the sets of studies and the configurations that will be examined by each.

Table 4-2 Configurations for Sensitivity Studies

STUDY	RESIDUAL STRESSES	PLASTIC STRAIN DUE TO WIRE DRAWING	HOOKED-END FORMING
Significance of residual stresses with hooked-end forming included	Two profiles	Included	Included
	One profile	Included	Included
	Excluded	Included	Included
Significance of residual stresses with hooked-end forming excluded	Excluded	Included	Excluded
Significance of strain with hooked-end forming included	Included	Excluded	Included
Significance of strain with hooked-end forming excluded	Included	Excluded	Excluded
Significance of hooked-end forming process	Included	Included	Excluded
	Excluded	Excluded	Included
	Excluded	Excluded	Excluded
Significance of the coefficient of friction	Included	Included	Included

In these studies, 'Residual stresses' refers to the residual stress profiles in the as-drawn wire at the end of the drawing process. 'Plastic strain' likewise refers to the equivalent plastic strain profile from the wire drawing process. 'Hooked-end forming' (stresses and plastic strains) refers to the residual stresses and equivalent plastic strains associated with the process of forming the hooked ends.

In keeping with the intent of formulating a simple material model for use in the design of reinforcing fibres, the accuracy of four possible models was investigated. Residual stresses and equivalent plastic strains from the wire drawing process were not included in these models and the hooked-end forming process was not simulated. The simple material models investigated are detailed in Table 4-3.

Table 4-3 Simple Material Models

HARDENING LAW	YIELD STRENGTH	TANGENT MODULUS
Isotropic	Based on plastic strain after wire drawing	Based on plastic strain after wire drawing
Kinematic	Based on plastic strain after wire drawing	Based on plastic strain after wire drawing
Isotropic	Based on plastic strain after wire drawing	Zero
Kinematic	Based on plastic strain after wire drawing	Zero

The energy required for pull-out was used as the basis for calculating the error between curves as follows:

$$\%\ error = \frac{\mathbb{E}_{baseline} - \mathbb{E}_{approx}}{\mathbb{E}_{baseline}} \times 100 \qquad (11)$$

© University of Pretoria

where energy was calculated using backward numerical integration:

$$\mathbb{E} = \sum_{i=1}^{n} (d_i - d_{i-1}) F(d_i) \tag{12}$$

Note that for this and all other tests in this series, 'baseline' refers to a configuration consisting of:

- All three (axial, radial and hoop) residual stress profiles included
- Plastic strain profile due to wire drawing included
- Residual stresses and plastic strains due to hooked-end forming included

4.8.1. Significance of residual stresses with forming included

The importance of the residual stresses resulting from the wire drawing process in terms of their effect on the pull-out behaviour of the reinforcing wire was investigated by simulating a series of pull-out tests on hooked-end fibres with an initial state omitting one or more residual stress profiles as per Table 4-4.

Table 4-4 Studies Testing the Significance of Residual Stresses with Hooked-End Forming Included

RESIDUAL STRESSES	PLASTIC STRAIN DUE TO WIRE DRAWING	HOOKED-END FORMING
Two profiles	Included	Included
One profile	Included	Included
Excluded	Included	Included

For each simulation the wire was initialised with the equivalent plastic strains associated with the wire drawing process and a stress state omitting one or more residual stress profiles. This wire was then subjected to the hooked-end forming process with the resulting geometry and final stress and strain states being used as initial conditions in the subsequent pull-out test.

Pull-out curves are depicted in Figure 4-23 for reinforcing fibres simulated with initial stress states given by two residual stress profiles. Figure 4-24 depicts the pull-out curves with initial stress states given by one residual stress profile. Figure 4-26 depicts the pull-out curve where all residual stress profiles were excluded.

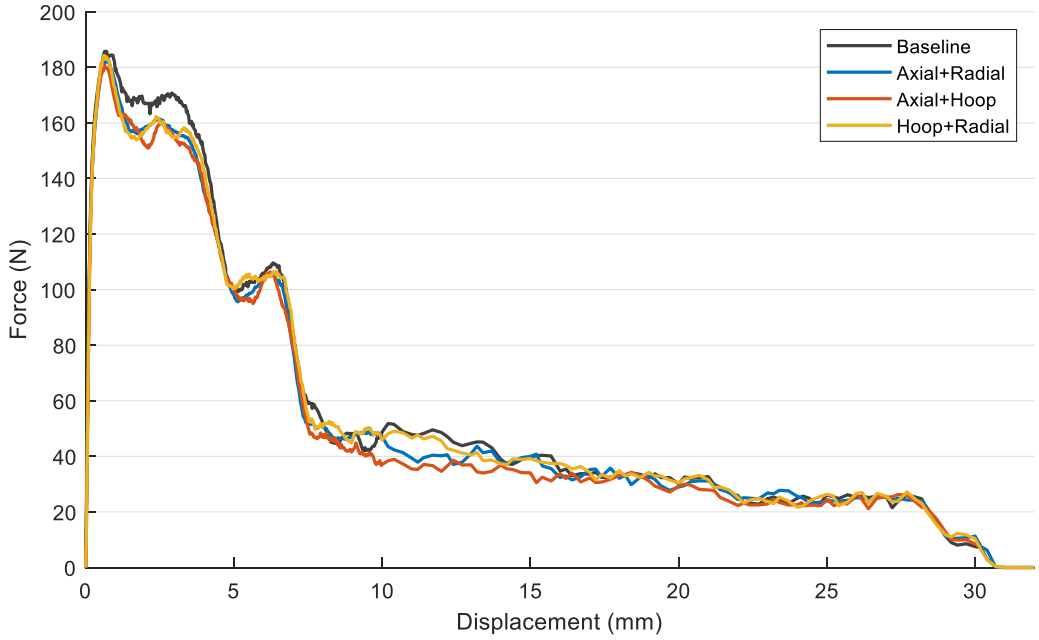

Figure 4-23 Combinations of two residual stress profiles, plastic strain due to wire drawing and forming of the hooked-ends are included

© University of Pretoria

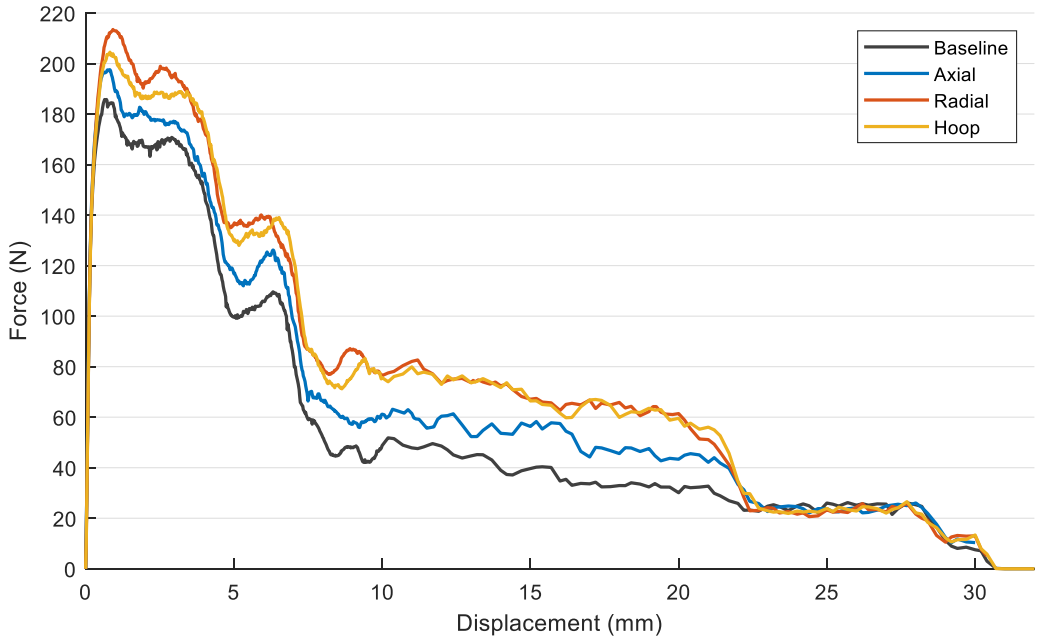

Figure 4-24 Single residual stress profile, plastic strain due to wire drawing and forming of the hooked-ends are included

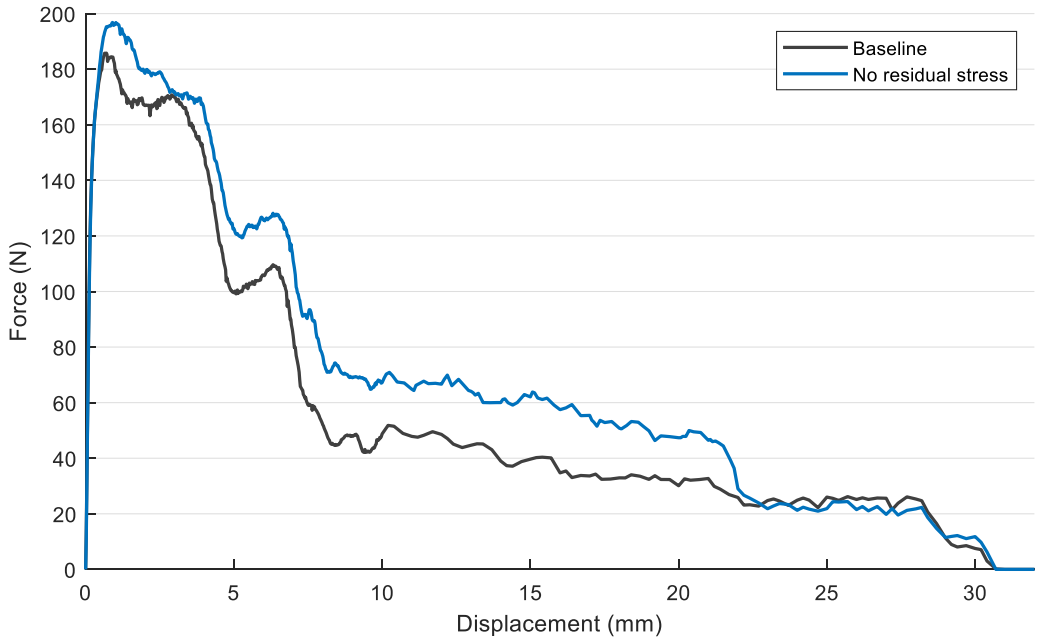

Figure 4-25 Residual stress from wire drawing excluded, plastic strain due to wire drawing and forming of the hooked-ends are included

It is evident that the approximations using two residual stress profiles as depicted in Figure 4-23 are more accurate than the other approximations depicted in Figure 4-24 and Figure 4-25. Close examination of Figure 4-23 reveals that the two peaks on the curve associated with plastic deformation of the hooked-end are best represented using the Axial + Radial profiles, while the rest of the curve is best represented using the Hoop + Radial profiles.

The approximations plotted in Figure 4-24 and Figure 4-25 can be seen to over predict the energy associated with pull-out. Close examination of Figure 4-24 reveals that the two peaks on the curve

© University of Pretoria

are best represented using the Hoop profile. The predicted energy and respective percentage errors in energy approximation are given in Table 4-5.

Table 4-5 Predicted Energy and Percentage Energy Error from Omitting One or More Residual Stress Profiles

RESIDUAL STRESSES CONSIDERED	HOOP + RADIAL	AXIAL + RADIAL	AXIAL + HOOP	AXIAL	NONE	HOOP	RADIAL	ALL
Predicted energy (Nmm)	1728.1	1694.3	1630.8	2049.9	2163.1	2360.5	2388.5	1769.8
Percentage Error	2.36	4.26	7.85	15.83	22.22	33.38	35.0	N/A

The extent of over-prediction of the pull-out energy due to the one-profile approximations is made clear when comparing the values in Table 4-5 with the baseline energy value. Consistent prediction of high forces over much of the displacement appears to contribute to a significantly increased area under the pull-out curve.

Table 4-5 shows that the most accurate two-profile approximation in terms of energy is given by the Hoop + Radial profiles. For conditions where only one residual stress profile is used, the Axial residual stress profile is shown to be the most accurate. It is also shown that the Hoop and Radial residual stress profiles should not be used as single profiles and one is in fact better off eliminating consideration of residual stresses altogether.

4.8.2. Significance of residual stresses with forming excluded

This study considers the significance of the residual stresses when the hooked-end forming process is excluded. Figure 4-25 shows the significance of residual stresses when forming is included. Figure 4-26 depicts the pull-out curve when both residual stresses and forming are excluded in accordance with Table 4-6. The percentage error obtained from this approximation is equal to 0.41.

Table 4-6 Studies Testing the Significance of Residual Stresses with Hooked-End Forming Excluded

RESIDUAL STRESSES	PLASTIC STRAIN DUE TO WIRE DRAWING	HOOKED-END FORMING
Excluded	Included	Excluded

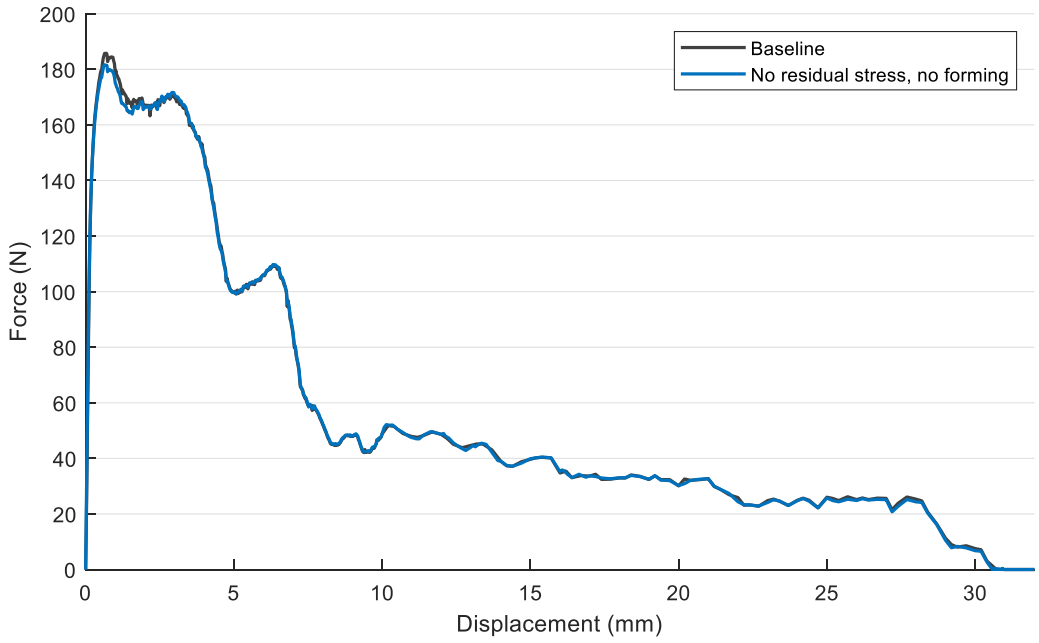

Figure 4-26 Residual stress and hooked-end forming excluded, plastic strain due to wire drawing included

© University of Pretoria

4.8.2.1. Discussion

The percentage errors between the baseline curve and the curves generated by omitting one or more residual stress profiles ranged from 2.36% to 35.0%. The most accurate approximations were generated when only one residual stress profile was omitted.

Figure 4-25 showed that a decent approximation could be obtained by excluding all residual stress profiles entirely. This approximation could be improved significantly from a percentage error of 22.22 to 0.41 by excluding the hooked-end forming process as given by Figure 4-26. It is evident that, when the residual stresses are excluded, including the hooked-end forming process results in reduced accuracy.

At this stage in the sensitivity study, the residual stress profiles do not appear to be significant in terms of predicting behaviour in the pull-out test. These preliminary results indicate that the plastic strain associated with the wire drawing process is the most important factor in terms of pull-out.

4.8.3. Significance of strain with residual stress included

The equivalent plastic strain due to the wire drawing process was seen to be the most important variable according to Sections 4.8.1 and 4.8.2. This was tested by eliminating the equivalent plastic strain attributable to the wire-drawing process and running the simulations detailed in Table 4-7.

Table 4-7 Studies Testing the Significance of Plastic Strain due to Drawing with Residual Stress Included

RESIDUAL STRESSES	PLASTIC STRAIN DUE TO WIRE DRAWING	HOOKED-END FORMING
Included	Excluded	Included
Included	Excluded	Excluded

Figure 4-27 shows the pull-out curves generated for the studies in Table 4-7. The predicted energy and respective percentage errors in energy approximation are given in Table 4-8. It is clear from Table 4-8 that when plastic strain due to wire drawing is not included, the resulting approximation is able to predict just over half of the energy associated with pull-out.

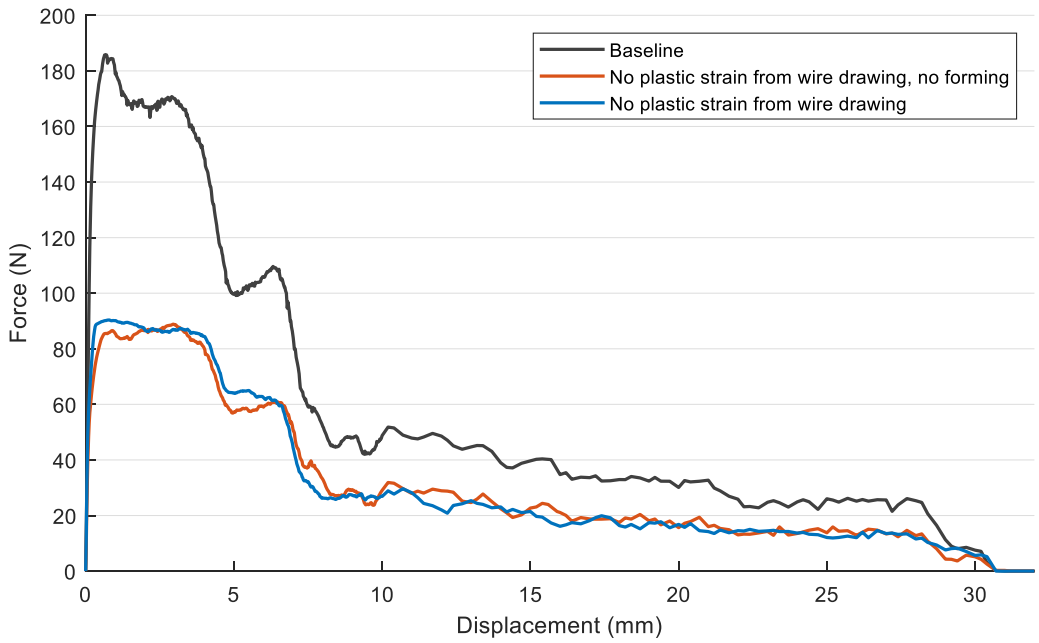

Figure 4-27 Residual stress included, plastic strain due to wire drawing excluded

© University of Pretoria

Table 4-8 Predicted Energy and Percentage Energy Error from Omitting Plastic Strain due to Drawing

HOOKED-END FORMING	INCLUDED	EXCLUDED	BASELINE
Predicted energy (Nmm)	959.4	966.9	1769.8
Percentage Error	45.79	45.36	N/A

Comparison of the percentage errors given in Table 4-8 shows that when the forming process is excluded, the percentage error improves slightly from 45.79 to 45.36. This improvement is not as significant as that associated with including plastic strain due to wire drawing and excluding the residual stress profiles (22.22% to 0.41%), but still serves to indicate that, when the consequences of the wire drawing process are excluded, the consequences of the hooked-end forming process should also be excluded. This will be tested further in Section 4.8.4.

A close examination of the approximation obtained with hooked-end forming excluded in Figure 4-27 reveals that it is able to fairly accurately capture the baseline curve from the point of the second peak onwards. This gives a preliminary indication of the potential for a simple magnitude correction to take the place of the excluded plastic strains due to wire drawing, provided that the hooked-end forming process is also excluded. The effect of such a magnitude correction is depicted in Figure 4-28 where a scaling factor of 1.7 was used. This approximation returned an error of 7.12% on energy.

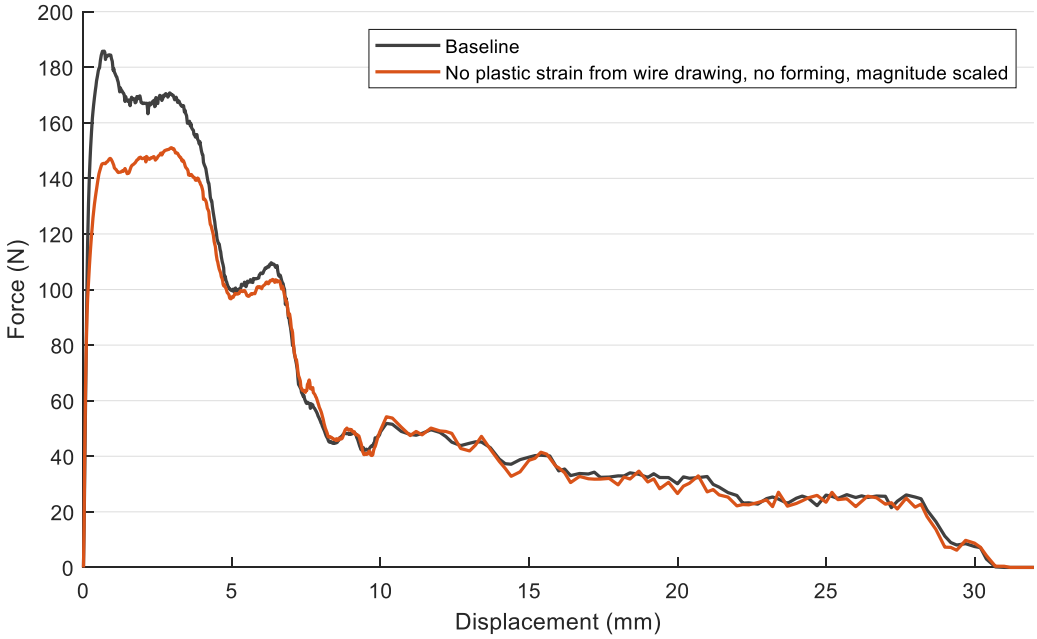

Figure 4-28 Effect of magnitude scaling as compensation for plastic strain from wire drawing

4.8.4. Significance of hooked-end forming process

The results from the previous sensitivity studies indicated that inclusion of the hooked-end forming process was not necessary for predicting behaviour during pull-out. This notion was tested by performing the simulations detailed in Table 4-9.

© University of Pretoria

Table 4-9 Studies Testing the Significance of the Hooked-End Forming Process

RESIDUAL STRESSES	PLASTIC STRAIN DUE TO WIRE DRAWING	HOOKED-END FORMING
Excluded	Excluded	Included
Excluded	Excluded	Excluded
Included	Included	Excluded

Figure 4-29 shows the pull-out curves generated for the first two of these three studies, where residual stresses and plastic strains resulting from the wire drawing process were both excluded. The predicted energy and respective percentage errors in energy approximation are given in Table 4-10.

Table 4-10 Predicted Energy and Percentage Energy Error from Omitting Effects due to Drawing

HOOKED-END FORMING	INCLUDED	EXCLUDED	BASELINE
Predicted energy (Nmm)	997.7	1043.1	1769.8
Percentage Error	43.62	41.06	N/A

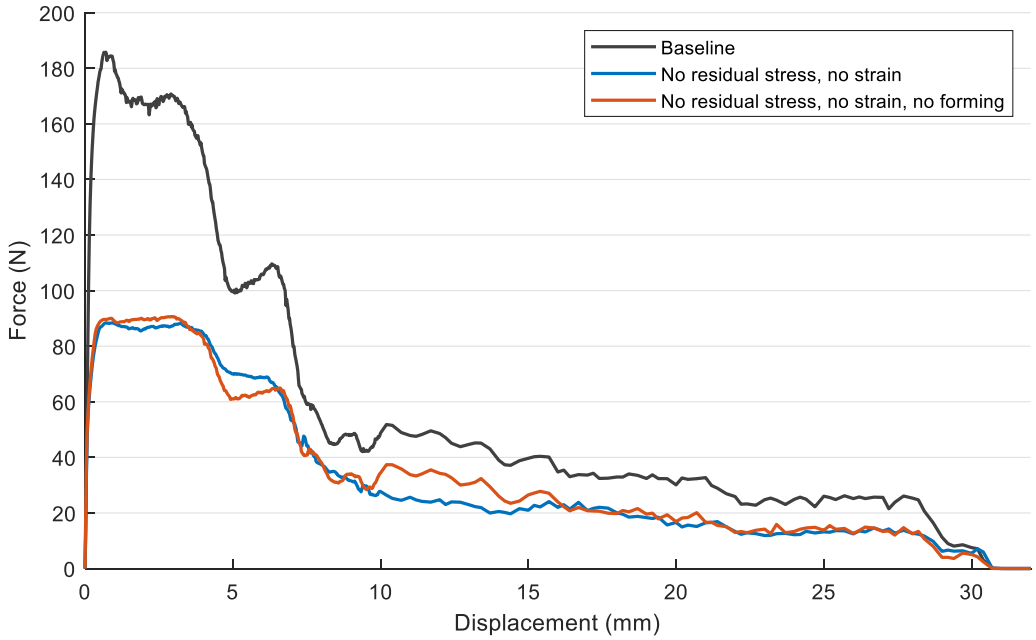

Figure 4-29 Residual stress and plastic strain due to wire drawing excluded, hooked-end forming included and excluded

Comparison of the errors associated with excluding stresses and plastic strains shows that when the forming process is excluded, the percentage error improves slightly from 43.62 to 41.06. It is also noted that the percentage error associated with Figure 4-29 is less than that associated with Figure 4-27, providing further confirmation of the fact that the residual stress profiles are not significant in terms of predicting behaviour in the pull-out test.

The over-all importance of the forming process in terms of its effect on the pull-out behaviour of the reinforcing wire was investigated by simulating the pull-out test with an initial state given by the wire drawing process only. All stresses and strains as a result of the hooked end forming process were ignored. Figure 4-30 shows the pull-out curve generated for this study.

© University of Pretoria

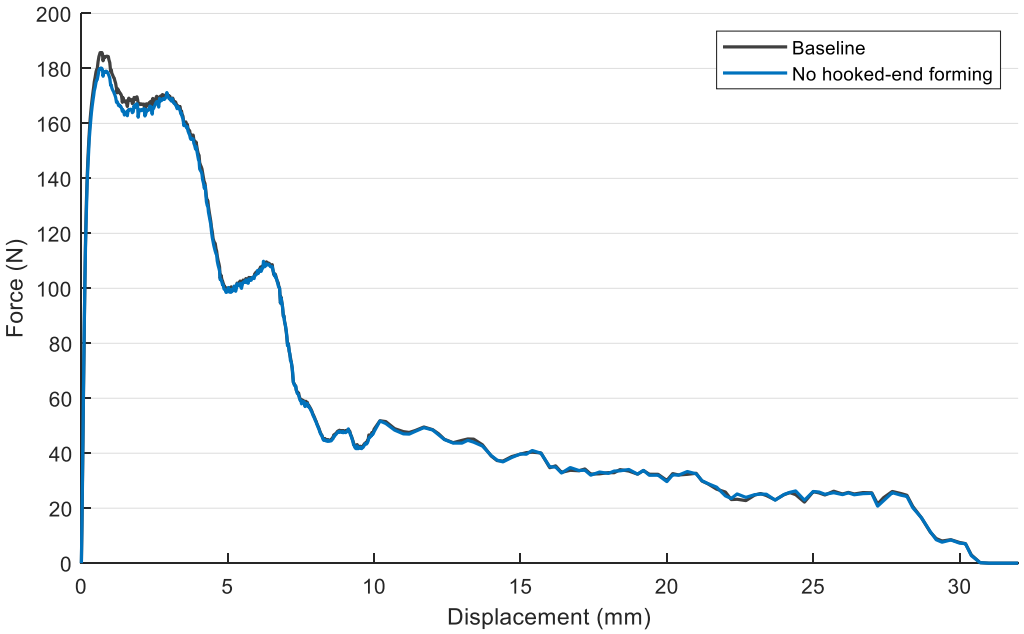

Figure 4-30 Residual stress and plastic strain due to wire drawing included, hooked-end forming excluded

The percentage error obtained from this approximation is equal to 0.87. This result indicates that the simulation of the hooked-end forming process is not absolutely necessary.

When this percentage error is compared with the error of 0.41% obtained in Section 4.8.2 we see that the inaccuracy introduced by excluding the hooked-end forming process may be halved by excluding all residual stress profiles in addition. This provides additional confirmation of the conclusion that the plastic strain associated with the wire drawing process is the most important factor.

4.8.4.1. Discussion

The small percentage error value of 0.41 obtained from Figure 4-26 indicates that there is no meaningful contribution from the stresses and plastic strains attributed to the hooked-end forming process in terms of pull-out. This therefore means that the simulation of the hooked-end forming process and the transfer of related data is not absolutely necessary. A close-up of the equivalent plastic strains in the bend radius of the formed hooked end is given in Figure 4-31.

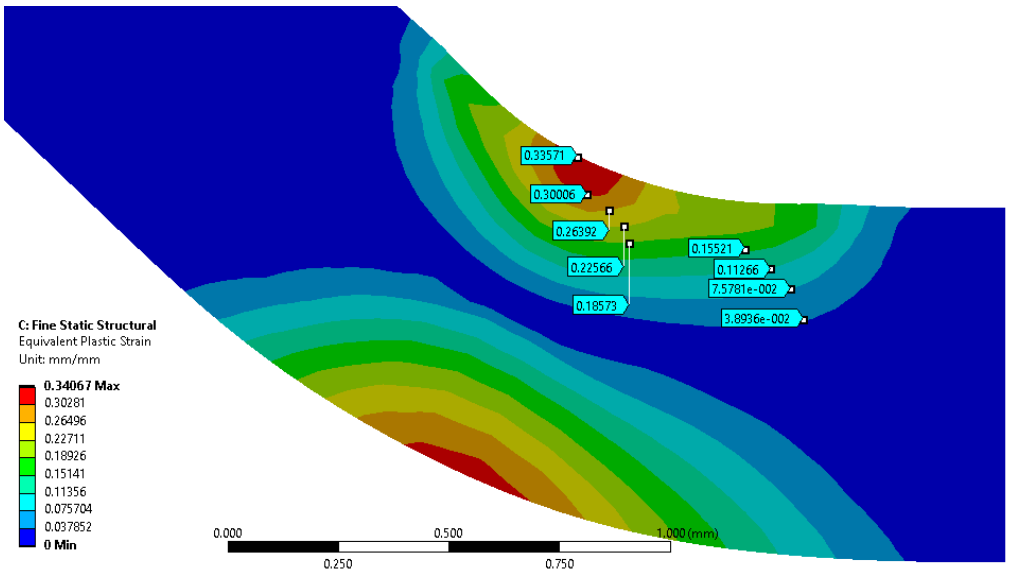

Figure 4-31 Equivalent plastic strains in the bend radius of the formed hooked end

© University of Pretoria

Attention is drawn to the following points of interest in Figure 4-31:

- The maximum equivalent plastic strain value is equal to 0.34 mm/mm. This region of high strain is localised and has a radius of less than 0.1 mm (25% of the fibre radius).
- The equivalent plastic strain decreases to a value of 0.15 mm/mm at a radius of 0.2 mm (44% of maximum strain at 50% of the fibre radius).
- Equivalent plastic strain tends towards a zero value at the middle of the wire.
- The region of increased plastic strain associated with the hooked-end forming process is therefore shown to be localised and to decay quickly to a zero value in the middle of the wire.

It is noted that the maximum equivalent plastic strain due to the wire drawing process was equal to 0.83 mm/mm. The maximum equivalent plastic strain due to the hooked-end forming process can be shown to only contribute approximately 30% of the maximum plastic strain associated with the manufacture of hooked-end fibres. The strains associated with the hooked-end forming process are therefore relatively low in comparison with those of the wire drawing process and mainly concentrated on the surface.

The increase in yield strength associated with the forming process was investigated in Table 4-11. Results show that forming of the hooked ends contributes to an increase in yield strength at the surface of about 131 MPa and about 70 MPa a quarter of the way through the wire diameter.

Table 4-11 Stress and Plastic Strains due to Drawing and Hooked-End Forming Compared

	DUE TO WIRE DRAWING	TOTAL AFTER FORMING AT 0.4mm RADIUS	TOTAL AFTER FORMING AT 0.2mm RADIUS
Strain (mm/mm)	0.83	1.13	0.98
Yield Strength (MPa)	1093.45	1224.55	1162.5

The limited effect of the hooked-end forming process on the pull-out curve is therefore believed to be as a result of the relatively small resulting increase in yield strength at the surface of the wire and the fact that this increase decays rapidly to a zero value close to the middle of the wire.

4.8.5. Significance of coefficient of friction

This study considers the significance of the value of the coefficient of friction on pull-out behaviour when using a constant friction model. The coefficient of friction used to establish the baseline pull-out curve in Section 4.7.1 was equal to 0.1. This study considers a coefficient of friction equal to 0.2 as per Table 4-12. Figure 4-32 depicts the pull-out curve for the increased coefficient of friction.

Table 4-12 Study Testing the Significance of Coefficient of Friction

RESIDUAL STRESSES	PLASTIC STRAIN DUE TO WIRE DRAWING	HOOKED-END FORMING	COEFFICIENT OF FRICTION
Included	Included	Included	0.2

© University of Pretoria

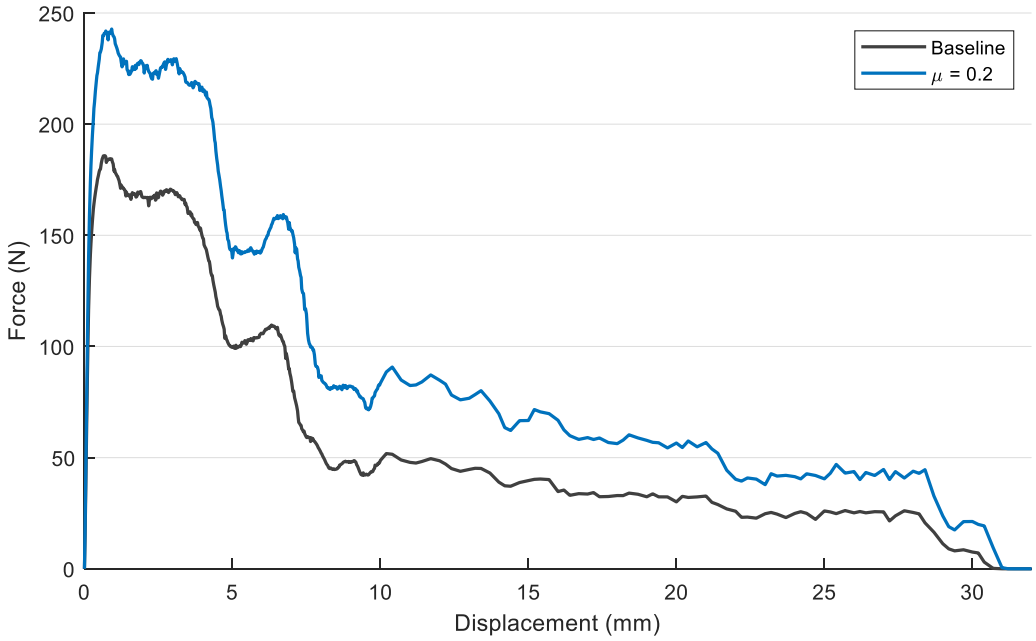

Figure 4-32 Effect of the coefficient of friction on the pull-out curve with residual stress and plastic strain due to wire drawing and hooked-end forming included

The variables used to determine the effect of the increased coefficient of friction are depicted in Figure 4-33. A and B are the maximum pull-out forces at the first peak. C and D are the force values at the start of the plateau when frictional pull-out begins. The values associated with these variables are given in Table 4-13.

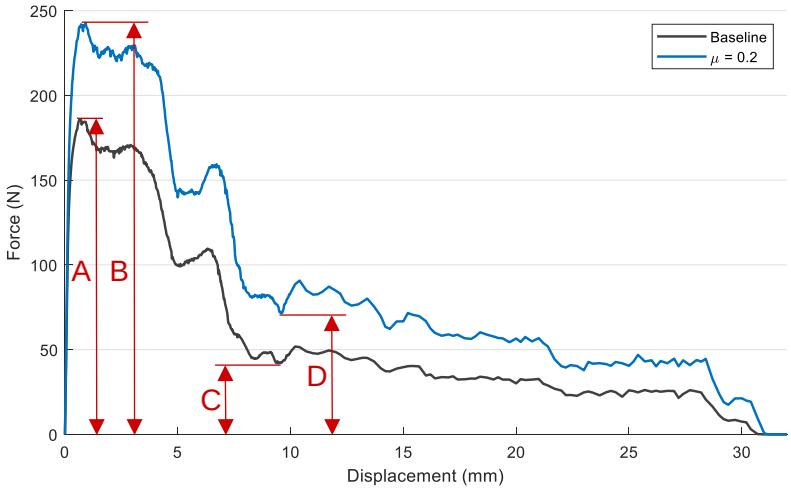

Figure 4-33 Variables used to determine the effect of the coefficient of friction

Table 4-13 Values and Ratios Associated With Effect of Coefficient of Friction on the Pull-Out Curve

A	B	C	D	A/B	C/D
185.79	242.78	42.06	71.49	0.77	0.59

According to Table 4-13, the ratio of maximum pull-out force for a coefficient of friction μ = 0.1 to that for a coefficient of friction μ = 0.2 is equal to 0.77. The ratio of the force at the start of frictional pull-out for a coefficient of friction μ = 0.1 to that for a coefficient of fiction μ = 0.2 is equal to 0.59. It is therefore clear that, for a constant friction model, an increase in the coefficient of friction has a greater effect on the maximum pull-out force than on the force at the start of frictional pull-out.

© University of Pretoria

4.8.6. Simple material model

The results obtained from the investigation into the significance of plastic strain showed that there is potential for a simple, accurate model that excludes the consequences of the wire drawing and hooked-end forming processes and includes some sort of a magnitude scaling factor. Such models would therefore consider only bilinear work hardening or perfect plastic behaviour. The sensitivity of the pull-out curve to the hardening law was tested by employing both isotropic and kinematic hardening in the simple material models.

We have shown that the equivalent plastic strain from the wire drawing process is the most important variable in terms of accurate simulation of the pull-out curves. The magnitude scaling factor would therefore be required to compensate for the fact that this plastic strain would not be explicitly included in the model. An appropriate value for the yield strength was read off the material stress-plastic strain curve at the average equivalent plastic strain value of 0.818 mm/mm due to wire drawing as depicted in Figure 4-34. The tangent modulus was calculated from the slope between this plastic strain and the next value, 0.84 mm/mm and is also depicted in Figure 4-34. Accordingly, the yield strength is equal to 1087 MPa and the tangent modulus is equal to 489 MPa. These values as given in Table 4-14 will henceforth be referred to as the known solution for the bilinear material model.

Table 4-14 Known Solution for the Bilinear Material Model

	YIELD STRENGTH (MPa)	TANGENT MODULUS (MPa)
Known solution	1087	489

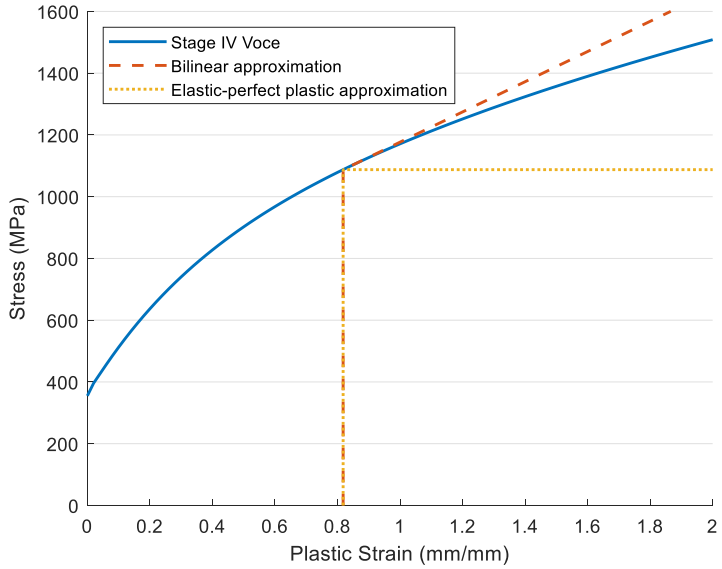

Figure 4-34 Bilinear and elastic-perfect plastic material models as determined from stress-plastic strain curve

Pull-out curves generated using the bilinear material models are depicted in Figure 4-35. The percentage error obtained using the bilinear isotropic approximation was 0.19. The percentage error obtained using the bilinear kinematic approximation was 3.93.

© University of Pretoria

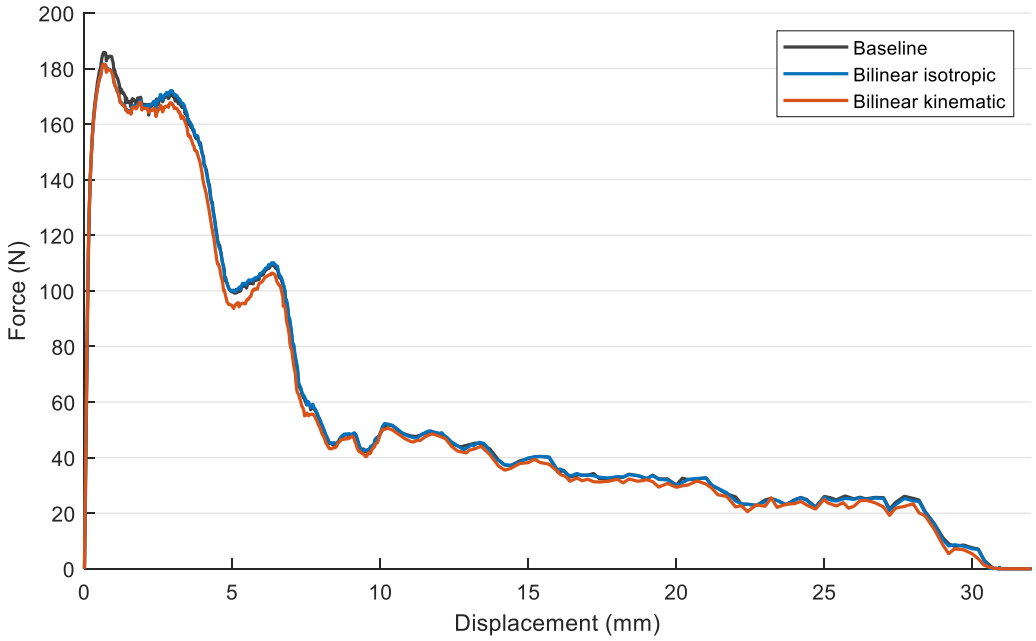

Figure 4-35 Pull-out curves for the bilinear material models

The elastic-perfect plastic material model is depicted in Figure 4-34. The yield strength was calculated in the same manner as for the bilinear material model with a zero-value used for the tangent modulus. Figure 4-36 shows the pull-out curves for the further simplified elastic-perfect plastic material models. The percentage error obtained for both approximations was 03.18.

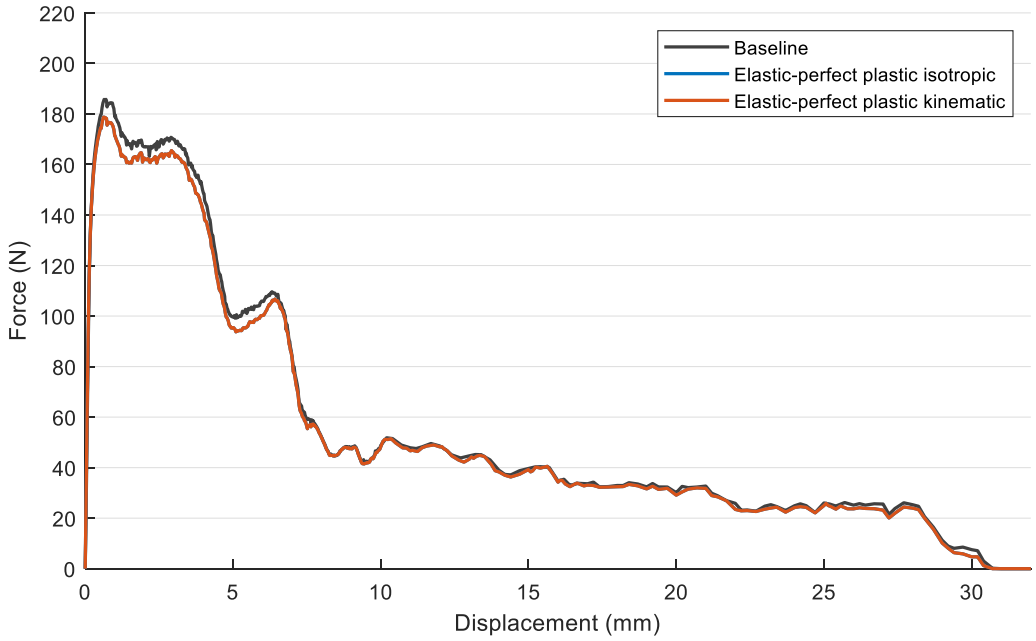

Figure 4-36 Pull-out curves for the elastic-perfect plastic material models

The low percentage errors obtained from the approximations depicted in Figure 4-35 and Figure 4-36 provides confirmation that a simple material model may be used to account for the effects of the wire drawing process, provided the associated plastic strains are known or can be accurately estimated. The relatively low errors also indicate that performance during pull-out is somewhat insensitive to the hardening law.

© University of Pretoria

4.8.7. Summary, results of sensitivity studies

A summary of the results from the sensitivity studies is given in Table 4-15, arranged from the most accurate approximation to the least.

Table 4-15 Summary of Errors Associated with Approximate Material Models

PERCENTAGE ERROR	RESIDUAL STRESS	STRAIN	FORMING	HARDENING LAW	MATERIAL MODEL
0.19	None	None	None	Isotropic	Bilinear
0.41	None	Yes	None	Isotropic	Stage IV Voce
0.87	All	Yes	None	Isotropic	Stage IV Voce
2.36	Hoop and Radial	Yes	Yes	Isotropic	Stage IV Voce
3.18	None	None	None	Isotropic	Elastic perfect plastic
3.18	None	None	None	Kinematic	Elastic perfect plastic
3.93	None	None	None	Kinematic	Bilinear
4.26	Axial and Radial	Yes	Yes	Isotropic	Stage IV Voce
7.85	Axial and Hoop	Yes	Yes	Isotropic	Stage IV Voce
15.83	Axial	Yes	Yes	Isotropic	Stage IV Voce
22.22	None	Yes	Yes	Isotropic	Stage IV Voce
33.38	Hoop	Yes	Yes	Isotropic	Stage IV Voce
34.96	Radial	Yes	Yes	Isotropic	Stage IV Voce
41.06	None	None	None	Isotropic	Stage IV Voce
43.62	None	None	Yes	Isotropic	Stage IV Voce
45.36	All	None	None	Isotropic	Stage IV Voce
45.79	All	None	Yes	Isotropic	Stage IV Voce

© University of Pretoria

CHAPTER 5 - THE INVERSE PROBLEM

5.1. OVERVIEW

In Chapters 2 and 3 we learned that a known wire drawing process is complex and hence difficult to model. The exact nature of a wire drawing process is often proprietary, creating an additional barrier to accurate simulation. There is therefore no suitable direct method for accurately obtaining the material properties for a given length of wire. An inverse approach to the problem is proposed to determine whether the unknown material properties may be inferred from a set of known data, the end goal of which is to facilitate the design of steel reinforcing fibres.

Reinforcing fibre designs are typically tested using the experimental pull-out test. This test is expensive and hence can only accommodate a limited number of design changes. Optimisation of the design using experimental methods is therefore not practical. Numerical simulation of the pull-out test has a low cost and is well suited to the design optimisation process. Currently, however, simulation is obstructed by the unknown material properties of the starting product, viz. the as-drawn wire.

In Section 4.8 we used the results of a simulated hooked-end fibre manufacturing process and pull-out test to determine which aspects of the process were most relevant to the pull-out curve. We concluded that the most accurate approximation for the pull-out curve was generated using a bilinear isotropic material model with the yield strength and tangent modulus calculated from the material's stress-strain curve at the average equivalent plastic strain value obtained at the end of the wire drawing process.

Since the stress-strain curve of the material will typically be unknown in practice, this chapter investigates the possibility of obtaining the required material properties (yield strength and tangent modulus) from the stress-strain curve generated from a tensile test. Additionally, in Section 2.7, we learned that the main energy absorption mechanism active during the pull-out test for a hooked-end fibre is related to the mechanical deformation of the fibre during pull-out, that is, bending and reverse bending. The possibility of obtaining the required material properties from the simple bend test will therefore also be investigated.

The hooked-end forming process was excluded from this part of the study due to the fact that its inclusion was shown to substantially increase the error in approximation of the pull-out curve. Residual stress profiles due to the wire-drawing process were likewise excluded based on the results of the studies performed in Section 4.8.

5.2. THE TWO-VARIABLE PROBLEM

The conclusion of Chapter 4 is that variables related to the work hardened state of the material after wire drawing are the most relevant in terms of behaviour during pull-out. Since the wire drawing process involves plastic strains of the order unity [12] the slope of the stress-plastic strain curve becomes approximately linear in the region of interest. This is depicted in Figure 5-1.

© University of Pretoria

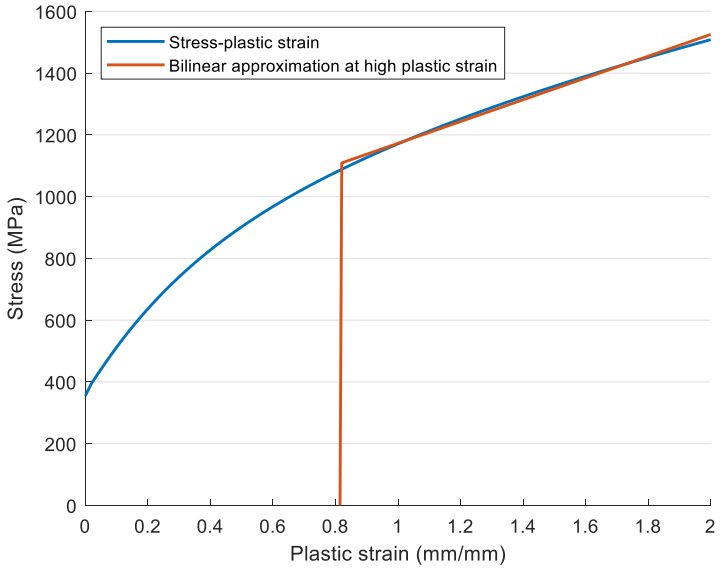

Figure 5-1 Bilinear nature of cold-drawn wire

Figure 5-1 shows that a bilinear stress-plastic strain curve is a suitable approximation for a material subjected to the wire drawing process. The yield strength gives the starting point of the curve and the tangent modulus gives the linear slope of subsequent work hardening.

5.3. CHARACTERISATION USING THE TENSILE TEST

In this section we will examine the possibility of using the results of the simulated tensile test on the as-drawn wire to estimate the starting material stress-strain curve. The following properties were calculated from the engineering stress-strain curve generated from the simulated tensile test in Figure 4-3:

- Using the 0.2% offset, yield strength = 1040.85 MPa
- From the slope between the point giving the yield strength and the next point on the stress-strain curve, tangent modulus = 596.83 MPa

Candidate material models, as defined by Table 5-1, were subjected to the pull-out test. The predicted energy, first and second peak forces and percentage errors obtained using each model are given in Table 5-2 together with information corresponding to the baseline curve. Pull-out curves are depicted in Figure 5-2.

Table 5-1 Material Parameters, Characterisation Using Tensile Test

HARDENING LAW	YIELD STRENGTH (MPa)	TANGENT MODULUS (MPa)
Known solution	1087	489
Bilinear Isotropic	1040.85	596.83
Bilinear Kinematic	1040.85	596.83
Isotropic Elastic-Perfect Plastic	1040.85	0
Kinematic Elastic-Perfect Plastic	1040.85	0

© University of Pretoria

Table 5-2 Energy, Force and Percentage Errors in Approximation: Pull-Out Test from Tensile Test Parameters

	BILINEAR ISOTROPIC	ELASTIC PERFECT PLASTIC ISOTROPIC	ELASTIC PERFECT PLASTIC KINEMATIC	BILINEAR KINEMATIC	BASELINE
Predicted energy (Nmm)	1738.3	1671.8	1671.8	1657.8	1769.79
Percentage error energy	1.78	5.54	5.54	6.33	N/A
Force 1st peak (N)	176.86	173.38	173.38	176.75	185.79
Percentage error 1st peak	4.81	6.68	6.68	4.87	N/A
Force 2nd peak (N)	107.98	103.32	103.32	103.19	109.11
Percentage error 2nd peak	1.03	5.28	5.28	5.40	N/A

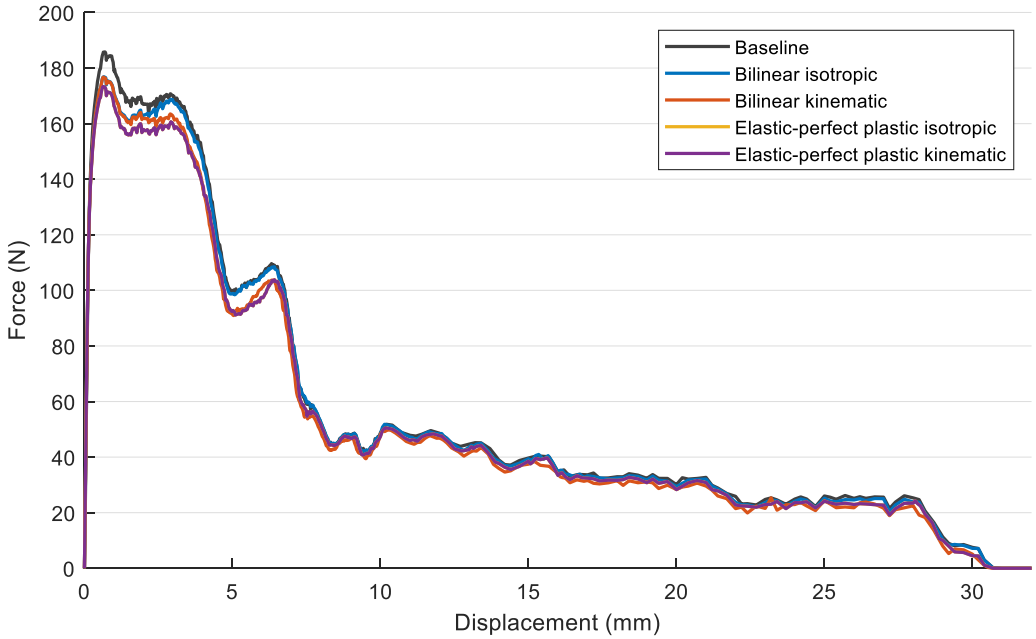

Figure 5-2 Approximation based on tensile test

Examination of Figure 5-2 shows that all approximation material models under-predict the force during pull-out. Qualitatively, the bilinear isotropic model can be seen to result in the best approximation, particularly from the second peak onwards.

5.4. CHARACTERISATION USING THE BEND TEST

In this section we will be examining the possibility of using the results of the simulated bend test on the as-drawn wire to estimate the starting material stress-strain curve. The force-time curve generated from the simulated bend test in Figure 4-12 was used as the baseline.

5.4.1. Design of experiments

Latin Hypercube Sampling (LHS) is a stratified sampling approach that ensures that all portions of the domain are sampled [74]. LHS was used to specify 50 sample points, consisting of a yield and tangent modulus value. Bounds for sampling were chosen as follows:

- Yield strength 500 – 2000 MPa
- Tangent modulus 0 – 3000 MPa

© University of Pretoria

5.4.2. Numerical simulation at selected locations

A series of bend tests identical to that detailed in Section 4.5 were performed for the bilinear material models defined by the 50 sample points. Two sets of studies were conducted, one using the isotropic material model, and one using the kinematic material model.

The output of these studies was a set of 50 force-time curves. Force results were extracted at 98 specific time values on each curve for the isotropic studies and 109 specific time values on each curve for the kinematic studies.

5.4.3. Construction of surrogate model

One surrogate surface was constructed for the isotropic material model, and one for the kinematic material model. For each set of studies, at each of the 50 sample points, the error between the output force value, $F_{SP}(\boldsymbol{t}, \mathbf{x}^i)$ given by Section 5.4.2, and the baseline force value, $F_{BL}(\boldsymbol{t})$ given by Figure 4-12, was calculated by taking the norm of the squared difference. The error function at each sample point is therefore given by:

$$f^i(\mathbf{x}) = \left\| F_{BL}(\boldsymbol{t}) - F_{SP}(\boldsymbol{t}, \mathbf{x}^{\boldsymbol{i}}) \right\|, \qquad \text{for } i = 1{:}\, k, k = 50 \tag{13}$$

where $\mathbf{x}^{\boldsymbol{i}}$ is the sample point vector of the yield strength and tangent modulus values and k is the number of sample points.

The error function $f(\mathbf{x})$ is approximated using a surrogate surface with the form [75]:

$$\tilde{f}(\mathbf{x}) = \sum_{i=1}^{k} \boldsymbol{w}^i \phi^i(\mathbf{x}, \mathbf{x}_{\boldsymbol{c}}), \quad \text{for } k = 50 \tag{14}$$

and is constructed as an interpolation function. The functions $\phi^i(\mathbf{x})$ used to construct the surrogate surface were selected as Gaussian Radial Basis Functions (RBF) given by [75]:

$$\phi^i(\mathbf{x}) = e^{-\epsilon \|\mathbf{x} - \mathbf{x}_c^i\|^2} \tag{15}$$

where:

- $\mathbf{x}_c^i$ are the points about which the basis functions are centred which, for the interpolation function, are the sample points
- ϵ is the shape parameter

The weight vector $\boldsymbol{w}^i$ in equation (14) is solved for each value of ϵ by evaluating [75]:

$$\begin{bmatrix} \phi^1(\mathrm{x}^1, \mathrm{x}_c^1) & \phi^2(\mathrm{x}^1, \mathrm{x}_c^2) & \cdots & \phi^k(\mathrm{x}^1, \mathrm{x}_c^k) \\ \phi^1(\mathrm{x}^2, \mathrm{x}_c^1) & \phi^2(\mathrm{x}^2, \mathrm{x}_c^2) & \cdots & \phi^k(\mathrm{x}^2, \mathrm{x}_c^k) \\ \vdots & & & \\ \phi^1(\mathrm{x}^k, \mathrm{x}_c^1) & \phi^2(\mathrm{x}^k, \mathrm{x}_c^2) & \cdots & \phi^k(\mathrm{x}^k, \mathrm{x}_c^k) \end{bmatrix} \begin{bmatrix} w^1 \\ w^2 \\ \vdots \\ w^k \end{bmatrix} = \begin{bmatrix} f^1 \\ f^2 \\ \vdots \\ f^k \end{bmatrix} \tag{16}$$

5.4.4. Model validation

The optimum value for ϵ for which the error between the surrogate surface $\tilde{f}(\mathbf{x})$ and the error function $f(\mathbf{x})$ is a minimum was determined using Leave-One-Out-Cross-Validation (LOOCV) on 1400 values of ϵ in the domain 10^{-4} to 10^{-3}. LOOCV was chosen because it allows for the use of all available data in constructing the surrogate [74].

The optimum ϵ value thus determined was used in equation (15) together with its associated weight vector calculated using equation (19) to create the surrogate surface given by equation (14). The LOOCV error associated with different values for ϵ is depicted in Figure 5-3. A value of $\epsilon = 3.673 \times 10^{-2}$ can be seen to result in the lowest LOOCV error value for the kinematic model and $\epsilon = 2.985 \times 10^{-3}$ for the isotropic model.

© University of Pretoria

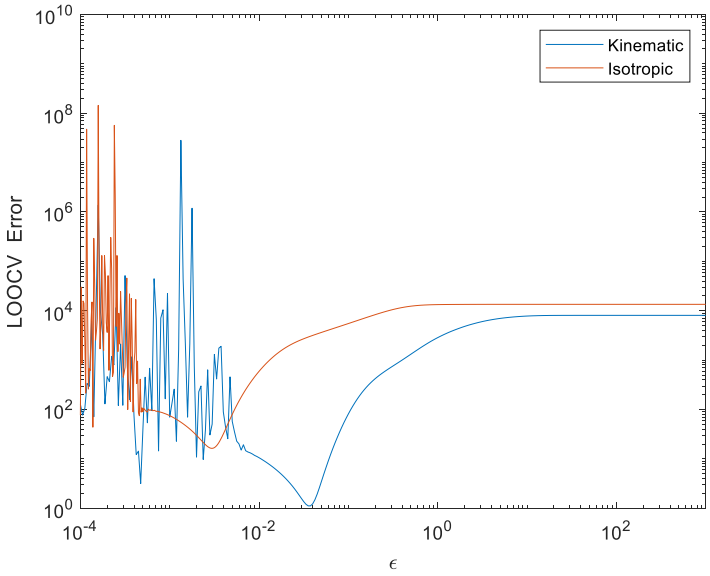

Figure 5-3 Surrogate surface LOOCV error associated with various values of ϵ for characterisation of material model using the bend test

Figure 5-3 shows considerable instability at ϵ values below 10^{-2} for the kinematic model and below 10^{-3} for the isotropic model. Optimum values for ϵ were therefore only considered relevant once the LOOCV error curve became smooth.

5.4.5. Optimisation

Constrained optimisation using sequential quadratic programming on the surrogate surface for 50 random starting points returned candidate material parameters given by the averaged results at the local minimum. There was one local minimum for the isotropic parametric studies and three for the kinematic studies. The results of this optimisation are given in Table 5-3.

Table 5-3 Material Parameters, Characterisation Using Bend Test

HARDENING LAW	YIELD STRENGTH (MPa)	TANGENT MODULUS (MPa)
Known solution	1087	489
Isotropic	1085.4	419.5
Kinematic 1	1188	1745.2
Kinematic 2	1249	432
Kinematic 3	1276	0

The surrogate surface generated by equation (14) for the isotropic material model is shown in Figure 5-4. The dark blue region corresponding to minimum values of $\tilde{f}(\mathbf{x})$ is clearly shown for a range of yields strength and tangent modulus values, along with the maximum errors corresponding to the maximum coincident values for yield strength and tangent modulus.

Figure 5-4 also depicts the dependence of the error on yield strength and tangent modulus, and clearly demonstrates that the yield strength has a greater effect on error than the tangent modulus. This corresponds to the results of the sensitivity studies performed in Section 4.8 where an elastic-perfect plastic material model was shown to provide a reasonable approximation. Also shown is the fact that increased yield strength values increase the sensitivity of the error to tangent modulus.

© University of Pretoria

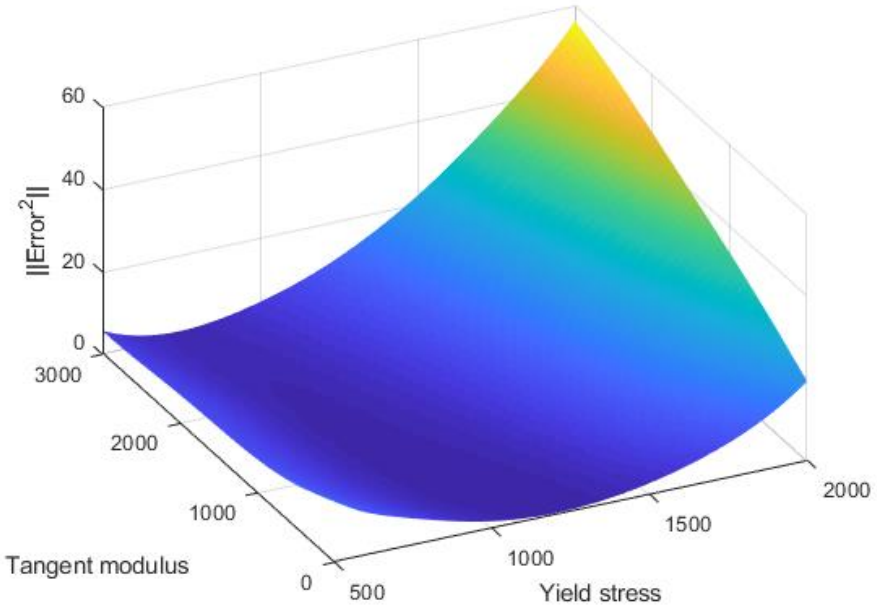

Figure 5-4 Surrogate surface for the isotropic material model

The surrogate surface generated by equation (14) for the kinematic material model is shown in Figure 5-5. The dark blue region corresponding to minimum values of $\tilde{f}(\mathbf{x})$ is clearly shown for a limited range of yield strength values and a wide range of tangent modulus values. Maximum errors corresponding to the lower and upper bounds for yield strength are also shown.

Figure 5-5 also depicts the pronounced dependence of the error on yield strength and the slight dependence on tangent modulus. This also corresponds to the results of the sensitivity studies performed in Section 4.8 where an elastic-perfect plastic kinematic material model was shown to provide an approximation of similar accuracy to the bilinear kinematic approximation. In contrast to the isotropic material model, Figure 5-5 shows that the error in the kinematic material is fairly independent of the tangent modulus value.

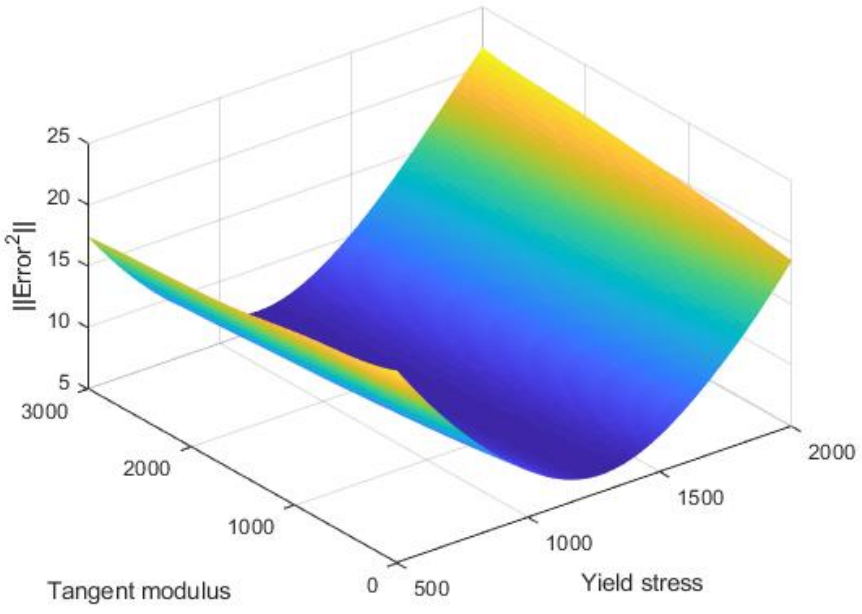

Figure 5-5 Surrogate surface for the kinematic material model

© University of Pretoria

A comparison of the error magnitudes for the isotropic and kinematic surrogate surfaces shows that the isotropic surface is able to achieve an error value of close to zero, while the minimum achievable error for the kinematic surface is 5. This is to be expected since the original material model was chosen to be isotropic. The fact that the kinematic surface is able to provide a reasonable approximation highlights the fact that the behaviour of the material during bending and reverse bending is not overly sensitive to the hardening law.

5.4.6. Verification using the bend test

The material parameters given in Table 5-3 were verified by performing a bend test and comparing the results thereof to the baseline force-time curve. Average percentage errors for the approximations are given in Table 5-4. Comparisons of the approximation force-time curves with the baseline curve are given in Figure 5-6 for the isotropic hardening law and Figure 5-7 for the kinematic hardening law.

The average percentage error is given by:

$$\%\ error = \frac{\frac{\sum|F_{BL} - F_{approx}|}{n}}{\frac{\sum|F_{BL}|}{n}} \times 100 \tag{17}$$

where:

- F_{BL} is the force value at a particular time point on the baseline bend test force-time curve
- F_{approx} is the corresponding force value from the force-time curve of the approximation model
- n is the number of specific time points along the curve

Table 5-4 Average Percentage Error from Approximation Bend Tests

HARDENING LAW	ISOTROPIC	KINEMATIC 1	KINEMATIC 2	KINEMATIC 3
Percentage Error	0.70	10.99	8.65	8.62

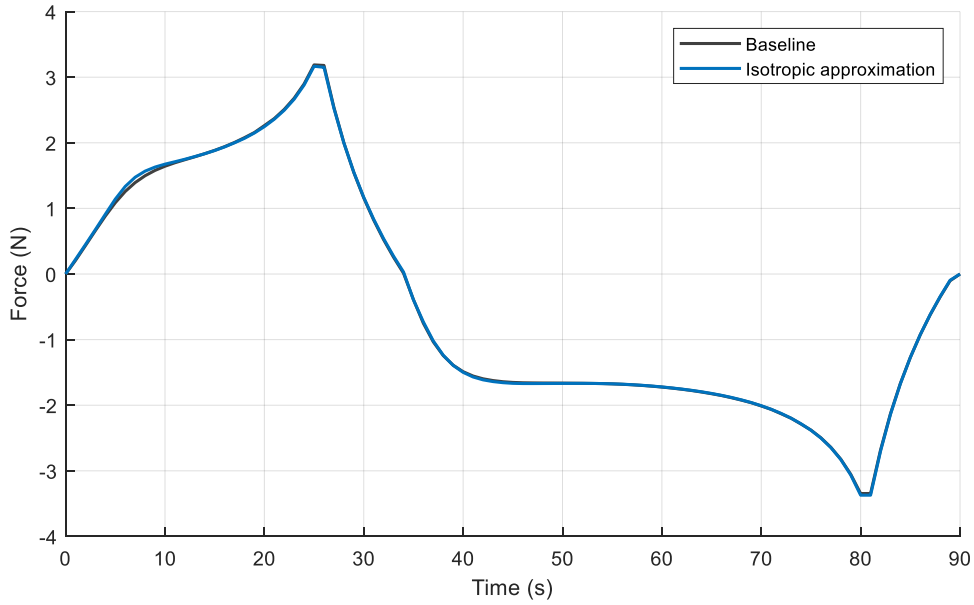

Figure 5-6 Force-time curve comparison, isotropic vs baseline

The approximation depicted in Figure 5-6 is seen to be good overall, with most of the error due to the inability of the approximation to model the behaviour of the material immediately after yielding during forward bending. The behaviour during reverse bending is captured very well. When the error

© University of Pretoria

due to the approximation of the material behaviour immediately after yielding is neglected, the average percentage error in approximating the rest of the curve is only equal to 0.45%.

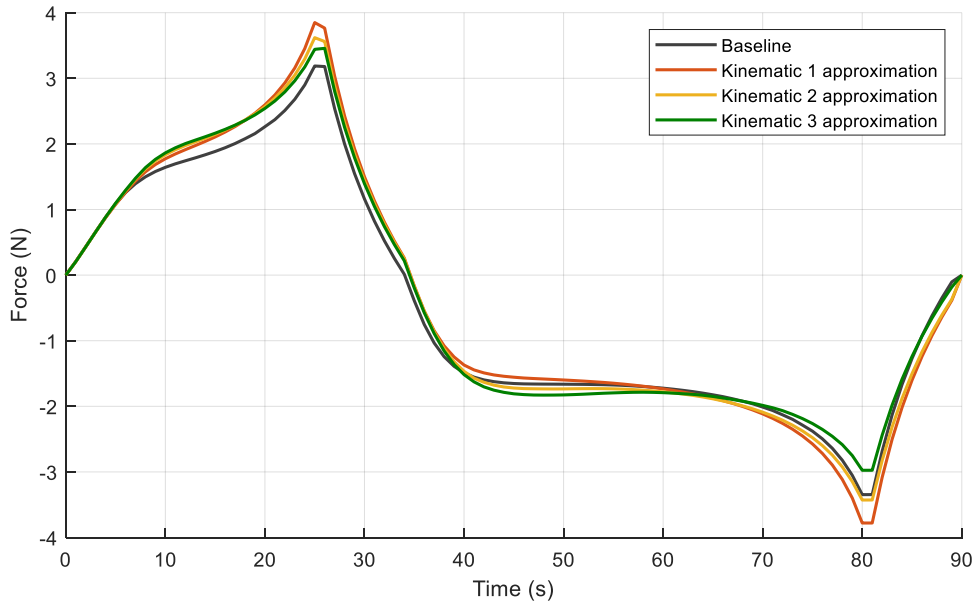

Figure 5-7 Force-time curve comparison, kinematic models vs baseline

Figure 5-7 shows that all kinematic approximations are able to model material behaviour before yielding well, but thereafter over-predict the forces required for forward bending. Kinematic 1 and 2 predict a higher maximum force for reverse bending while Kinematic 3 under-predicts the maximum force for reverse bending.

The high tangent modulus model Kinematic 1 has the largest percentage error value in Table 5-4. This is confirmed in Figure 5-7 where it is seen to be the most inaccurate model in terms of replicating the baseline bend test results.

The low tangent modulus model Kinematic 2 has a tangent modulus value of the same order as that of the isotropic material model. It can be seen to be fairly accurate at predicting material behaviour during reverse bending. The model is most inaccurate under forward bending conditions.

The elastic-perfect plastic model Kinematic 3 provides the most accurate approximation of all the kinematic models according to Table 5-4. Regarding specific portions of the bend curve, it can be seen to have the smallest error under conditions of forward bending and is the only model that under-predicts the maximum force during reverse bending.

5.4.7. Pull-out test on approximate models

The pull-out test was performed on hooked-end fibres with material models defined according to the parameters in Table 5-3. The predicted energy, first and second peak forces and percentage errors obtained using each model are given in Table 5-5 together with information corresponding to the baseline curve. Comparisons of the approximation model pull-out curves with the baseline curve are depicted in Figure 5-8 through Figure 5-11.

© University of Pretoria

Table 5-5 Energy, Force and Percentage Errors in Approximation: Pull-Out Test from Bend Test Parameters

	ISOTROPIC	KINEMATIC 1	KINEMATIC 2	KINEMATIC 3	BASELINE
Predicted energy (Nmm)	1756.47	1758.68	1838.80	1873.12	1769.79
Percentage error energy	0.75	0.63	3.90	5.84	N/A
Force 1st peak (N)	180.93	200.13	199.61	200.07	185.79
Percentage error 1st peak	2.62	7.72	7.44	7.69	N/A
Force 2nd peak (N)	108.85	111.5	115.06	116.95	109.11
Percentage error 2nd peak	0.24	2.18	5.43	7.15	N/A

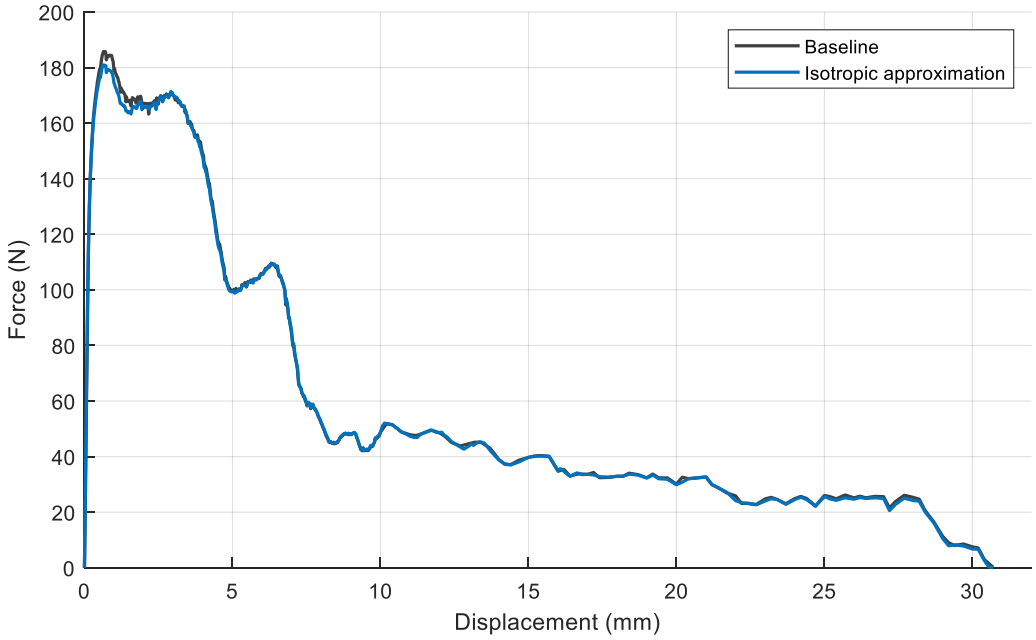

Figure 5-8 Pull-out test comparing isotropic model with baseline

The notion in Section 4.8.5 is confirmed with the bilinear isotropic approximation depicted in Figure 5-8 being the most accurate. The behaviour of the fibre during all stages of the pull-out test can be seen to be well approximated with most features of the baseline curve being matched by the approximation.

© University of Pretoria

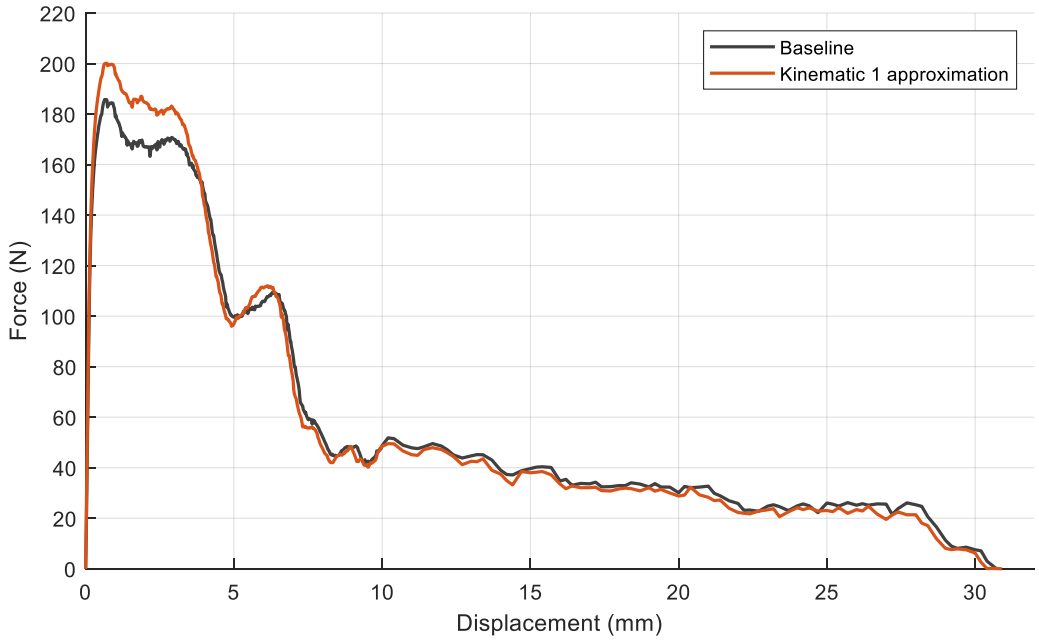

Figure 5-9 Pull-out test comparing Kinematic 1 model with baseline

The high tangent modulus model Kinematic 1 had the largest average error in approximating the baseline bend curve according to Table 5-4. However, according to Table 5-5, this approximation was the most accurate in terms of predicting the energy associated with pull-out and the maximum pull-out force at the second peak. Qualitatively, out of all of the kinematic approximations, this approximation resulted in the most accurate prediction of behaviour during pull-out.

It is noted that the percentage error associated with energy prediction given by the Kinematic 1 approximation in Figure 5-9 is less than that given by the isotropic approximation in Figure 5-8. It is however shown in Table 5-5 that the isotropic approximation has lower percentage errors associated with predicting the maximum pull-out force at the first and second peaks, thereby confirming the isotropic approximation as more accurate over-all.

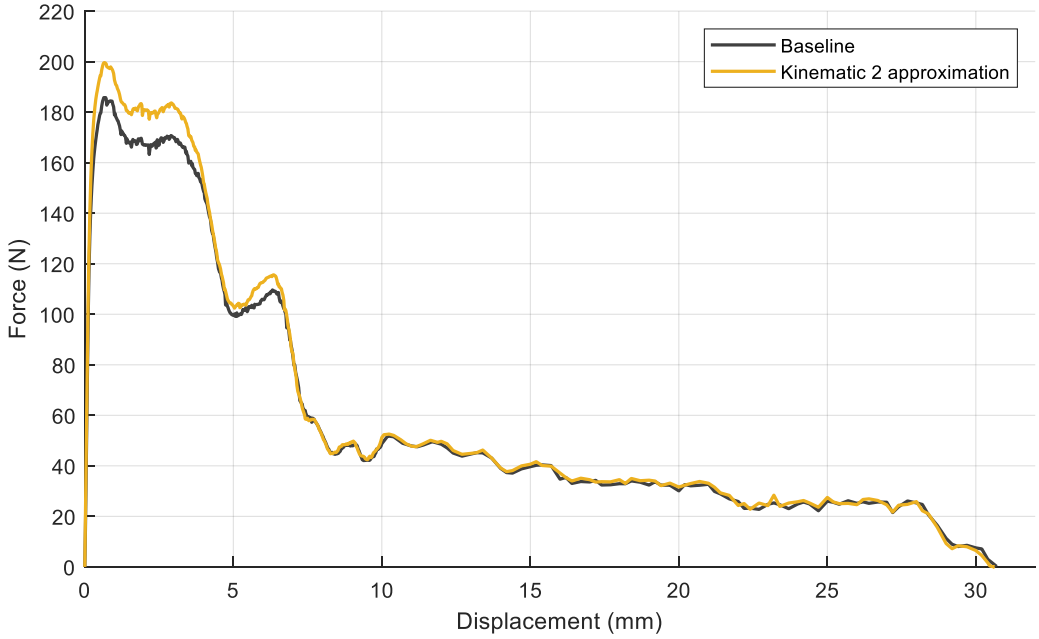

Figure 5-10 Pull-out test comparing Kinematic 2 model with baseline

© University of Pretoria

The low tangent modulus model Kinematic 2 depicted in Figure 5-10 was seen in Figure 5-7 to be the most accurate of the kinematic approximations at predicting behaviour during reverse bending. According to Table 5-5 this translated into the lowest error in approximating maximum pull-out force at the first peak and the second-lowest error for the second peak. Aside from over-predicting maximum pull-out force at the first and second peaks, this material model can be seen to provide a fairly accurate approximation of material behaviour during pull-out.

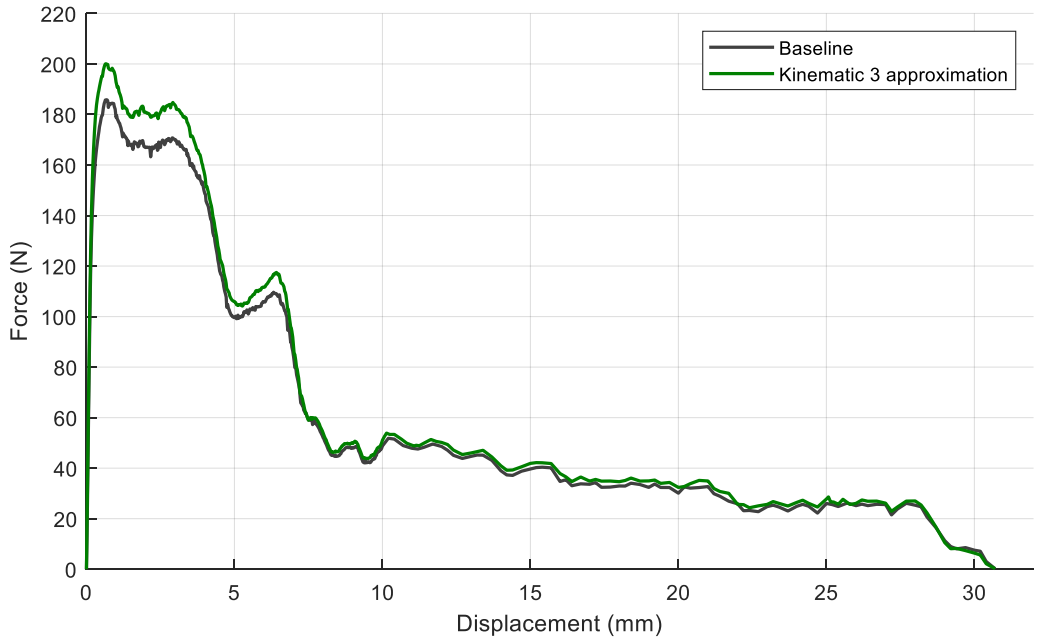

Figure 5-11 Pull-out test comparing Kinematic 3 model with baseline

The elastic-perfect plastic model Kinematic 3 depicted in Figure 5-11 was seen to be the most accurate kinematic approximation in terms of predicting behaviour during the bend test. According to Table 5-5, it can however be seen to be the least accurate model in terms of predicting total energy absorbed during pull-out with Figure 5-11 showing that this approximation consistently over-predicts the force at all stages of pull-out.

In Section 4.8.7, the elastic-perfect plastic kinematic approximation was predicted to be more accurate than the bilinear kinematic approximation. This was seen to not be the case and could indicate room for improvement in the generation of the surrogate surface for the kinematic material model.

5.5. CHARACTERISATION USING THE PULL-OUT TEST

In this section we will be examining the possibility of using the results of the simulated pull-out test on the as-drawn wire to estimate the starting material stress-strain curve. The force-displacement curve generated from the simulated pull-out test in Figure 4-20 was used as the baseline.

5.5.1. Design of experiments and numerical simulation

The same design of experiments was used as in Section 5.4.1, returning 50 sample points. Numerical simulation considered a series of pull-out tests identical to that detailed in Section 4.7 for bilinear material models defined by the 50 sample points. Two sets of studies were conducted, one using the isotropic material model, and one using the kinematic material model. Force results were extracted at 150 specific time values on each resulting force-displacement curve.

5.5.2. Construction of surrogate model

A surrogate surface was constructed to approximate the error between the numerical simulations performed in Section 5.5.1 and the baseline. Construction of the surface was performed in accordance with Section 5.4.3. One surrogate surface was created for the isotropic material model and one for the kinematic material model.

© University of Pretoria

5.5.3. Model validation and optimisation

The optimum value for ϵ was determined and the model was validated in accordance with Section 5.4.4. A total of 400 values of ϵ were evaluated in the domain 10^{-2} to 10^{2}. A value of $\epsilon = 1.78 \times 10^{-2}$ resulted in the lowest LOOCV error value for the isotropic model and $\epsilon = 2.45 \times 10^{-2}$ for the kinematic model.

The LOOCV error associated with different values for ϵ is depicted in Figure 5-12. The instability at ϵ values below 10^{-2} is clearly illustrated for both the kinematic and isotropic material models.

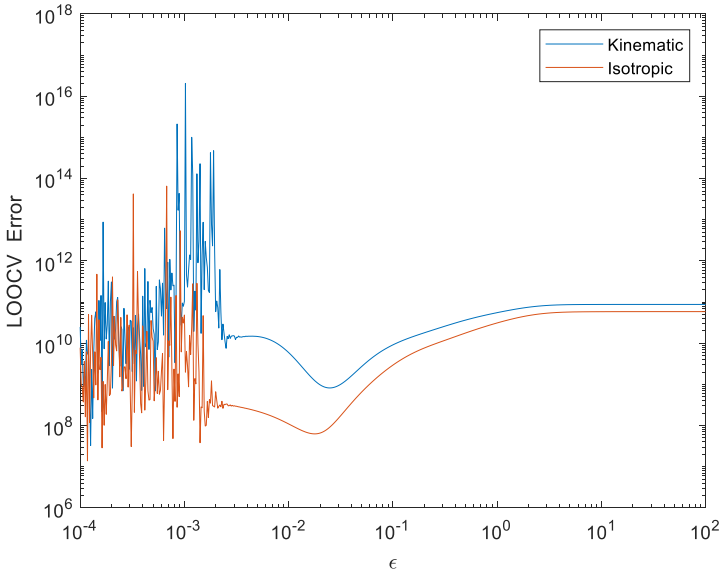

Figure 5-12 Surrogate surface LOOCV error associated with various values of ϵ for characterisation of material model using the pull-out test

Optimisation was performed in accordance with Section 5.4.5. Material parameters returned are given in Table 5-10.

Table 5-6 Material Parameters, Characterisation Using Simulated Pull-Out Curve

HARDENING LAW	YIELD STRENGTH (MPa)	TANGENT MODULUS (MPa)
Known solution	1087	489
Isotropic	1102	561
Kinematic	1126	435

5.5.4. Pull-out test on approximate models

The pull-out test was performed on hooked-end fibres with material models defined according to the parameters in Table 5-6. The predicted energy, first and second peak forces and percentage errors obtained using each model are given in Table 5-7 together with information corresponding to the baseline curve. Comparisons of the approximation model pull-out curves with the baseline curves are given in Figure 5-13.

Table 5-7 Energy, Force and Percentage Errors in Approximation: Pull-Out Test from Pull-Out Curve

	ISOTROPIC	KINEMATIC	BASELINE
Predicted energy (Nmm)	1787.53	1735.11	1769.79
Percentage error energy	1.00	1.96	N/A
Force 1st peak (N)	183.77	185.71	185.79
Percentage error 1st peak	1.09	0.04	N/A
Force 2nd peak (N)	111.81	108.59	109.11
Percentage error 2nd peak	2.47	0.48	N/A

© University of Pretoria

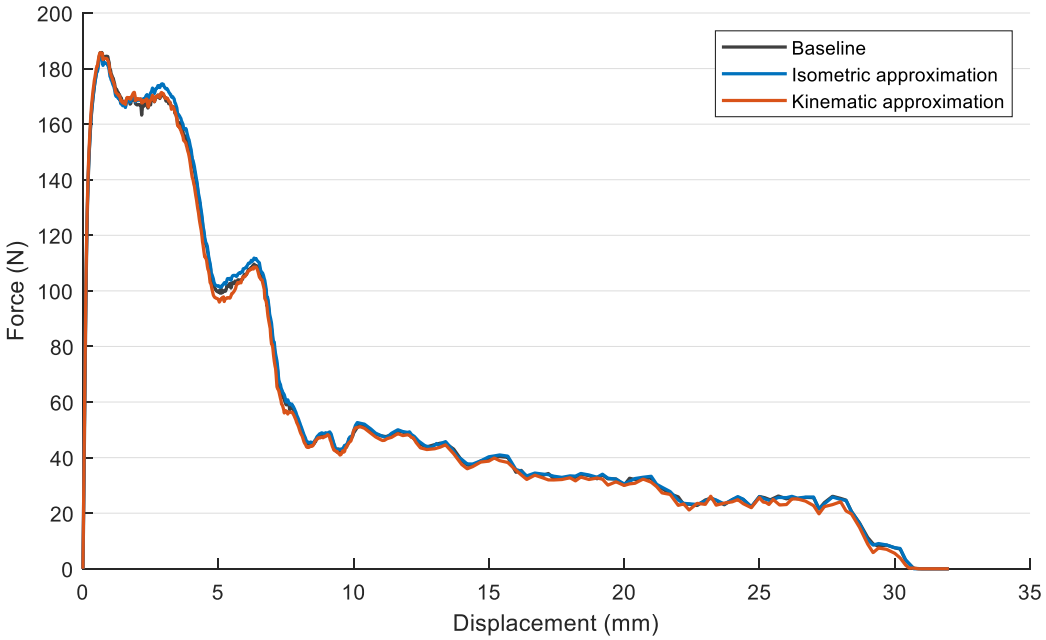

Figure 5-13 Pull-out test comparing material model characterised using the pull-out test

Figure 5-13 provides clear evidence of the fact that the material model may be accurately characterised using data from the pull-out test. The percentage errors on energy and force at the first and second peaks are all shown in Table 5-11 to be very low. The material model using the isotropic hardening law was seen to result in the lowest percentage error in terms of energy approximation, while the material model using the kinematic hardening law was seen to result in the lowest percentage errors for predicting maximum pull-out force at the first and second peaks. Once again, material behaviour during pull-out was shown to be insensitive to the hardening law.

5.6. CHARACTERISATION USING EXPERIMENTAL PULL-OUT CURVES

Section 5.5 demonstrated the sufficiency of the pull-out test for characterisation of the fibre material. In this section we will use an experimental pull-out curve to estimate the starting material stress-strain curve. The chosen curve is depicted in Figure 5-14 and corresponds to curve number S2T1 in Mpanga-A-Kangaj [8].

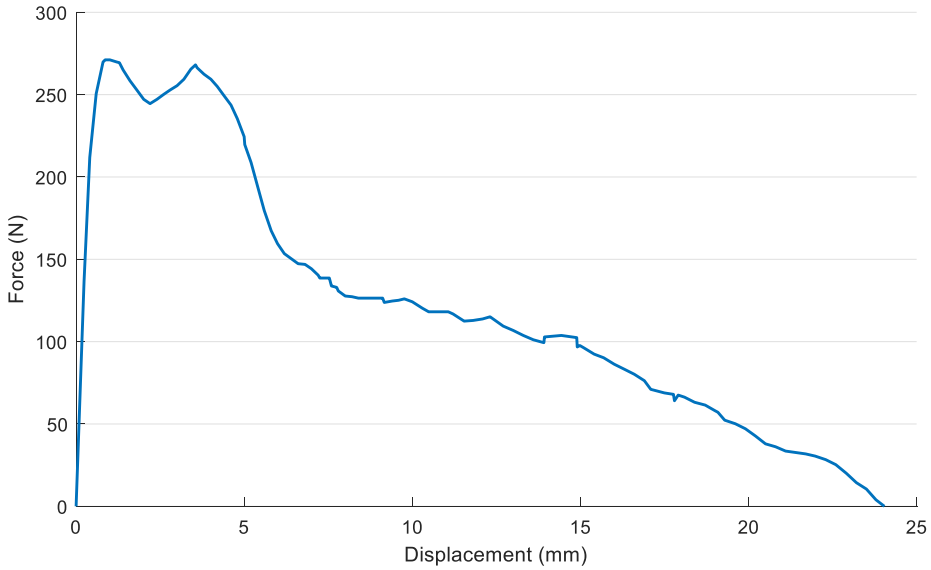

Figure 5-14 Experimental pull-out curves [8]

© University of Pretoria

There are significant differences between the experimental setup and the simulation used to estimate the fibre material model. Fibre geometry (diameter and shape of the hook), embedded length, surrounding material and coefficient of friction are all known to have a large effect on the shape of the pull-out curve and no attempt was made to alter the simulation to account for these differences beyond scaling of the curve as detailed in Section 5.6.3.

5.6.1. Design of experiments and numerical simulation

The same design of experiments was used as in Section 5.4.1, returning 50 sample points. Numerical simulation considered a series of pull-out tests identical to that detailed in Section 4.7 for bilinear material models defined by the 50 sample points. Two sets of studies were conducted, one using the isotropic material model, and one using the kinematic material model. Force results were extracted at 150 specific time values on each resulting force-displacement curve.

5.6.2. Construction of surrogate model

A surrogate surface was constructed to approximate the error between the numerical simulations performed in Section 5.6.1 and the baseline. Construction of the surface was performed in accordance with Section 5.4.3. One surrogate surface was created for the isotropic material model and one for the kinematic material model. The baseline experimental curve was determined according to Section 5.6.3.

5.6.3. Establishing the baseline

The experimental curve in Figure 5-14 was known to be generated by a fibre with a diameter ranging from 0.9 – 0.95 mm and an embedded length of 24 – 25 mm [8]. The fibres used for our study have a diameter of 0.8 mm and an embedded length of 32 mm.

From experimental studies performed by Abdallah et al. [72] the following empirical relationship was deduced for the effect of a change in diameter of the hooked-end fibre on pull-out energy:

$$\mathbb{E}_D = \left(\frac{D}{d}\right)^2 \mathbb{E}_d \tag{18}$$

where:

- $\mathbb{E}_D$ is the pull-out energy associated with the larger diameter fibre
- $\mathbb{E}_d$ is the pull-out energy associated with the smaller diameter fibre
- D is the diameter of the larger fibre
- d is the diameter of the smaller fibre

In the absence of further information, the diameter of the fibre used to generate the experimental curve in Figure 5-14 was assumed to be equal to 0.9 mm. Using equation (18), the values given in Table 5-8 were calculated for this diameter. From Table 5-8 we see that the energy associated with pull-out of the 0.9 mm fibre must be reduced by 21% in order to approximate the energy that would be associated with a 0.8 mm diameter fibre.

Table 5-8 Pull-Out Energy as Affected by Different Fibre Diameters Used in this Study

D (mm)	d (mm)	$\mathbb{E}_D$	$\mathbb{E}_d$
0.9	0.8	$1.266\mathbb{E}_d$	$0.790\mathbb{E}_D$

Since fibre diameter is also known to affect the magnitude of the peak loads [5], the reduction in energy was accomplished by scaling the force values by the factor of 0.790 given in Table 5-8. The effect of this scaling on the experimental curve is depicted in Figure 5-15.

© University of Pretoria

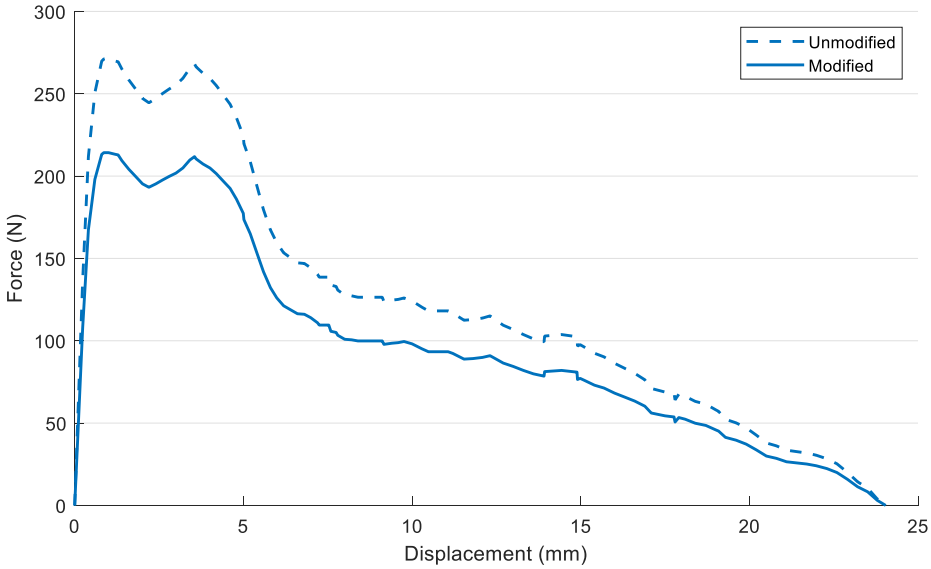

Figure 5-15 Illustration of energy scaling on two sets of experimental results

Figure 5-16 compares the experimental curve with a typical pull-out curve generated in the course of this study. It is clear that the second peak corresponding to plastic deformation of the last bend radius of the hooked-end was not captured by the experimental results. Also shown is the similarity between the shape of the first peak of the experimental curve, including the pseudo-peak, and that of the typical pull-out curve. It is therefore likely that a good approximation may be obtained for that portion of the experimental curve associated with plastic deformation of both bend radii of the hooked-end.

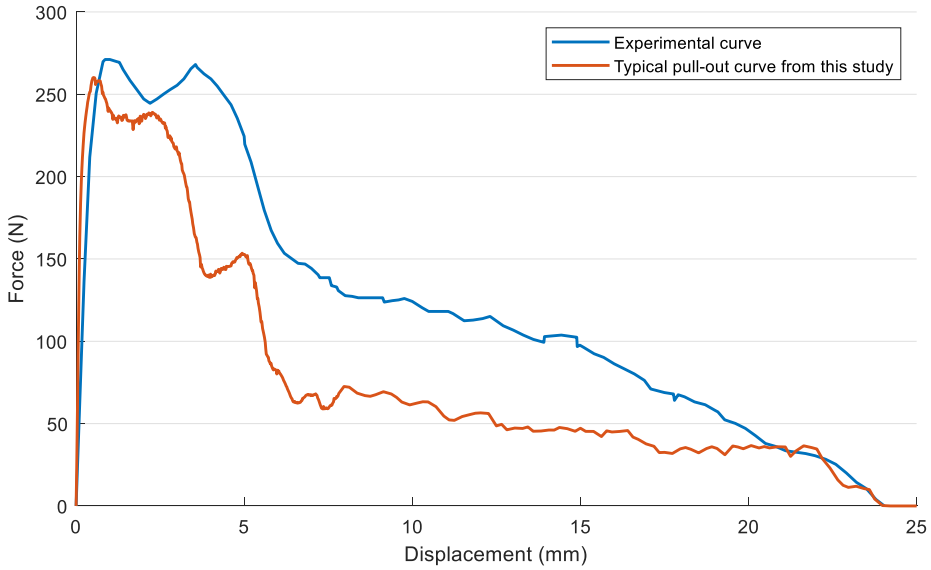

Figure 5-16 Comparison of experimental curve and typical pull-out curve

From Figure 5-16 we can see that plastic deformation of both bend radii continues until a displacement of 6.0 mm on the experimental pull-out curve and 4.8 mm on the typical pull-out curve. The first 6.0 mm of the experimental pull-out curve therefore needs to be scaled appropriately in order to establish a suitable baseline curve for use in constructing the surrogate surface.

Since this portion of the pull-out curve is associated with the geometry of the hooked-end, the first 6.0 mm of the experimental curve was scaled back to 4.8 mm in order to match the typical pull-out curve. This scaling can be seen in Figure 5-17.

© University of Pretoria

Figure 5-16 also shows a large difference in the force value at the start of frictional pull-out between the experimental curve and the typical pull-out curve. This indicates that a larger coefficient of friction exists in the experimental pull-out test than was used in the simulation. It is therefore clear that the simulated curves will not be able to approximate the experimental curve for the region of frictional pull-out unless a third variable is added to the material model – that of the coefficient of friction. This is a suggested topic for further study.

Figure 5-17 shows the portion of the experimental pull-out curve that will be used to train the surrogate surface. This portion corresponds to the plastic deformation of both bend radii of the hooked-end taking place over the first 4.8 mm of displacement. Since the surrogate surface is only trained using the first 4.8mm of the experimental curve, any prediction of the pull-out curve beyond this displacement cannot be expected to be accurate.

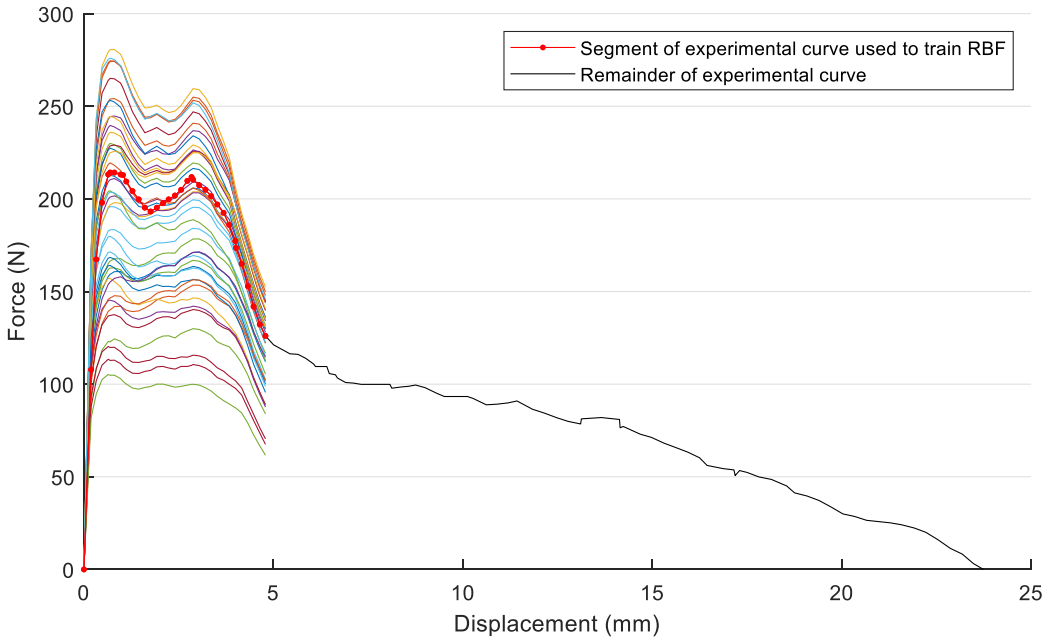

Figure 5-17 Segment of the experimental curve used to train the surrogate surface

Also shown in Figure 5-17 is the first 4.8 mm of the set of numerical simulation pull-out curves generated using the 50 sample points given by the design of experiments. Good correlation can be seen between the shape of these curves and the shape of that portion of the experimental curve used to train the surrogate surface.

5.6.4. Regarding embedded length

The relationship between the embedded length of a hooked-end fibre and pull-out energy has been shown to be linear with increasing embedded length [73]. For the case of equal coefficients of friction [5] the portion of the simulated curve associated with frictional pull-out may be scaled such that its associated pull-out energy is decreased by the ratio of the embedded length of the experimental fibre (24 mm) to the embedded length of the fibres used in the numerical simulations (32 mm).

5.6.5. Model validation and optimisation

The optimum value for ϵ was determined and the model was validated in accordance with Section 5.4.4. The domains for and optimal values of ϵ are given in Table 5-9 for the isotropic and kinematic material models. A minimum of 10000 points were considered in determining the LOOCV error.

Table 5-9 Domains and Optimal Values for ϵ, Characterisation Using Experimental Pull-Out Curve

ISOTROPIC		KINEMATIC	
DOMAIN	VALUE	DOMAIN	VALUE
10^{-2} to 10^{2}	0.0603	10^{-2} to 10^{2}	0.0245

© University of Pretoria

Optimisation was performed in accordance with Section 5.4.5. Material parameters returned are given in Table 5-10. It is interesting to note that both hardening laws in general returned material parameter values of approximately the same order.

Table 5-10 Material Parameters, Characterisation Using Experimental Pull-Out Curve

ISOTROPIC		KINEMATIC	
Yield strength (MPa)	Tangent modulus (MPa)	Yield strength (MPa)	Tangent modulus (MPa)
1341	743	1152	650
1252	1850		

5.6.6. Pull-out tests on approximate models

It is noted that obtaining a low error in terms of predicted energy is unrealistic since only the first 6.0 mm (scaled back to 4.8 mm) of the experimental curve was used to train the surrogate surface. A reasonably accurate prediction of maximum pull-out force at the first peak is however expected.

The pull-out test was performed on hooked-end fibres with material models defined according to the parameters in Table 5-10. The predicted energy, first peak force and percentage errors obtained using each model are given in Table 5-11 together with information corresponding to the experimental curve. Comparison of the approximation model pull-out curves with the experimental curve is given in Figure 5-18.

Table 5-11 Energy, Force and Percentage Errors in Approximation: Pull-Out Test from Experimental Curve

	PREDICTED ENERGY (Nmm)	PERCENTAGE ERROR ENERGY	FORCE 1st PEAK (N)	PERCENTAGE ERROR 1st PEAK
Experimental	2332.08	N/A	214.22	N/A
Isotropic 1	1661.63	28.75	211.21	1.41
Isotropic 2	1706.63	26.82	208.07	2.87
Kinematic	1463.18	37.26	189.52	11.53

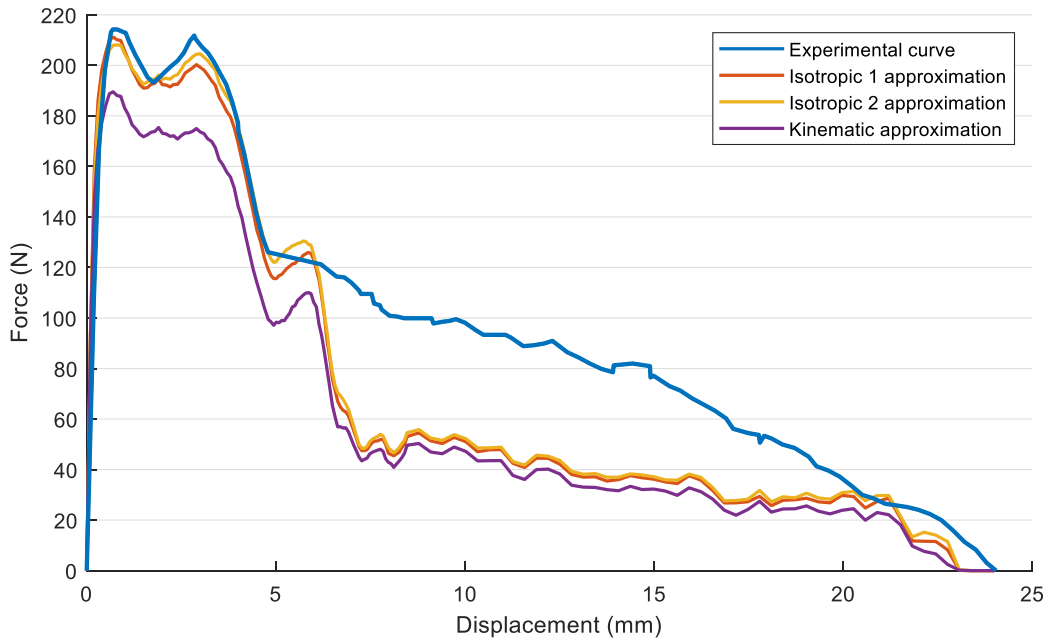

Figure 5-18 Comparison of pull-out curves from material characterised using experimental curve

The pull-out curves given by the isotropic approximations in Figure 5-18 can be seen to be the most accurate, corresponding to the lower percentage errors given in Table 5-11. The first 4.8 mm of the

© University of Pretoria

experimental curve can be seen to be well represented by the isotropic approximations. Failure of the kinematic approximation is likely due to an insufficiency in the surrogate model.

5.7. SUMMARY AND CONCLUSIONS

Results are summarised in Table 5-12 for the material models considered in Table 5-1, Table 5-3 and Table 5-6. Table 5-12 shows that characterisation using the pull-out test is able to provide the most accurate predictions for maximum pull-out force at the first and second peaks. Characterisation using the bend test is shown to be more accurate in terms of predicting the energy associated with pull-out. The tensile test is seen to be the least suitable for material characterisation. The percentage error on energy associated with the bilinear isotropic approximation created using the tensile test was 2.3 times higher than the percentage error associated with that of the bend test.

Table 5-12 Summary of Results

APPROXIMATION	PERCENTAGE ERROR IN APPROXIMATING BEND TEST	PERCENTAGE ERROR IN ENERGY APPROXIMATION	PERCENTAGE ERROR IN PREDICTING MAXIMUM PULL-OUT FORCE	
			First peak	Second peak
Pull-out Test Isotropic	N/A	1.00	1.09	2.47
Pull-out Test Kinematic	N/A	1.96	0.04	0.48
Bend Test Isotropic	0.70	0.75	2.62	0.24
Bend Test Kinematic 1	10.99	0.63	7.72	2.18
Bend Test Kinematic 2	8.65	3.90	7.44	5.43
Bend Test Kinematic 3	8.62	5.84	7.69	7.15
Tensile Bilinear Isotropic	N/A	1.78	4.81	1.03
Tensile Elastic- Perfect Plastic Isotropic	N/A	5.54	6.68	5.28
Tensile Elastic- Perfect Plastic Kinematic	N/A	5.54	6.68	5.28
Tensile Bilinear Kinematic	N/A	6.33	4.87	5.40

The fact that models defined using the isotropic hardening law were the most accurate is not surprising due to the fact that the isotropic hardening law was employed in the models used to obtain the baseline results. It is noted however, that a model using the kinematic hardening law may be found that produces results with the same order of error in all respects as that of the isotropic model.

For characterisation using the tensile test, the bilinear kinematic material model was shown to be the least accurate. This further serves to illustrate the usefulness of the pull-out and bend tests in characterising the material model since the actual hardening law for the material (isotropic, kinematic or combination thereof) will be unknown in practice.

It is therefore recommended that the starting material model to be used in the simulation and design of a steel-reinforcing fibre be determined as follows:

a) Perform a tensile test and calculate benchmark yield strength and tangent modulus values
b) Perform either a bend test or a pull-out test to determine the baseline curves
c) Perform a series of parametric studies for various hardening laws and values for yield strength and tangent modulus
d) Construct surrogate surfaces and optimise to obtain material properties. These properties should be of the same order as those calculated using the tensile test, though widely varying tangent modulus values should not be discarded
e) Test returned material properties by simulating the bend test or pull-out test and comparing the resulting curves to the baseline

© University of Pretoria

f) Create a bilinear material model based on the material properties corresponding to the most accurate approximation of the baseline curve

Further confirmation of the suitability of the use of the pull-out test for material characterisation was provided in Section 5.6 where an experimental pull-out curve was used as a baseline and surrogate surfaces constructed to estimate the error between the baseline and a set of simulated pull-out curves for the isotropic and kinematic hardening laws. Good correlation was achieved for the first 6.0 mm (scaled back to 4.8 mm) of pull-out despite significant differences between the experimental setup and the simulation.

© University of Pretoria

CHAPTER 6 - CONCLUSION

This study developed a theoretical material model based on information available to us from a real-world supplier of hooked-end steel fibres. Where information was lacking, the experience of other researchers in this field was drawn upon together with general information about the wire-drawing industry.

A reputable laboratory analysed a sample fibre acquired from a local manufacturer. Based on this information, we identified a plausible theoretical material model which we then submitted to a simulated wire-drawing process to arrive at a theoretical model of the as-drawn wire. Our confidence in this model is justified:

a) Simulated tensile tests agree substantially with the laboratory report and
b) The model's residual stress and equivalent plastic strain profiles conform substantially to real-world evidence in literature.

We identified a baseline model for pull-out tests as follows:

a) Determined force-displacement curves for our wire model in respect of each of the following:
    - Tensile test
    - Torsion test
    - Bend test
b) Simulated the hooked-end forming process
c) Simulated a pull-out test
d) Examined the contribution of the following, in combination and in isolation, to the results of the pull-out test
    - Residual stress profiles due to wire drawing
    - Plastic strain due to wire drawing
    - Stresses and plastic strains due to hooked-end forming
    - Coefficient of friction
    - Approximation of stress-strain curve using bilinear and elastic-perfect plastic models
    - Hardening law – isotropic and kinematic

And finally, with respect to the baseline model established above, we examined the possibility of predicting performance in a pull-out test by considering material models estimated using the following:

a) Results of a tensile test
b) Results of a simple bend test and
c) Results of a pull-out test

A summary of the errors between the baseline curves and the curves generated using the approximate material models in given in Table 6-1.

Table 6-1 Summary of Results from Approximate Models

APPROXIMATION	% ERROR IN BEND TEST APPROXIMATION	% ERROR IN ENERGY APPROXIMATION	QUALITATIVE ERROR IN PREDICTION
Pull-out Test Isotropic	N/A	1.0	Excellent
Pull-out Test Kinematic	N/A	1.96	Excellent
Bend Test Isotropic	0.70	0.75	Excellent
Bend Test Kinematic 1	10.99	0.63	Good
Bend Test Kinematic 2	8.65	3.90	Fair
Bend Test Kinematic 3	8.62	5.84	Fair
Tensile Bilinear Isotropic	N/A	1.78	Very good
Tensile Elastic- Perfect Plastic Isotropic	N/A	5.54	OK
Tensile Elastic- Perfect Plastic Kinematic	N/A	5.54	OK
Tensile Bilinear Kinematic	N/A	6.33	Good

© University of Pretoria

The results in Table 6-1 show that the material model characterised using the pull-out test is superior in terms of overall force prediction while the material model characterised using the bend test is superior in terms of predicting the pull-out energy. The bend test is seen to be able to provide more information for characterisation of the wire than the tensile test. The error associated with the tensile bilinear isotropic approximation was 2.3 times higher than the error associated with the bilinear isotropic approximation developed using the bend tests.

When the pull-out test was used to characterise the material, the percentage errors associated with both energy and maximum pull-out force were shown to be insensitive to the hardening law. When the bend test was used to characterise the material, the model returned for the kinematic hardening law was shown to produce the same order of error as the isotropic model in terms of energy absorbed during pull-out. This further serves to illustrate the value of the pull-out and bend tests since the actual hardening law for the material will be unknown in practice.

It is therefore recommended that the starting material model to be used in the simulation and design of a steel-reinforcing fibre be determined as follows:

a) Perform a tensile test and calculate benchmark yield strength and tangent modulus values
b) Perform a bend test to determine the baseline force-time curve
c) Perform a series of parametric studies for various hardening laws and values for yield strength and tangent modulus
d) Construct surrogate surfaces and optimise to obtain material properties. These properties should be of the same order as those calculated using the tensile test, though widely varying tangent modulus values should not be discarded
e) Test returned material properties by simulating the bend test and comparing the resulting force-time curves to the baseline
f) Create a bilinear material model based on the material properties corresponding to the most accurate approximation of the bend test force-time curve

Practical application of material characterisation using the pull-out test was demonstrated where a numerical simulation was able to provide a good approximation for the first 6.0 mm of an experimental pull-out curve despite significant differences between the simulation and experimental setups. The bilinear material model was shown to be able to predict the maximum pull-out force at the first peak with good accuracy.

Since only the first 6.0 mm of the experimental curve (scaled back to 4.8 mm to match the simulated pull-out curve) was used to train the surrogate surface, good approximation of the remainder of the curve associated with frictional pull-out could not be expected. This is due to the significant effect of the coefficient of friction on this region of the pull-out curve. A three-parameter model considering yield strength, tangent modulus and coefficient of friction would therefore be required in order to obtain an accurate approximation of an experimental pull-out curve. This is a suggested topic for further study.

© University of Pretoria

REFERENCES

[1] N. Subramanian, Design of Reinforced Concrete Structures: 1. Introduction to Reinforced Concrete, Oxford University Press, 2013.

[2] Stang, H.; Shah, S. P.;, "Failure of fibre-reinforced composites by pull-out fracture," *Journal of Materials Science,* vol. 21, pp. 953-957, 1986.

[3] A. Naaman, "Fiber reinforced concrete: Five decades of progress," in *BCCM4; 4th Brazilian Conference on Composite Materials, Rio de Janeiro, July 22nd-25th 2018*, Original source: Fiber reinforced cement and concrete composites; Florida, 2017.

[4] A. E. Naaman, "Engineered Steel Fibers with Optimal Properties for Reinforcement of Cement Composites," *Journal of Advanced Concrete Technology Vol 1. No 3,* pp. 241-252, 2003.

[5] J. Alwan, A. Naaman and W. Hansen, "Pull-out work of steel fibers from cementitious composites: Analytical investigation," *Cement & Concrete Composites 13,* pp. 247-255, 1991.

[6] J. M. Alwan, A. E. Naaman and P. Guerrero, "Effect of mechanical clamping on the pull-out response of hooked steel fibers embedded in cementitious matrices," *Concrete Science and Engineering Volume 1,* pp. 15-25, 1999.

[7] F. Laranjeira, C. Molins and A. Aguado, "Predicting the pullout response of inclined hooked steel fibers," *Cement and Concrete Research 40,* pp. 471-1487, 2010.

[8] C. Mpanga-A-Kangaj, "Pull-out of hooked end steel fibres: Experimental and numerical study," Faculty of Engineering, Build Environment and Information Technolology: University of Pretoria, 2013.

[9] S. Hamoush, T. Abu-Lebdeh, T. Cummins and B. Zornig, "Pullout Characterizations of Various Steel Fibers Embedded in Very High-Strength Concrete," *American Journal of Engineering and Applied Sciences, Volume 3,* pp. 418-426, 2010.

[10] M. A. Ulas, K. E. Alyamac and Z. C. Ulucan, "Effects of aggregate grading on the properties of steel fibre-reinforced concrete," 24 August 2019. [Online]. Available: https://www.researchgate.net/publication/320425332_Effects_of_aggregate_grading_on_the_properties_of_steel_fibre-reinforced_concrete.

[11] I. Markovich, J. van Mier and J. C. Walraven, "Single fiber pullout from hybrid fiber reinforced concrete," *HERON Volume 46, Number 3,,* pp. 191-200, 2001.

[12] G. E. Dieter, Mechanical Metallurgy, McGraw-Hill, 1961.

[13] V. N. Dankchenko, Metal forming, National Metallurgy Academy of Ukraine, 2007.

[14] R. N. Wright, Wire Technology: Process Engineering and Metallurgy; Second Edition, Elsevier Inc., 2016.

[15] K. Lange, Handbook of Metal forming; Society of Manufacturing Engineers; First Edition, McGraw-Hill, 1985.

[16] K. Osakada, "Effects of Strain Rate and Temperature in Forming Processes of Metals.," *Journal de Physique IV Colloque,* vol. 07, no. C3, pp. C3-XXXVII-C3-XLIV, 1997.

[17] J. M. Atienza, M. L. Matrinez-Perez, J. Ruiz-Hervias, F. Mompean, M. Garcia-Hernandez and M. Elices, "Residual stresses in cold drawn ferritic rods," *Scripta Materialia,* vol. 52, pp. 305-309, 2005.

[18] S. He, A. van Bael, S. Y. Li, P. van Houtte, F. Mei and A. Sarban, "Residual stress determination in cold drawn steel wire by FEM simulation and X-ray diffraction," *Materials Science and Engineering,* vol. A346, pp. 101-107, 2003.

[19] J. Toribio, J.-C. Matos, B. González and J. Escuadra, "Influence of Residual Stress Field on the Fatigue Crack Propagation in Prestressing Steel Wires," *Materials,* vol. 8, pp. 7589-7597, 2015.

[20] J. M. Atienza, J. Ruiz-Hervias and M. Elices, "The Role of Residual Stresses in the Performance and Durability of Prestressing Steel Wires," *Experimental Mechanics,* vol. 52, no. 7, pp. 881-893, 2012.

[21] R. Brighenti, A. Carpinteri and S. Vantadori, "Influence of Residual Stresses on Fatigue Crack Propagation in Pearlitic Cold-Drawn Steel Wires," *Materials Science Forum,* vol. 681, pp. 229-235, 2011.

[22] M. Elices, G. Maeder and V. Sánchez-Gálvez, "Effect of Surface Residual Stress on Hydrogen Embrittlement of Prestressing Steels," *British Corrosion Journal,* vol. 18, no. 2, pp. 80-81, 1983.

[23] C. a. E. E. Denise Brehm, "Cement's basic molecular structure finally decoded; September 9, 2009," 4 February 2019. [Online].

[24] C. Woodford, "Concrete and Reinforced Concrete; Last Updated October 31, 2018," 4 February 2019. [Online]. Available: https://www.explainthatstuff.com/steelconcrete.html.

[25] R. Collins, "People of Provence and France, Joseph Monier," 4 February 2019. [Online]. Available: http://www.beyond.fr/people/monier-joseph.html.

[26] "Joseph Monier, Last updated January 1, 2019," 4 February 2019. [Online].

[27] D. A. Fanella, Reinforced Concrete Structures: Analysis and Design, 2nd Edition; 1. Introduction and 2. Materials, McGraw-Hill Education, 2016.

[28] M. B. Muñoz, "Study of Bond Behaviour Between FRP Reinforcement and Concrete; 2.5 Literature Review Summary – Bond strength," Universitat de Girona, 2010.

[29] B. S. Choo, Advanced Concrete Technology; Institute of Concrete Technology; Volume 4: Processes; Part 10: Reinforced and Prestressed Concrete; Chapter 25: Reinforced and Prestressed Concrete, Elsevier Butterworth-Heinemann, 2003.

© University of Pretoria

[30] I. Löfgren, “Thesis for the Degree of Doctor of Philosophy: Fibre-reinforced concrete for industrial construction – a fracture mechanics approach to material testing and structural analysis,” 2005. [Online]. Available: http://publications.lib.chalmers.se/records/fulltext/8627/8627.pdf.

[31] D. Hannant, Advanced Concrete Technology; Institute of Concrete Technology; Volume 4: Processes; Part 2: Special Concretes; Chapter 6: Fibre-reinforced Concrete, Elsevier Butterworth-Heinemann, 2003.

[32] FIBSOL, “Steel Reinforcing Fibres,” 4 February 2019. [Online]. Available: fibsol.co.za.

[33] ACI Committee 544, “ACI 544.1R-96 State-of-the-art Report on Fiber Reinforced Concrete,” American Concrete Institute, 1996, Reapproved 2002.

[34] American Society for Testing and Materials, “ASTM A820/A820M-16 Standard Specification for Steel Fibers for Fiber-Reinforced Concrete,” ASTM International, 2016.

[35] British Standards, “BS EN 14889-1:2006 Fibres for concrete – Part 1: Steel fibres – definitions, specifications and conformity,” British Standards Institute, 2006.

[36] ArcelorMittal, “Wire Solutions, Steel Fibres, Products,” 16 February 2019. [Online]. Available: http://ds.arcelormittal.com/wiresolutions/steelfibres/products/language/EN.

[37] M. M, “Steel Fibers and Rebar; Last updated December 9, 2015,” 4 February 2019. [Online]. Available: http://www.concretefibersolutions.com/2015/12/09/steel-fibers-and-rebar/.

[38] ArcelorMittal, “Wire Solutions, Steel Fibres: Housing applications,” 16 February 2019. [Online]. Available: http://ds.arcelormittal.com/repository/fanny/Housing_EN.pdf 2015.

[39] ArcelorMittal, “Wire Solutions, Steel Fibres: Structural applications,” 16 February 2019. [Online]. Available: http://ds.arcelormittal.com/repository/fanny/Structural-EN.pdf.

[40] American Concrete Institute, “ACI 318-14 Building Code Requirements for Structural Concrete (ACI 318-14) and Commentary on Building Code Requirements for Structural Concrete (ACI 318-R-14); R9.6.3 Minimum shear reinforcement,” American Concrete Institute, 2014.

[41] The South African Bureau of Standards, “SABS 0100-1*, Edition 2.2: South African Standard Code of Practice; The structural use of concrete, Part 1: Design,” The South African Bureau of Standards, 2000.

[42] South African National Standard, “SANS 10100-2:2014, Edition 3: The structural use of concrete, Part 2: Materials and execution of work,” SABS Standards Division, 2014.

[43] South African National Standard, “SANS 10144:2012, Edition 2: Detailing of steel reinforcement for concrete,” SABS Standards Division, 2012.

[44] The International Federation for Structural Concrete (fib), “fib Model Code for Concrete Structures 2010,” Ernst & Sohn, 2013.

[45] N. Görander and C. Halldén, “Master’s Thesis: Crack width profiles for fibre-reinforced concrete elements with conventional reinforcement,” 2015. [Online]. Available: http://publications.lib.chalmers.se/records/fulltext/219358/219358.pdf.

[46] A. Pompo, P. R. Stupak, L. Nicolais and B. Marchese, “Analysis of steel fibre pull-out from a cement matrix using video photography,” *Cement and Concrete Composites; Volume 18,* pp. 3 - 8, 1996.

[47] A. Phelippeau, S. Pommier, T. Tsakalakos, M. Clavel and C. Prioul, “Cold drawn steel wires – processing, residual stresses and ductility – part I: metallography and finite element analyses,” *Fatigue and Fracture of Engineering Materials and Structures,* vol. 29, pp. 243-253, 2005.

[48] J. Toribio, M. Lorenzo, D. Vergara and V. Kharin, “Effects of manufacturing-induced residual stresses and strains on hydrogen embrittlement of cold drawn steels,” *Procedia Engineering,* vol. 10, pp. 3540-3545, 2011.

[49] U. Prisco, “Strain Hardening of Carbon Steel during Wire Drawing,” *Materials Research,* vol. 21, no. 3, 2018.

[50] Hyperion Materials and Technologies, “Toolmaker Solutions: Wire Drawing Guide TS-WD 1809-001,” 2018. [Online]. Available: www.HyperionMT.com. [Accessed 19 May 2019].

[51] S. Kok, “MEE 732: Small strain plasticity class notes for Advanced Finite Element Methods course MEE 781 taken in 2015,” University of Pretoria, 2005.

[52] W. D. Callister, Jr., Materials Science and Engineering, an Introduction, Seventh Edition, Wiley, 2007.

[53] ANSYS, Inc., “ANSYS Training manual: Chapter Three: Rate-Independent Plasticity; Inventory #001491 3-2,” September 2001. [Online]. Available: https://slideplayer.com/slide/9509075/. [Accessed 17 August 2019].

[54] S. Imaoka, “Sheldon’s ANSYS tips and tricks: Plasticity hardening rules; Memo number: STI:01/11,” ANSYS, 2001.

[55] ANSYS, Inc., “Mechanical APDL 2019 R2 – Material Reference Chapter 4: Nonlinear Material Properties – 4.4 Rate Independent Plasticity,” 2019.

[56] U. F. Kocks, Texture and Anisotropy Chapter 8: Kinematics and Kinetics of Plasticity, Cambridge University Press, 1998.

[57] S. Kok, A. J. Beaudoin and D. A. Tortorelli, “On the development of stage IV hardening using a model based on the mechanical threshold,” *Acta Materialia,* vol. 50, pp. 1653-1667, 2002.

[58] S. Kok and D. N. Wilke, “Estimating the stress-strain curve of steel wire,” *Engineering Optimization,* vol. IV, pp. 1011-1016, 2015.

[59] A. D. Rollett and U. F. Kocks, “A review of the stages of work hardening,” Los Alamos National Laboratory, [Online]. Available: https://www.osti.gov/servlets/purl/10170133. [Accessed 24 August 2019].

© University of Pretoria

[60] L. M. Brown, “Dislocation plasticity in persistent slip bands,” *Materials Science and Engineering: A,* vol. 285, no. 1-2, pp. 35-42, 2000.

[61] N. E. Dowling, Mechanical Behaviour of Materials: Engineering Methods for Deformation, Fracture, and Fatigue; Fourth Edition; Chapter 12: Plastic deformation behaviour and models for materials, Pearson, 2013.

[62] Matweb, “Material Property Data,” [Online]. Available: Matweb Material property data; http://www.matweb.com/search/DataSheet.aspx?MatGUID=07f46bb58c374eaeb6eb8cefc486404f. [Accessed 25 August 2019].

[63] CAEAI, “Tips and tricks for modeling plasticity,” [Online]. Available: https://caeai.com/resources/tips-tricks-modeling-plasticity-ansys-e-learning. [Accessed 21 July 2019].

[64] ANSYS, Inc., “ANSYS Workbench 2019 R2; Engineering Data Sources; Granta Design Sample Materials; Tungsten carbide,” Granta Design, 2019.

[65] K. R. Yoshida, R. Ido and T. Denshi, “Effects of Back Tension and Drawing Direction on Wire Properties in Copper Wire Drawing,” in *71st Wire & Cable Technical Symposium*, Atlanta, 2001.

[66] API/ASME, “Table 4.1 Carbon Steel UTS ≤ 414MPa,” in *API-579/ASME FFS-1: Fitness-For-Service; 2nd Edition*, The American Society of Mechanical Engineers and American Petroleum Institute, 2016.

[67] National Institute of Standards and Technology, “NIST Technical Note 1907: Temperature-Dependent Material Modelling for Structural Steels: Formulation and Application,” April 2016. [Online]. Available: http://dx.doi.org/10.6028/NIST.TN.1907. [Accessed 4 July 2019].

[68] S. He, P. Van Houtte, A. Van Bael, F. Mei, A. Sarban, P. Boesman, F. Galvez and J. M. Atienza, “Strain rate effect in high-speed wire drawing process,” *Modelling and Simulation in Materials Science and Engineering,* vol. 10, pp. 267-276, 2002.

[69] ASTM, “ASTM F1622-95 Standard Test ethod for Measuring the Torsional Properties of Metallic Bone Screws,” ASTM International, 1995 Reapproved 2000.

[70] ANSYS, Inc., “ANSYS Workbench 2019 R3; Engineering Data Sources; General Non-linear Materials; Concrete NL,” 2019.

[71] A. Khbaz, “Determination of Friction Coefficient Between Straight Steel Fiber and the Concrete Fri (SSF.C),” *Advances in Materials,* vol. 4, no. 2, pp. 20 - 29, 2015.

[72] S. Abdallah, M. Fan and X. Zhou, “Pull-Out Behaviour of Hooked End Steel Fibres Embedded in Ultra-high Performance Mortar with Various W/B Ratios,” *International Journal of Concrete Structures and Materials,* vol. 11, no. 2, pp. 301-313, 2017.

[73] F. Deng, X. Ding, Y. Chi, L. Xu and L. Wang, “The pull-out behavior of straight and hooked-end steel fiber from hybrid fiber reinforced cementitious composite: Experimental study and analytical modelling,” *Composite Structures,* vol. 206, pp. 693-712, 218.

[74] N. V. Quipo, R. T. Haftka, W. Shyy, T. Goel, R. Vaidyanathan and P. K. Tucker, “Surrogate-based Analysis and Optimization,” University of Florida, Department of Mechanical and Aerospace Engineering.

[75] D. N. Wilke, “Primer on response surfaces (surrogates),” University of Pretoria, 2016.

© University of Pretoria

APPENDIX A. SIMULATING THE WIRE-DRAWING PROCESS

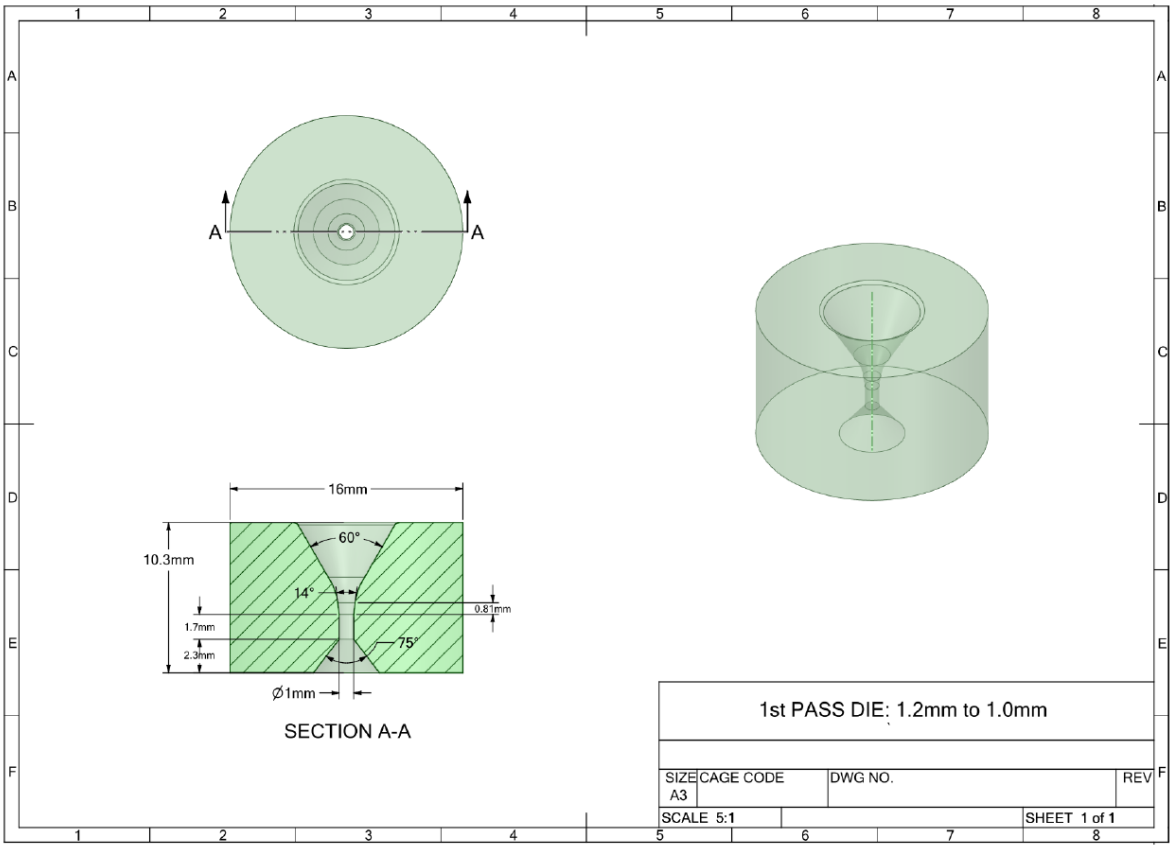

Figure A-1 First-pass die

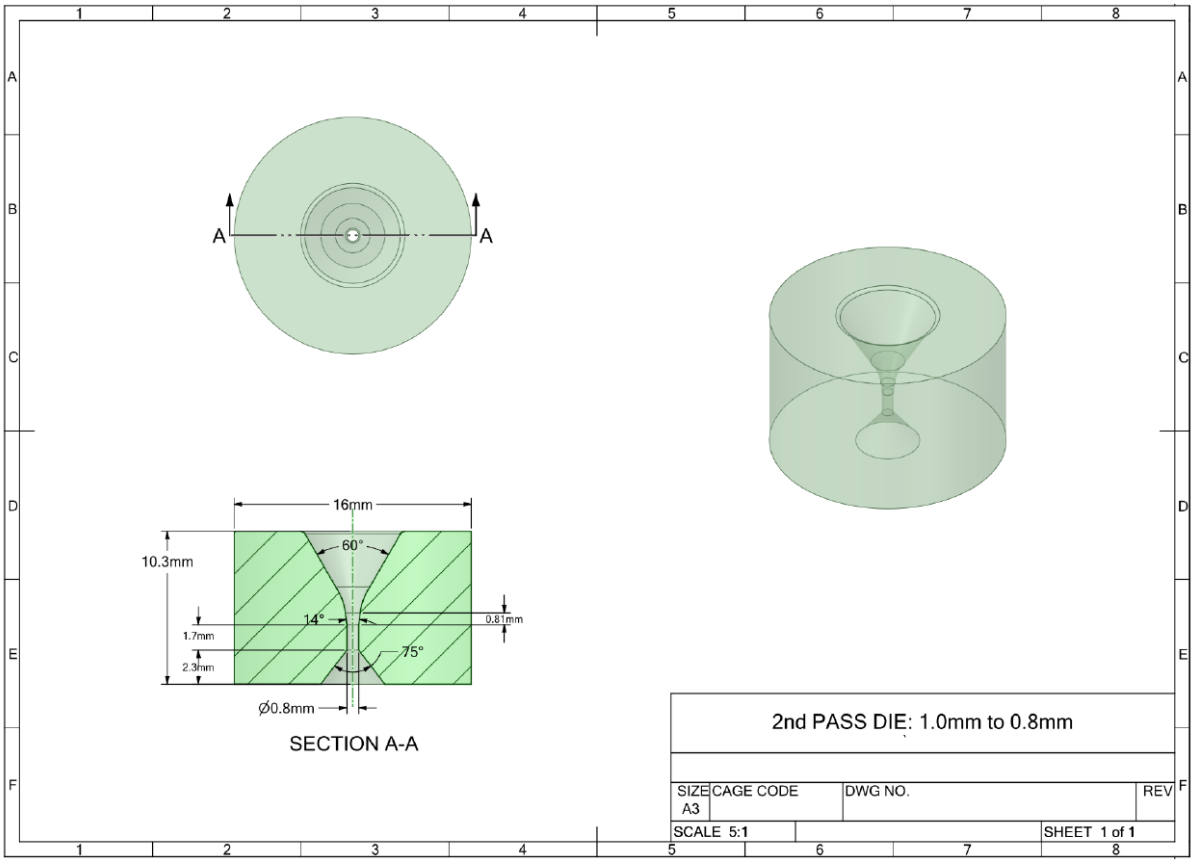

Figure A-2 Second-pass die

© University of Pretoria

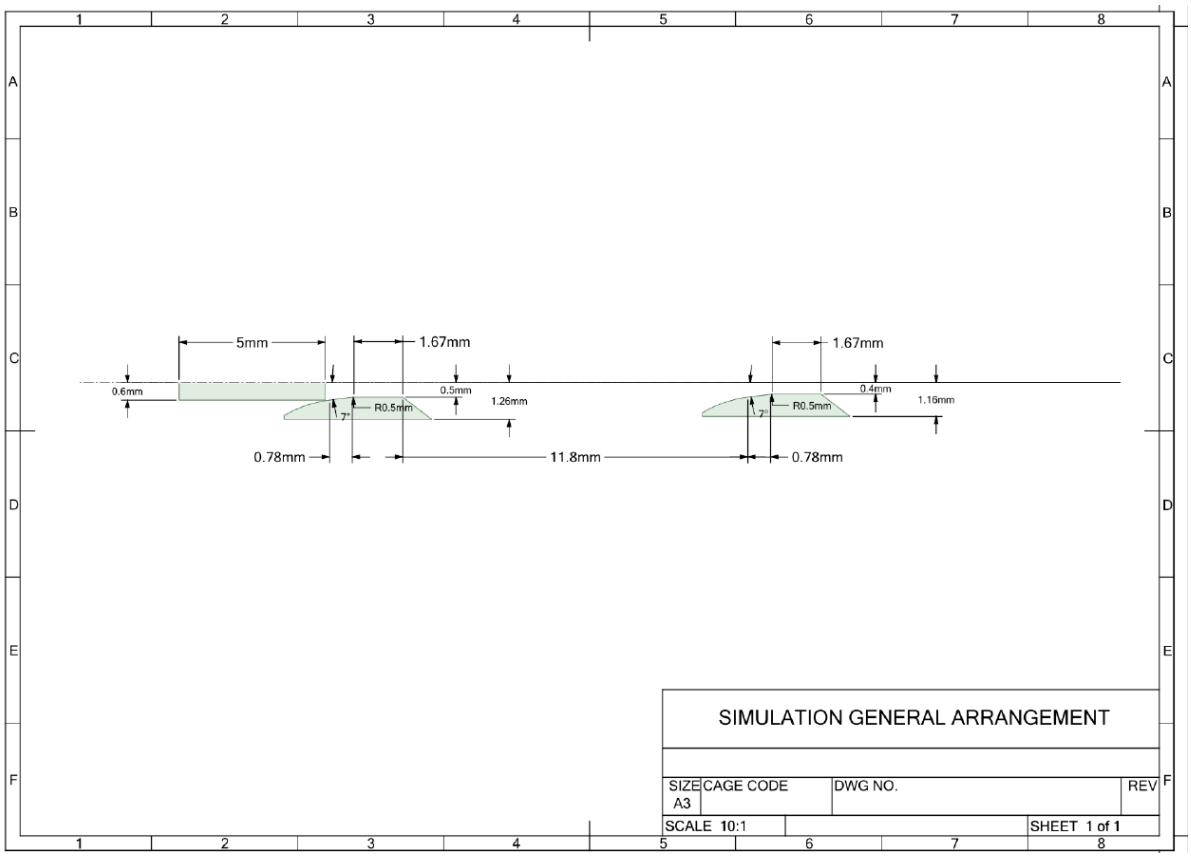

Figure A-3 Simulation general arrangement

Table A-1 Laboratory Report for Sample Hooked-End Fibres

#	DIA. mm	AREA mm^2	GUAGE 5.56V±5mm mm	YIELD 0.2% LOAD N	MAX LOAD N	EXTENSION mm	YIELD 0.2% STRESS MPa	UTS MPa	ELONGATION 5.56V±5mm %
1	0.80	0.50	10.00	630	786	0.3	1267	1563	3
2	0.80	0.50	10.00	800	818	0.2	1604	1626	2
3	0.80	0.50	10.00	580	764	0.3	1159	1520	3

Tested by Scrooby's Laboratory Service CC In accordance with SANS 6892-1:2010/ISO 6892-1:2009

© University of Pretoria

Distribution Solutions
WireSolutions

ArcelorMittal

Technical data sheet
Hooked-end steel fibres

HE 90/60

Dimensions	
Wire diameter (d)	0.90 mm (± 0.04 mm)
Fibre length (L)	60.0 mm (+2/-3 mm)
Hook length (l and l')	1 – 4
Hook depth (h and h')	1.80 mm (+1/-0 mm)
Bending angle (α and α')	45° (min. 30°)
Aspect ratio (L/d)	67
Camber of the fibre	max. 5% of L'
Torsion angle of the fibre	< 30°
Number of fibres per kg	3200
Total fibre length per 10 kg	1920 m

Packaging	
Recyclable cardboard boxes	
Net weight/box	25 kg
Boxes/palette	48
Weight/palette	1200 kg
The fibres are oriented in one direction	
Palettes are wrapped or welded in a plastic folio	
Available also in big bag of 500 kg	

Miscellaneous

The described fibre is in accordance with the following standards:

- EN 14889-1 type 1 (cold-drawn wire),
- ASTM A820/A820M-04 type 1 (cold-drawn wire).

Material characteristics

- Tensile strength of drawn wire 1200 N/mm²

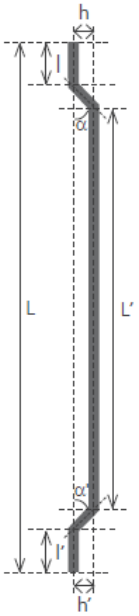

All information in this promotional material illustrates products and services in a non final way and invites further technical or commercial explanation. This is not contractual. Copyright ArcelorMittal – June 2011.

ArcelorMittal Bissen & Bettembourg
Route de Finsterthal - PO Box 16
L-7703 Bissen
T +352 83 57 72 1
F +352 83 56 98
www.arcelormittal.com/steelfibres

Figure A-4 Data sheet, sample fibre

© University of Pretoria

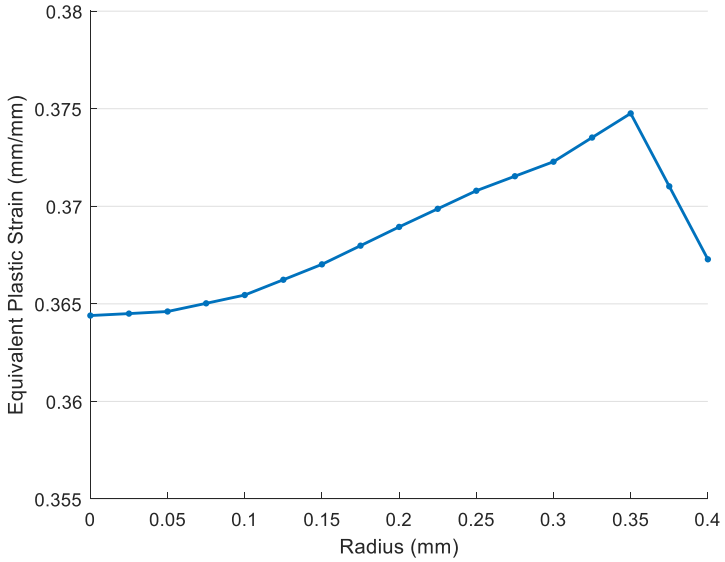

Figure A-5 First pass equivalent plastic strain

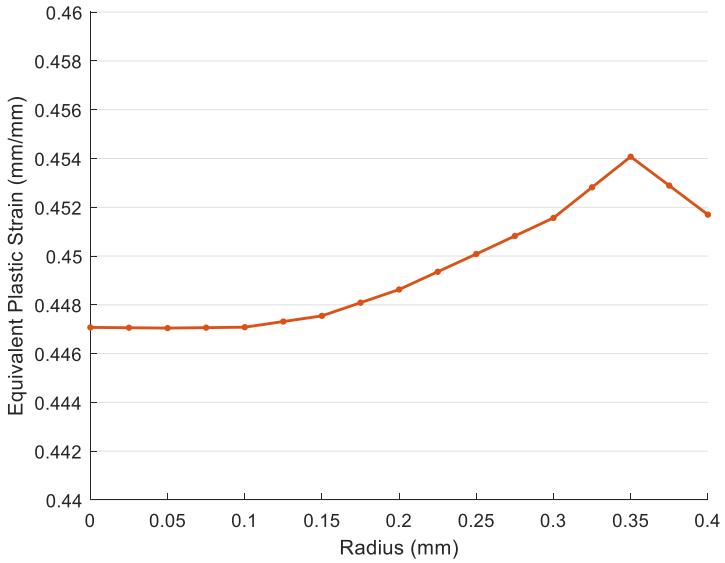

Figure A-6 Second pass equivalent plastic strain

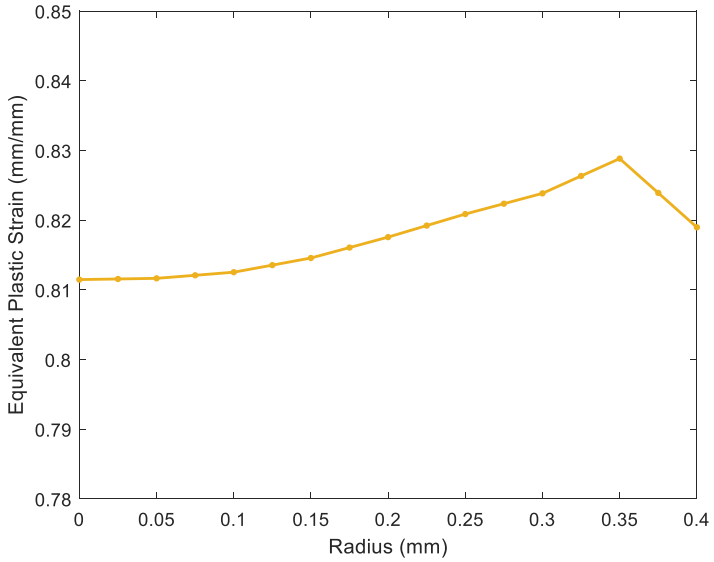

Figure A-7 Total equivalent plastic strain in the simulated as-drawn wire

© University of Pretoria

APPENDIX B. BASELINE RESULTS

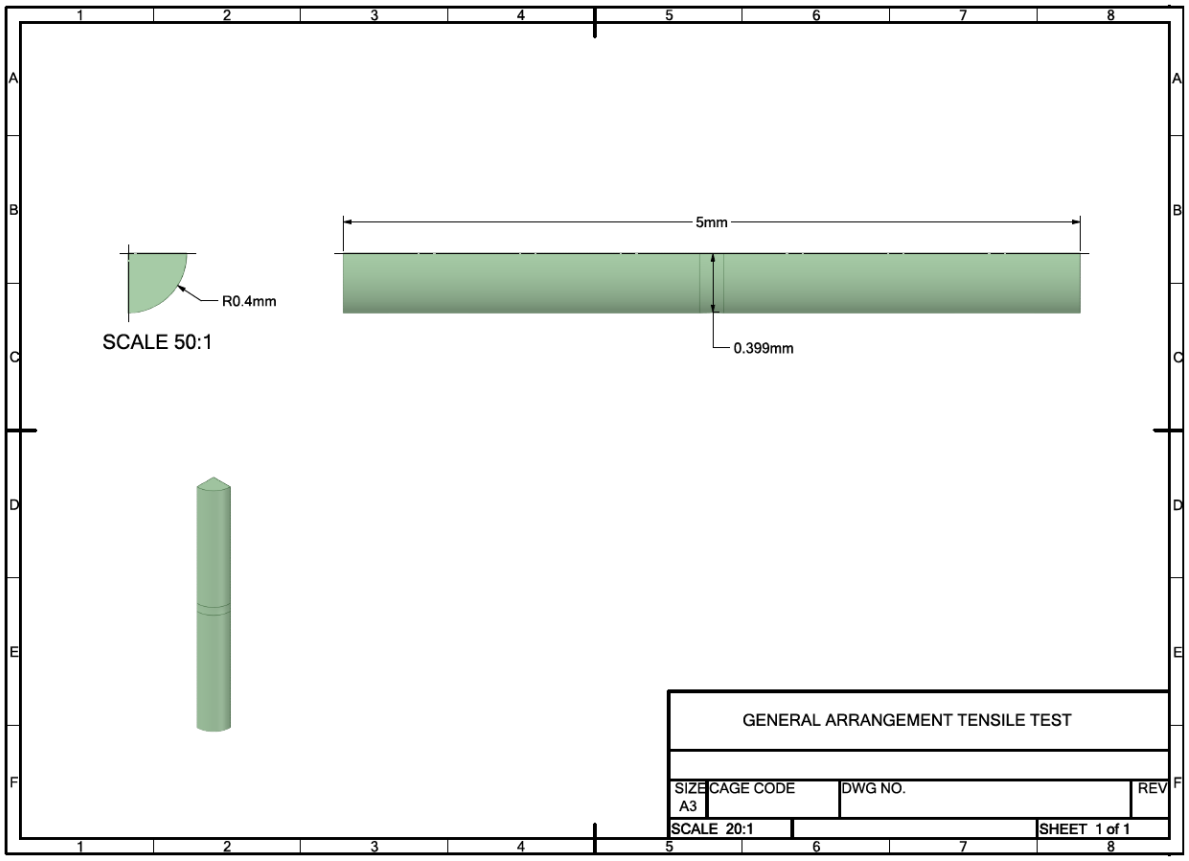

Figure B-1 General arrangement, tensile test

B.1 Mesh convergence for tensile test

The convergence study was performed for a mesh size of 0.1mm and 0.05mm. This resulted in a 460% increase in the number of nodes and elements. The average error between the force-displacement curves was calculated as follows:

$$average\ error = \frac{\sum \frac{\|F_{0.05} - F_{0.1}\|}{F_{0.05}}}{n_p} \tag{19}$$

where n_p is the number of points used to generate the force-displacement curve.

When converted to a percentage, the average error between results obtained using a mesh size of 0.1mm and results obtained using a mesh size of 0.05mm was calculated to be equal to 1.20%. Results for the tension test were therefore considered to have converged at a mesh size of 0.05mm.

© University of Pretoria

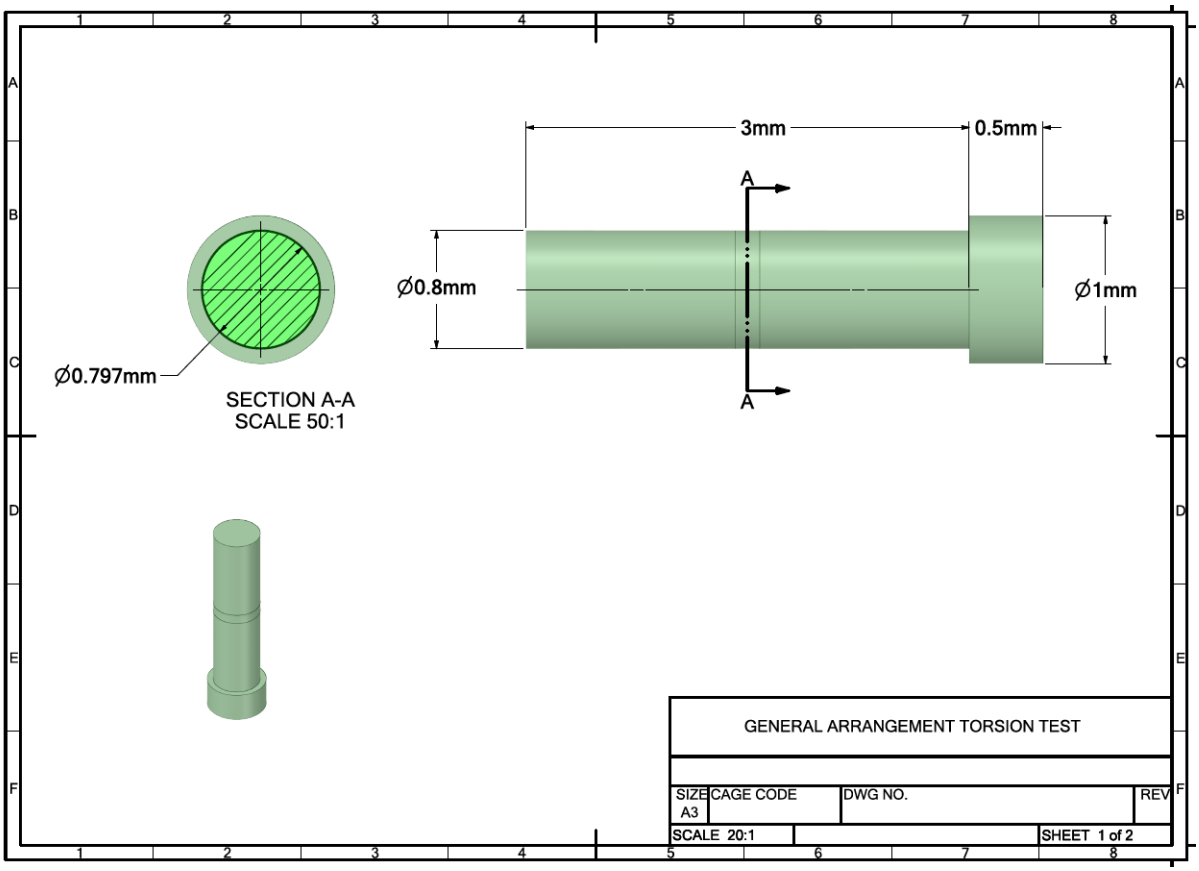

Figure B-2 General arrangement, torsion test

B.2 Mesh convergence for torsion test

The convergence study was performed for a mesh size of 0.1mm and 0.07mm. This resulted in a 260% increase in the number of nodes and elements. The average error between the torque-twist curves was calculated as follows:

$$average\ error = \frac{\sum \left\| \frac{T_{0.07} - T_{0.1}}{T_{0.07}} \right\|}{n_p} \tag{20}$$

where n_p is the number of points used to generate the torque-twist curve.

When converted to a percentage, the average error between results obtained using a mesh size of 0.1mm and results obtained using a mesh size of 0.07mm was calculated to be equal to 0.05%. Results for the tension test were therefore considered to have converged at a mesh size of 0.07mm.

© University of Pretoria

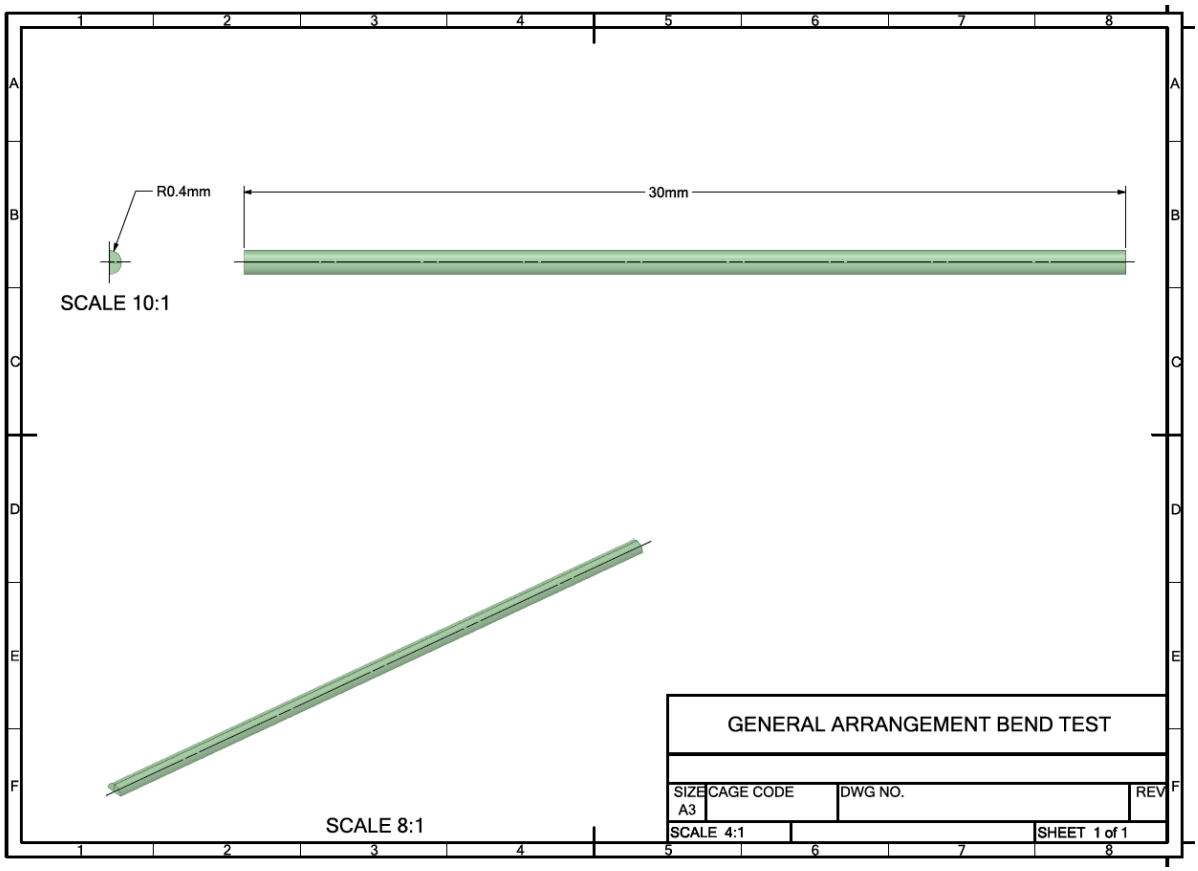

Figure B-3 General arrangement, bend test

B.3 Mesh convergence for bend test

The convergence study was performed for a mesh size of 0.15mm and 0.1mm. This resulted in a 60% increase in the number of nodes and elements. The average error between the force-displacement curves was calculated as follows:

$$average\ error = \frac{\sum \left\| \frac{F_{0.1} - F_{0.15}}{F_{0.1}} \right\|}{n_p} \tag{21}$$

where n_p is the number of points used to generate the force-displacement curve.

When converted to a percentage, the average error between results obtained using a mesh size of 0.15mm and results obtained using a mesh size of 0.1mm was calculated to be equal to 2.3%. Results for the bend test were therefore considered to have converged at a mesh size of 0.1mm.

© University of Pretoria

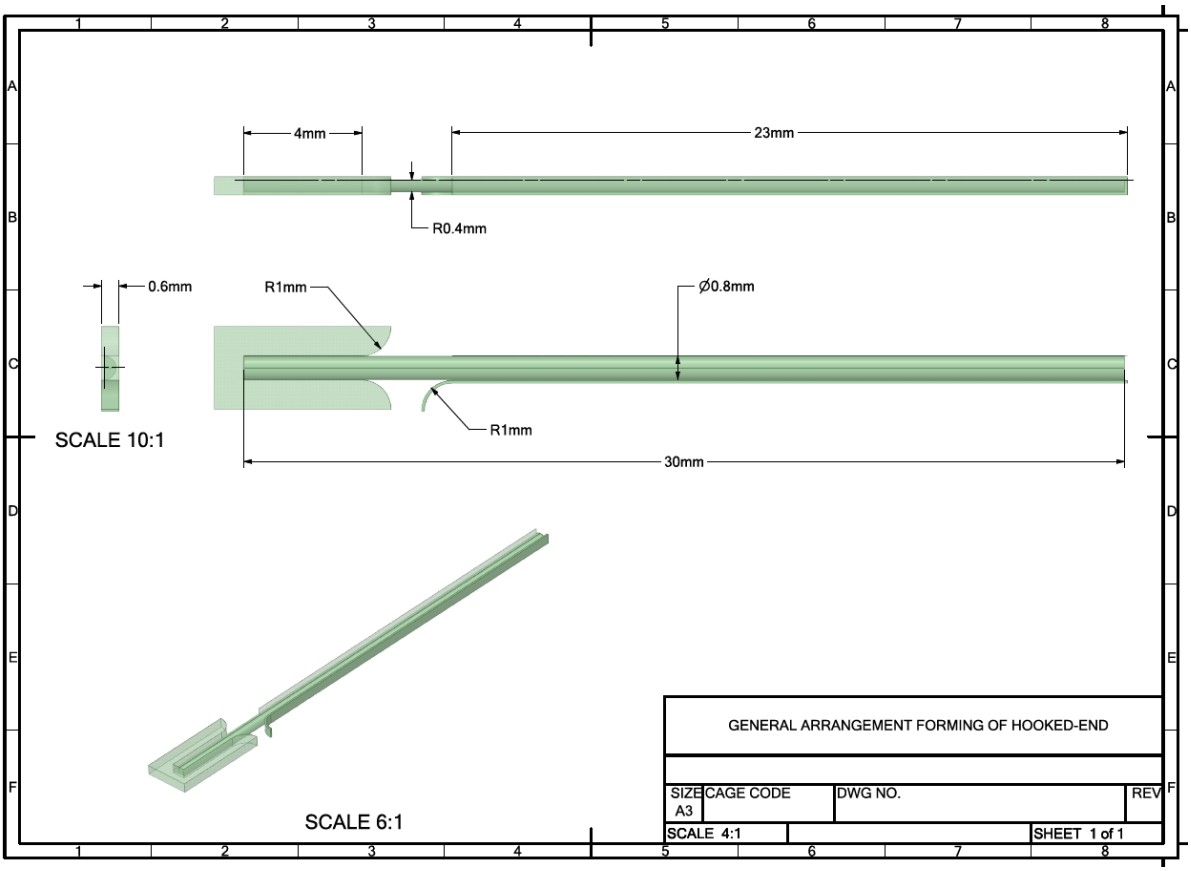

Figure B-4 General arrangement, forming hooked ends

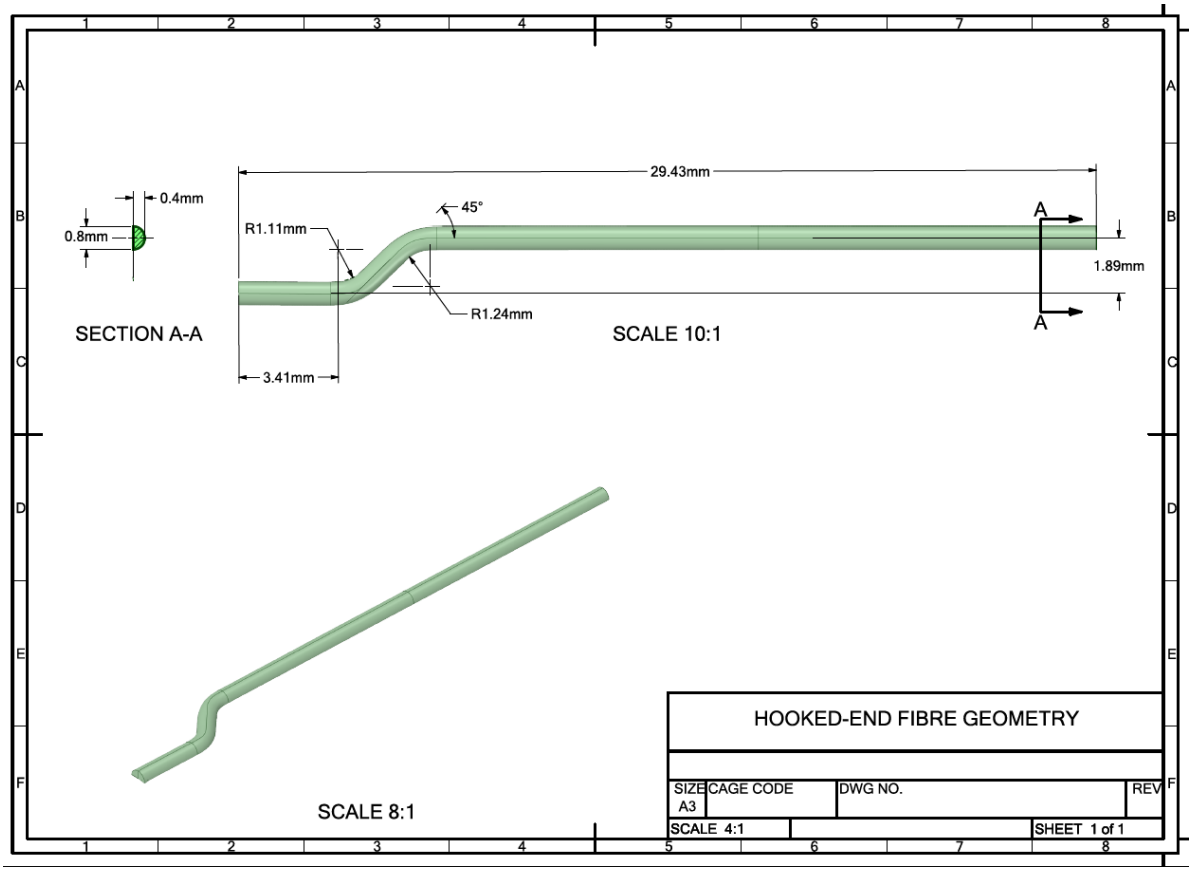

Figure B-5 General arrangement, hooked-end fibre geometry

© University of Pretoria

B.4 Mesh convergence for hooked-end forming

The convergence study was performed for a mesh size of 0.13mm and 0.08mm. This resulted in a 680% increase in the number of nodes and elements. The error between the final values for the hook depth was calculated as follows:

$$error = \frac{h_{0.08} - h_{0.13}}{h_{0.08}} \tag{22}$$

when converted to a percentage, the error between the hook depth obtained using a mesh size of 0.13mm and the hook depth obtained using a mesh size of 0.08mm was calculated to be equal to 0.085%. Results for the forming operation were therefore considered to have converged at a mesh size of 0.08mm.

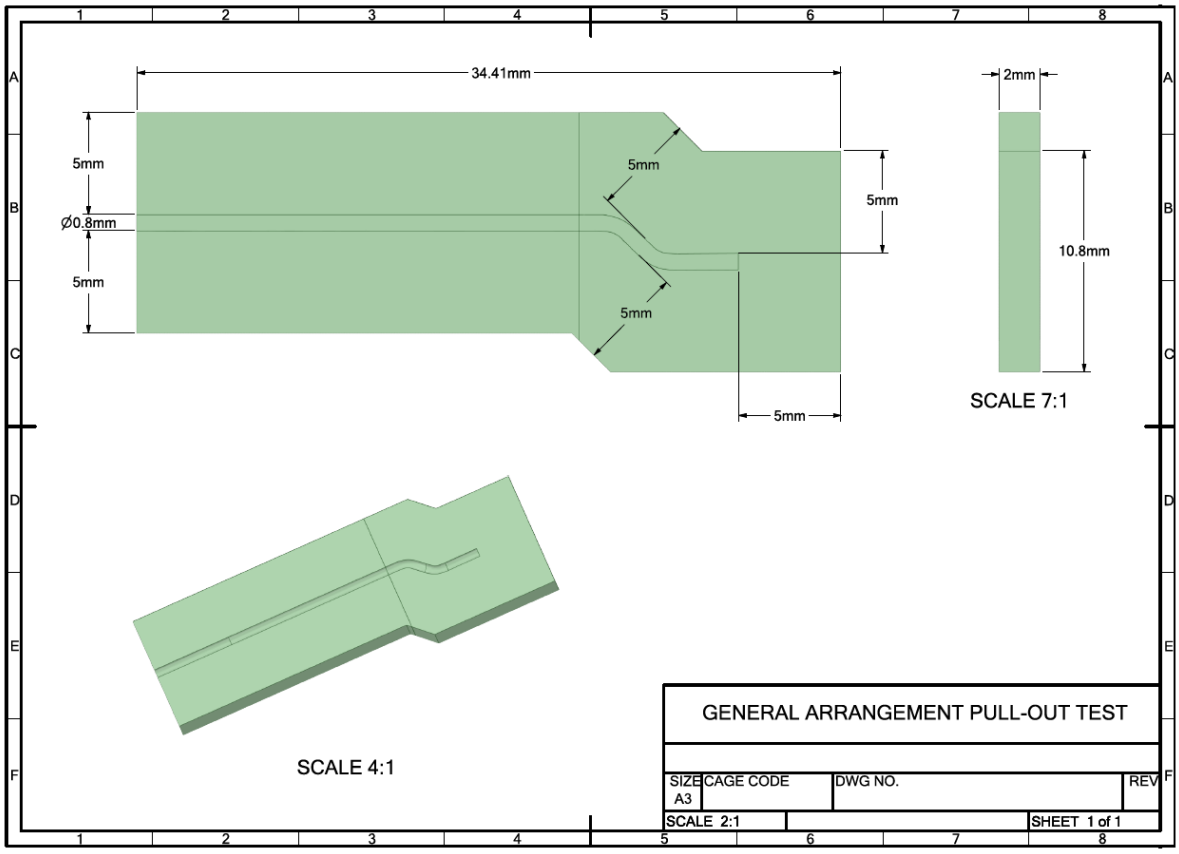

Figure B-6 General arrangement, pull-out test

B.5 Mesh convergence for pull-out test

A swept hexahedral mesh of quadratic elements was generated across the fibre with refinement applied to the hooked-end portion of the fibre. The concrete geometry was split into two parts, perpendicular to the axis of the wire just before the first bend, in order to facilitate mesh refinement on the inner surface of that portion of the duct in contact with the hooked end of the fibre. This portion of the concrete duct was meshed using second order tetrahedral elements. The remainder of the concrete geometry was meshed using quadratic hexahedral elements where possible and tetrahedral elements elsewhere. The mesh was refined until convergence was achieved on the reaction force at the prescribed displacement boundary condition.

The energy required for pull-out is given by the area underneath the pull-out curve. This was calculated using backward numerical integration:

© University of Pretoria

$$\mathbb{E} = \sum_{i=1}^{n} (d_i - d_{i-1}) F(d_i) \tag{23}$$

where d_i is the displacement at point i and $F(d_i)$ is the corresponding force at the point under consideration.

The convergence study was performed for a mesh size of 0.2mm and 0.12mm. This resulted in a 130% increase in the number of nodes and elements. The error between the force-displacement curves was calculated as follows:

$$error = \frac{\mathbb{E}_{0.12} - \mathbb{E}_{0.2}}{\mathbb{E}_{0.12}} \tag{24}$$

When converted to a percentage, the error between results obtained using a mesh size of 0.2mm and results obtained using a mesh size of 0.12mm was calculated to be equal to 3.9%. Results for the pull-out test were therefore considered to have converged at a mesh size of 0.12mm.

© University of Pretoria